Spin-dependent electronic transport in nanowires
in the presence of
Rashba and Dresselhaus spin-orbit couplings

Dissertation
zur Erlangung des Doktorgrades
des Department Physik
der Universität Hamburg

vorgelegt von
Masayuki Yamamoto
aus Osaka

Hamburg
2007

Gutachter der Dissertation:	Bernhard Kramer
	Stefan Kettemann
Gutachter der Disputation:	Bernhard Kramer
	Tomi Ohtsuki
Datum der Disputation:	2 August 2007
Vorsitzender des Prüfungsausschusses:	Alexander Chudnovskiy
Vorsitzender des Promotionsausschusses:	Günter Huber
MIN-Dekan der Faultät Department Physik:	Arno Frühwald

Zusammenfassung

Die Spin-Orbit Kopplung ist eine relativistische Korrektur zur Schrödingergleichung, die in Anwesenheit elektrischer Felder auftritt. Der Effekt ist ziemlich schwach und wird erst signifikant, wenn sich Elektronen in der Nähe von Atomkernen bewegen. In Festkörpern jedoch wird dieser Effekt durch die Kopplung der Bänder sehr verstärkt. Moderate elektrische Felder genügen, um die Spin- und Orbital-Zustände der Elektronen zu beeinflussen.

Vor einigen Dekaden sagte Rashba *et.al.* die Spin-Orbit Kopplung, verursacht durch die Asymmetrie des Einschlusspotentials, voraus. Während D'yakonov *et.al.* prognostizierte, dass die Separation von spinpolarisiertem elektrischem Strom durch die von Störstellen induzierte Spin-Orbit Kopplung auftreten sollte. Kürzlich fand man beide Effekte in Experimenten. Auf der einen Seite konnte gezeigt werden, dass die Stärke der Spin-Orbit Kopplung in einem zweidimensionalen Elektronensystem durch die Gatespannung modifiziert werden kann. Auf der anderen Seite hat man den sogenannten extrinsischen Spin-Hall Effekt in Halbleitern und Metallen sogar bei Raumtemperatur gefunden. Diese Entdeckungen öffnen den Weg zur Spintronik, welche bezweckt, den Spin eines elektrischen Stroms zusätzlich zu seiner Ladung zu verwenden.

In dieser Arbeit wird der spinabhängige elektronische Transport durch Nanodrähte in Anwesenheit der Spin-Orbit Kopplung numerisch untersucht. Zunächst zeigen wir die Herleitung des effektiven Hamiltonoperators mit Spin-Orbit Kopplung von der Betrachtung der Einheitszelle eines III-V-Halbleiters. Dann erörtern wir, wie man numerisch den elektronischen Transport in mesoskopischen Systemen, beschrieben durch den effektiven Hamiltonoperator, berechnet. Zum Schluss sagen wir voraus, dass die Kombination eines Three-Terminal Nanoscale Conductors mit Spin-Orbit Kopplung spinpolarisierten elektrischen Strom induzieren kann, in Abwesenheit magnetischer Felder.

Preface

Spin-orbit coupling is a relativistic correction to the Schrödinger equation in the presence of electric field. The effect is very weak and becomes significant only if electrons are traveling in the vicinity of nuclei of atoms where electric field is extremely high. In solids, however, this effect is strongly enhanced due to the band couplings. Moderate electric field is enough to affect the spin and orbital states of electrons.

A few decades ago, Rashba *et al.* predicted the spin-orbit coupling induced by the asymmetric confinement potential in two-dimensional systems while D'yakonov *et al.* predicted that separation of spin polarized electric current should occur due to the spin-orbit coupling induced by impurities. Recently, both effects have been observed in experiments. On the one hand, it is shown that the strength of spin-orbit coupling can be modified by gate voltage in two-dimensional electron systems.On the other hand, the so-called extrinsic spin Hall effect has been observed in semiconductors and metals even at room temperature. These observations open the way to spintronics which aims to use spin of an electric current in addition to charge of it.

In this thesis, we have numerically investigated the spin-dependent electronic transport via nanowires in the presence of spin-orbit coupling. We firstly show the derivation of the effective Hamiltonian with spin-orbit coupling from the unit cell of Ⅲ-Ⅴ semiconductors. Then we show how one can numerically calculate the electronic transport in mesoscopic systems described by the effective Hamiltonian. Finally, we have predicted that combination of three-terminal nanoscale conductor and spin-orbit coupling can induce spin polarized electric current in the absence of magnetic field.

Acknowledgement

First of all, I would like to thank Prof. Dr. B. Kramer and Prof. Dr. T. Ohtsuki for supervising my PHD course. I also thank the current and former member of mesoscopic group in Hamburg, S. Kettemann, J. Ohe, K. Dittmer, M. Kossow, H. Hübener, C. Jung, P. Wenk, B. Vogt, A. Struck, S. Debald, F. Cavaliere, and R. Mazzarello. I would like to express to Prof. Dr. C.J. Lambert, V.M. Garcia-Suarez and S. Sirichantaropass my gratitude for their accommodation during a short visit to Lancaster University. I am also grateful to Prof. Dr. J. Nitta. The financial support by Marie Curie Research Training Network was very helpful. I appreciate the Network very much. Finally, I thank Miyuki and my family.

List of publications

"Spin polarization induced by Rashba spin-orbit coupling in three terminal devices"
M. Yamamoto, K. Dittmer, B. Kramer, T. Ohtsuki, Physica E **32**, 462 (2006).

"Spin polarization in a T-shape conductor induced by strong Rashba spin-orbit coupling"
M. Yamamoto, T. Ohtsuki, B. Kramer, Phys. Rev. B **72**, 115321 (2005).

"Spin polarization in a 3-terminal conductor induced by Rashba spin-orbit coupling"
M. Yamamoto, J. Ohe, T. Ohtsuki, J.Nitta, B. Kramer, Physica E **29**, 490 (2005).

"Mesoscopic Stern-Gerlach spin filter by nonuniform spin-orbit interaction"
J. Ohe, M. Yamamoto, T. Ohtsuki, J. Nitta, Phys. Rev. B **72**, 041308(R) (2005).

"Spin-polarized current induced by three terminal geometry"
M. Yamamoto, J. Ohe, T. Ohtsuki, Physica E **22**, 430 (2004).

"Conductance fluctuations in the presence of spin scattering"
J. Ohe, M. Yamamoto, T. Ohtsuki, Phys. Rev. B **68**, 165344 (2003).

"Effect of magnetic field applied on leads"
M. Yamamoto, T. Ohtsuki, K. Slevin, J. Phys. Soc. Jpn. **72**, Suppl. A, 155 (2003).

List of presentations

International Conferences

(2006)
"Spin Hall current induced by acceleration of electrons"
ICPS-28, Vienna, Austria (July 24-28, 2006). [poster]

(2005)
"Spin polarization induced by Rashba spin-orbit coupling in three terminal devices"
MSS-12, New Mexico, USA (July 10-15, 2005). [poster]

"Spin polarization in a 3-terminal conductor induced by Rashba spin-orbit coupling"
1st International Symposium on "Nanometer-scale Quantum Physics" (nanoPHYS'05), Tokyo, Japan (January 26-28, 2005). [oral]

(2003)
"Spin-polarized current induced by three terminal geometry"
EP2DS-15, Nara, Japan (July 14-18, 2003). [poster]

(2002)
"Effect of magnetic field applied on leads"
International Conference on "Quantum Transport and Quantum Coherence" (Localization 2002), Tokyo, Japan (August 16-19, 2002). [poster]

Domestic meetings, Workshops, and Summerschools

(2006)
"Spin Hall current induced by electric field pulse"
International workshop of MCRTN on "Fundamentals of Nanoelectronics", Keszthely, Hungary (August 27 - September 1, 2006). [poster]

"Spin Hall current induced by electric field pulse"
International school/workshop on "Spin and charge effects at the nanoscale" (SCEN06), Pisa, Italy (June 1-9, 2006). [poster]

"Spintronics"
Marie Curie Advanced Study Institute "Quantum Optics and Computation", Riomaggiore, Italy (April 2-7, 2006). [oral]

(2005)
"Spin polarization and spin Hall effect in the presence of Rashba spin-orbit coupling"
International workshop of MCRTN on "Nanoscale Dynamics and Quantum Coherence", Catania, Italy (October 2-5, 2005). [oral]

"Spin polarization in a T-shape conductor induced by strong Rashba spin-orbit coupling"
6th International WEH Summerschool on "Spintronics", Wittenberg, Germany (August 1-12, 2005). [poster]

"Spin polarization in a T-shape conductor induced by strong Rashba spin-orbit coupling"
JPS Spring Meetings, Chiba, Japan (March 24-27, 2005). [oral]

"Spin polarization in a T-shape conductor induced by strong Rashba spin-orbit coupling"
DPG Spring Meetings, Berlin, Germany (March 4-9, 2005). [poster]

(2004)
"Spin-polarization by T-shaped geometry with strong Rashba spin-orbit coupling"
International workshop of MCRTN on "Nanoscale Dynamics and Quantum Coherence", Hamburg, Germany (September 19-23, 2004). [oral+poster]

"Spin-polarization by T-shaped geometry with strong Rashba spin-orbit coupling"
5th International WEH Summerschool on "Molecules", Wittenberg, Germany (August 2-13, 2004). [poster]

(2003)
"Spin-filtering by three terminal geometry"
JPS Autumn Meetings, Okayama, Japan (September 20-23, 2003). [oral]

Contents

Chapter 1

Introduction

1.1 Nanotechnology

Nanotechnology is a field of applied science focused on the materials and devices on the nanoscale. It is a technology in chemistry, biology, physics and other scientific fields. Two main approaches are used in nanotechnology. One is a "bottom-up" approach where materials and devices are built up atom by atom. The other is a "top-down" approach where they are constructed by removing existing material from larger entities. A unique aspect of nanotechnology is the significantly increased ratio of surface area to volume, which opens new possibilities in surface-based science.

The current interest for nanotechnology has originated from new analytical tools such as the atomic force microscope (AFM) and the scanning tunneling microscope (STM). Combined with refined processes such as electron beam lithography, these instruments allow the detailed manipulation of nanostructures. These new materials and structures have led to the observation of novel phenomena such as the quantum size effect. This effect does not come into play by going from macro to micro dimensions. However, it becomes dominant when the nanometer size range is reached.

Materials reduced to the nanoscale can suddenly show very different properties compared to what they exhibit on a macroscopic scale. For example, insulators become conductors; solids turn into liquids at room temperature; stable materials turn combustible; inert materials become catalysts; opaque substances become transparent. These unique quantum and surface phenomena enable unique applications. Quantum dots and carbon nanotubes

are examples of the most prominent systems and materials in the field of nanotechnology.

1.2 Spintronics

Spintronics is a technology which uses the spin of electrons as well as their charge state. In order to make a spintronic device, it is necessary to have a system that can generate a spin polarized current, and a system that is sensitive to the spin polarization of the electrons. Most devices also have a unit that changes the magnitude of a current depending on its spin states.

The simplest spintronic device consists of two ferromagnetic layers separated by a non-magnetic spacer layer. The first layer is used to generate a spin polarized current. If the spin direction of a spin polarized current is parallel to the second layer, the resistance is low and a current will flow freely. On the other hand, if the spin direction of a spin polarized current is antiparallel to the second layer, the resistance is high and a current will not flow very much. This effect is called a giant magnetoresistance (GMR).

GMR effect is used in a spin valve device (Fig. 1.1). In a spin valve, one of the ferromagnetic layers is pinned while the other ferromagnetic layer is free to rotate by an applied magnetic field. Spin valves can be designed with soft free layers which have a very sensitive response to magnetic fields. Such spintronic devices are used in the field of mass-storage devices. Recently, one could compress massive amounts of data into a small area. The storage density of hard disk drives is rapidly increasing.

Future applications may include a spin field effect transistor as we introduce in the next section. This requires the development of magnetic semiconductors exhibiting room temperature ferromagnetism. The operation of magnetic random access memory (MRAM) is also based on spintronic principles.

1.3 Device applications

In this section, we briefly introduce a few spintronic device proposals based on the so-called Rashba spin-orbit coupling (RSO). RSO is originated from the asymmetry of the confining potential perpendicular to two dimensional electron systems.

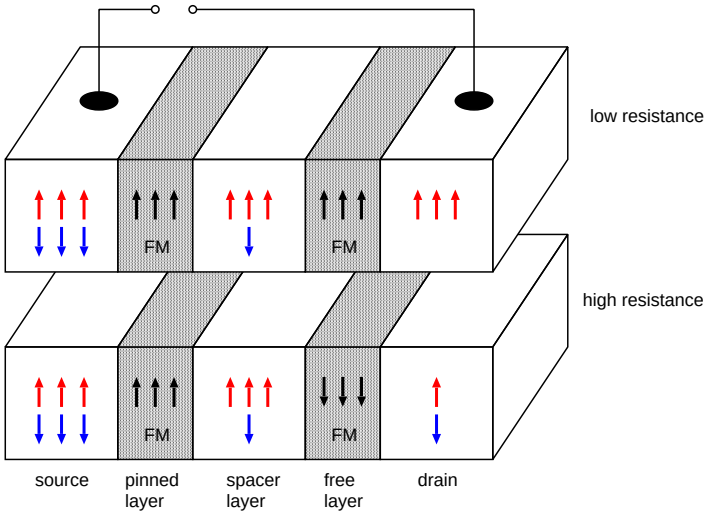

Figure 1.1: Schematic of the spin valve. The spin direction of a free layer can be rotated by an external magnetic field.

The Rashba Hamiltonian is given by

$$H_{\rm rso} = \frac{\alpha}{\hbar}\left(\sigma_x p_y - \sigma_y p_x\right) \tag{1.1}$$

where α denotes the strength of RSO, and σ_i and p_i $(i = x, y)$ are the Pauli matrices and components of the momentum, respectively [1]. In the presence of RSO, propagating electrons feel effective in-plane magnetic field perpendicular to its traveling direction (Sec. 3.5). This effective magnetic field induces the spin precession of propagating electrons.

1.3.1 Spin FET

One of the most important features of RSO is that one can control the strength of RSO by gate voltage [2, 3]. In 1990, Datta and Das proposed the spin field effect transistor (spin FET) based on this property [4]. The transistor consists of a sample region with RSO attached to two ferromagnetic contacts (Fig. 1.2).

The mechanism of the spin FET is as follows:

1. Spin polarized electrons are injected from a ferromagnetic source contact.

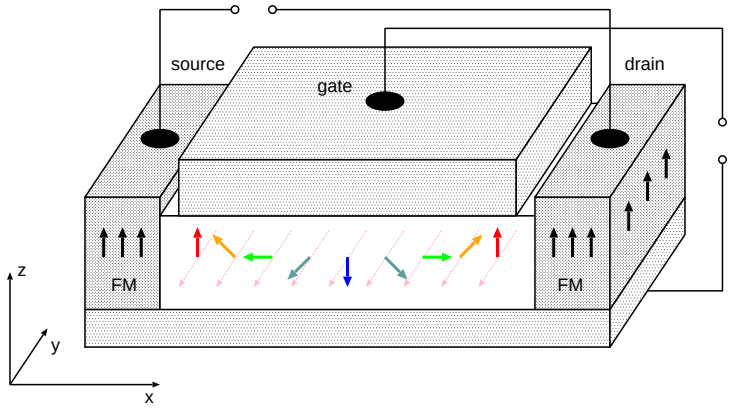

Figure 1.2: Schematic of the spin field effect transistor (spin FET). The spin precession length of electrons can be modified by gate voltage.

2. Spin precession occurs due to the effective magnetic field induced by RSO.

3. Output current will (not) flow if spins of electrons leaving a sample region are parallel (antiparallel) to those of a ferromagnetic drain contact.

One can modify the strength of RSO so that the spin precession length and the output current are changed.

The spin FET proposal attracted much interest on RSO and spintronics. However, it has not been experimentally realized yet. The main obstacle is the junction between ferromagnetic contacts and a sample region. Since a sample region is semiconductor while contacts are metal, there is a large mismatch at the junction and the spin polarization of current is dramatically reduced [5]. In order to overcome this problem, it is necessary to use ferromagnetic semiconductor contacts or to generate spin polarized current without using ferromagnetic materials. Both of them are main current research topics in the field of spintronics.

1.3.2 Spin interference device

In addition to the spin precession, propagating electrons will acquire the spin-dependent phase factor in the presence of RSO (Sec. 3.6). In 1999, Nitta *et*

al. proposed the spin interference device based on this property [6]. The device consists of a sample region with RSO attached to normal contacts (Fig. 1.3). The mechanism is the same as that of the AB oscillation except the use of RSO instead of magnetic flux. One can control the strength of RSO by gate voltage so that the effective flux through ring and the output current are changed. The magnitude of the output conductance is given by

$$G = \frac{e^2}{h}\left[1 + \cos\left(2\pi a \frac{\alpha m^*}{\hbar^2}\right)\right], \tag{1.2}$$

where a denotes the radius of a ring [6]. This spin interference device has been experimentally realized by Koga *et al.* [7].

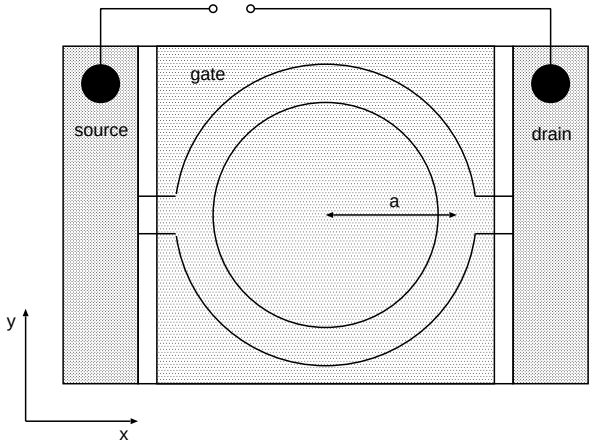

Figure 1.3: Schematic of the spin interference device (top view). The magnitude of an effective flux through ring can be modified by gate voltage.

Chapter 2

Bandstructure

In this chapter, we will briefly introduce how to derive the effective Hamiltonian for a conduction band from the atom and structure of materials. We will start with the calculation of a band structure for a two-atoms periodic lattice as example. Then we derive the $\boldsymbol{k}$-dependent Hamiltonian for a unit cell of GaAs by using the sp^3s^* model [8]. After that, we transform the basis of Hamiltonian from orbital states to eigenstates at the Γ-point ($\boldsymbol{k} = 0$). Finally, we obtain the effective Hamiltonian for a conduction band in the vicinity of the Γ-point by using the Löwdin partitioning (perturbation) [9]. These procedures are summarized as a flowchart in Fig. 2.1.

2.1 Procedure of calculating bandstructure

Firstly, let us consider the two-atoms periodic lattice in one-dimensional system as shown in Fig. 2.2. By using one orbital per atom, the Hamiltonian

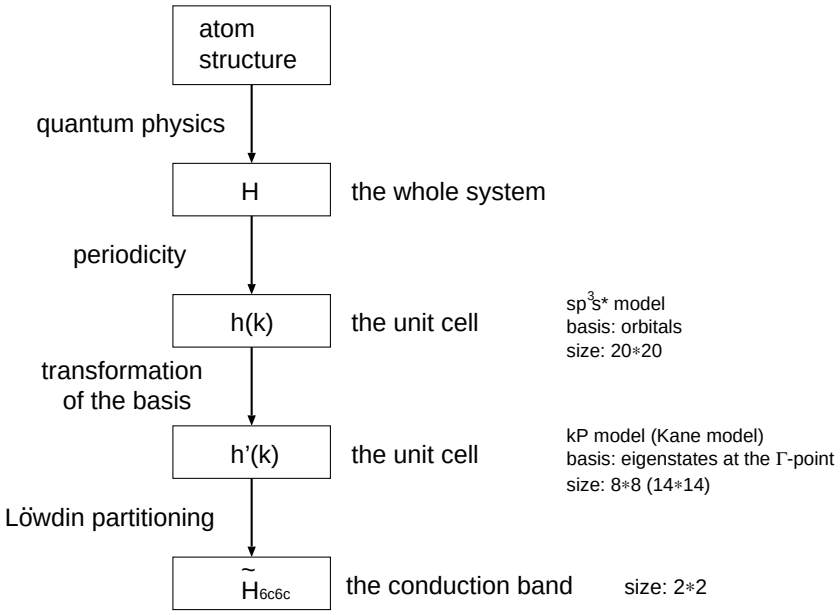

Figure 2.1: Flowchart of deriving the effective Hamiltonian for a conduction band.

can be written in the matrix representation as

$$H = \begin{array}{c} \\ \vdots \\ \langle 1A| \\ \langle 1B| \\ \langle 2A| \\ \langle 2B| \\ \langle 3A| \\ \langle 3B| \\ \vdots \end{array} \begin{array}{c} \begin{array}{ccccccccc} \cdots & |1A\rangle & |1B\rangle & |2A\rangle & |2B\rangle & |3A\rangle & |3B\rangle & \cdots \end{array} \\ \begin{pmatrix} \ddots & \vdots & \vdots & \vdots & \vdots & \vdots & \vdots & \\ \cdots & E_A & V & 0 & 0 & 0 & 0 & \cdots \\ \cdots & V & E_B & V' & 0 & 0 & 0 & \cdots \\ \cdots & 0 & V' & E_A & V & 0 & 0 & \cdots \\ \cdots & 0 & 0 & V & E_B & V' & 0 & \cdots \\ \cdots & 0 & 0 & 0 & V' & E_A & V & \cdots \\ \cdots & 0 & 0 & 0 & 0 & V & E_B & \cdots \\ & \vdots & \vdots & \vdots & \vdots & \vdots & \vdots & \ddots \end{pmatrix} \end{array}, \quad (2.1)$$

where E_A and E_B denotes the energy of the atom A and B, respectively. The term V represents the hopping energy between the atom A and B in the same unit cell while V' that between the atom B and the atom A of the nearest neighbor unit cell.

By combining the elements of the matrix into (2×2) blocks, one can

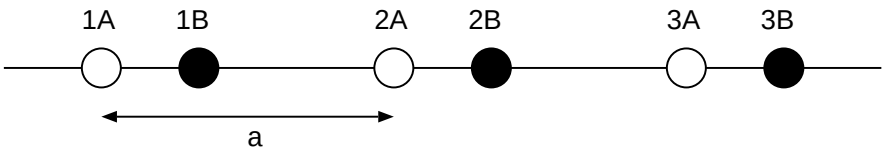

Figure 2.2: Schematic of a two-atoms periodic lattice in one-dimensional system. Unit cells including atoms A and B are replaced by the distance a.

rewrite this Hamiltonian as

$$H = \begin{array}{c} \\ \vdots \\ \langle 1| \\ \langle 2| \\ \langle 3| \\ \vdots \end{array} \begin{array}{c} \begin{array}{ccccc} \cdots & |1\rangle & |2\rangle & |3\rangle & \cdots \end{array} \\ \begin{pmatrix} \ddots & \vdots & \vdots & \vdots & \\ \cdots & H_{11} & H_{12} & 0 & \cdots \\ \cdots & H_{21} & H_{22} & H_{23} & \cdots \\ \cdots & 0 & H_{32} & H_{33} & \cdots \\ & \vdots & \vdots & \vdots & \ddots \end{pmatrix} \end{array}, \tag{2.2}$$

where

$$H_{nn} = \begin{pmatrix} E_A & V \\ V & E_B \end{pmatrix}, H_{n,n-1} = \begin{pmatrix} 0 & V' \\ 0 & 0 \end{pmatrix}, H_{n,n+1} = \begin{pmatrix} 0 & 0 \\ V' & 0 \end{pmatrix}. \tag{2.3}$$

In this representation, one can obtain the following matrix equation for any particular unit cell n,

$$H_{n,n-1} |n-1\rangle + H_{nn} |n\rangle + H_{n,n+1} |n+1\rangle = E |n\rangle . \tag{2.4}$$

By using the ansatz,

$$|n\rangle = \mathrm{e}^{ikna} |0\rangle , \tag{2.5}$$

this set of equations can be simplified as

$$\left(H_{n,n-1}\mathrm{e}^{-ika} + H_{nn} + H_{n,n+1}\mathrm{e}^{ika}\right) |0\rangle = E |0\rangle , \tag{2.6}$$

that is

$$\begin{pmatrix} E_A & V + V'\mathrm{e}^{-ika} \\ V + V'\mathrm{e}^{ika} & E_B \end{pmatrix} |0\rangle = E |0\rangle . \tag{2.7}$$

By diagonalizing this (2×2) matrix, one can obtain the k-dependent eigenvalues,

$$E_{\pm}(k) = \frac{(E_A + E_B) \pm \sqrt{(E_A - E_B)^2 + 4(V^2 + V'^2 + 2VV' \cos(ka))}}{2}. \quad (2.8)$$

We show this dispersion relation of the two-atoms periodic lattice in Fig. 2.3. The parameters are $E_A = 1$, $E_B = -1$, $V = 2$, and $V' = 1$. Qualitatively same dispersion relation can be obtained for a two-atoms periodic lattice made by the same atom, i.e., $E_A = E_B$. This means that the transtion from a one-atom periodic lattice to a two-atoms one opens a band-gap. If the Fermi energy of a material is inside this band-gap, the material changes its property from conductor to insulator (Peierls transition).

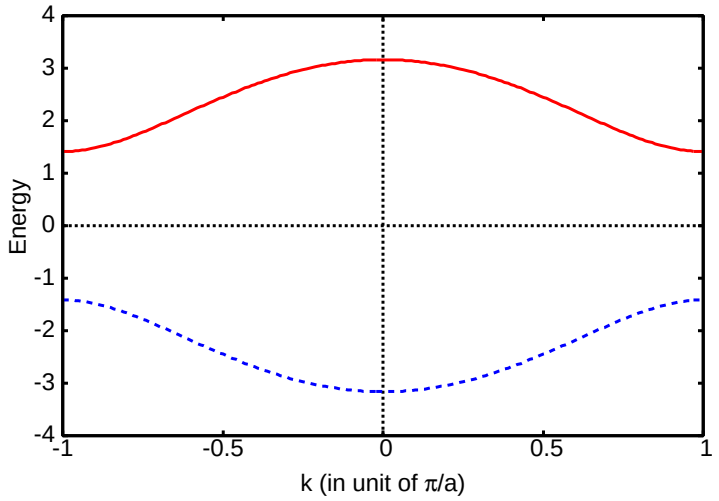

Figure 2.3: Dispersion relation of the two-atoms periodic lattice (Eq. (2.8)). Parameters are $E_A = 1$, $E_B = -1$, $V = 2$, and $V' = 1$.

This procedure can be easily generalized. Now let us consider any particular unit cell n coupled with several unit cells m. One can write down the following matrix equation,

$$\sum_m H_{nm} |m\rangle = E |n\rangle . \quad (2.9)$$

The size of the matrix H_{nm} depends on the number of basis functions per unit cell.

By substituting the ansatz,

$$|m\rangle = \mathrm{e}^{i\boldsymbol{k}\cdot\boldsymbol{d}_m}\,|0\rangle\,, \tag{2.10}$$

into Eq. (2.9), one can obtain

$$h(\boldsymbol{k})\,|0\rangle = E\,|0\rangle\,, \tag{2.11}$$

where

$$h(\boldsymbol{k}) = \sum_m H_{nm}\mathrm{e}^{i\boldsymbol{k}\cdot(\boldsymbol{d}_m-\boldsymbol{d}_n)}. \tag{2.12}$$

The dispersion relation (bandstructure) can be plotted by diagonalizing the Hamiltonian $h(\boldsymbol{k})$ for each value of $\boldsymbol{k}$. If we assume that the number of basis functions per unit cell is b, it will show b branches.

2.2 Bandstructure of gallium arsenide

Gallium arsenide (GaAs) belongs to the diamond structure which has a unit cell consisting of Ga (cation) and As (anion) atoms. For each atom, we need to include at least four valence orbitals, that is 4s, $4p_x$, $4p_y$ and $4p_z$. It is common to include the next higher orbital (5s) as well. This is so called the sp^3s^* model and the unit cell has 10 basis, 5 orbitals multiplied by 2 atoms. This means that the Hamiltonian $h(\boldsymbol{k})$ is given by (10×10) matrix.

Now let us consider the structure of GaAs. The diamond structure consists of two interpenetrating face-centered cubic (FCC) lattice as shown in Fig. 2.4. The lattice of As atoms can be obtained by adding $(1, 1, 1)a/4$ to that of Ga atoms. As shown in Fig. 2.5, the As atom in a diamond structure has four nearest neighbors of the Ga atoms arranged in a tetrahedron.

By considering these structure, the Hamiltonian can be obtained as [8, 10]

$$h(\boldsymbol{k}) =$$

$$\begin{array}{c} \\ \langle s_a| \\ \langle s_c| \\ \langle X_a| \\ \langle Y_a| \\ \langle Z_a| \\ \langle X_c| \\ \langle Y_c| \\ \langle Z_c| \\ \langle s_a^*| \\ \langle s_c^*| \end{array} \begin{array}{c} \begin{array}{cccccccccc} |s_a\rangle & |s_c\rangle & |X_a\rangle & |Y_a\rangle & |Z_a\rangle & |X_c\rangle & |Y_c\rangle & |Z_c\rangle & |s_a^*\rangle & |s_c^*\rangle \end{array} \\ \begin{pmatrix} E_{sa} & 4E_{ss}g_0 & 0 & 0 & 0 & 4E_{sapc}g_1 & 4E_{sapc}g_2 & 4E_{sapc}g_3 & 0 & 0 \\ 4E_{ss}g_0^* & E_{sc} & 4E_{pasc}g_1^* & 4E_{pasc}g_2^* & 4E_{pasc}g_3^* & 0 & 0 & 0 & 0 & 0 \\ 0 & 4E_{pasc}g_1 & E_{pa} & 0 & 0 & 4E_{xx}g_0 & 4E_{xy}g_3 & 4E_{xy}g_2 & 0 & 4E_{pas^*c}g_1 \\ 0 & 4E_{pasc}g_2 & 0 & E_{pa} & 0 & 4E_{xy}g_3 & 4E_{xx}g_0 & 4E_{xy}g_1 & 0 & 4E_{pas^*c}g_2 \\ 0 & 4E_{pasc}g_3 & 0 & 0 & E_{pa} & 4E_{xy}g_2 & 4E_{xy}g_1 & 4E_{xx}g_0 & 0 & 4E_{pas^*c}g_3 \\ 4E_{sapc}g_1^* & 0 & 4E_{xx}g_0^* & 4E_{xy}g_3^* & 4E_{xy}g_2^* & E_{pc} & 0 & 0 & 4E_{s^*apc}g_1^* & 0 \\ 4E_{sapc}g_2^* & 0 & 4E_{xy}g_3^* & 4E_{xx}g_0^* & 4E_{xy}g_1^* & 0 & E_{pc} & 0 & 4E_{s^*apc}g_2^* & 0 \\ 4E_{sapc}g_3^* & 0 & 4E_{xy}g_2^* & 4E_{xy}g_1^* & 4E_{xx}g_0^* & 0 & 0 & E_{pc} & 4E_{s^*apc}g_3^* & 0 \\ 0 & 0 & 0 & 0 & 0 & 4E_{s^*apc}g_1 & 4E_{s^*apc}g_2 & 4E_{s^*apc}g_3 & E_{s^*a} & 0 \\ 0 & 0 & 4E_{pas^*c}g_1 & 4E_{pas^*c}g_2 & 4E_{pas^*c}g_3 & 0 & 0 & 0 & 0 & E_{s^*c} \end{pmatrix} \end{array} \tag{2.13}$$

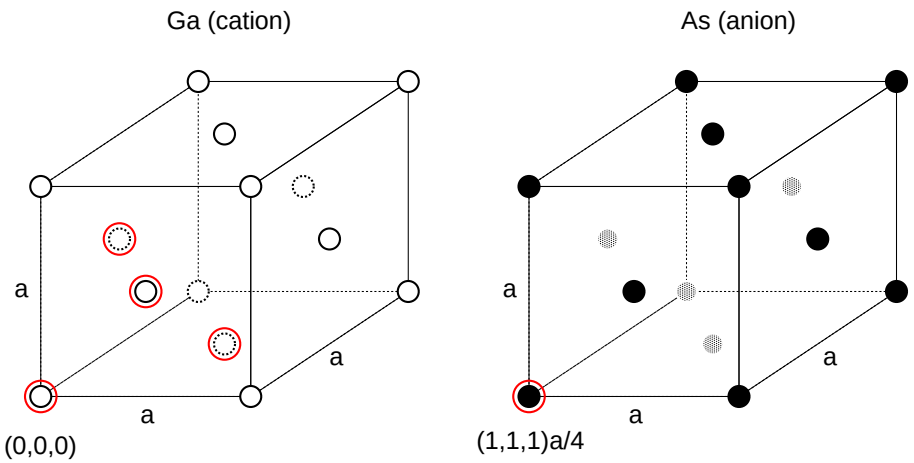

Figure 2.4: Schematic of the FCC lattices based on Ga and As atoms. The lattice of As atoms is shifted from that of Ga atoms by $(1,1,1)a/4$. The diamond structure of GaAs consists of these two FCC lattices.

Here E_{sa} and E_{sc} denotes the energies of the 4s-orbitals for the anion (As) and cation (Ga), E_{pa} and E_{pc} the energies of the 4p-orbitals, and E_{s^*a}, and E_{s^*c} the energies of the 5s-orbitals, respectively. The hopping terms between the orbitals are given by E_{ss}, E_{xx}, E_{xy}, E_{sapc}, E_{pasc}, E_{s^*apc}, and E_{pas^*c}. The factor g_0, g_1, g_2, and g_3 are defined by

$$
\begin{aligned}
4g_0 &\equiv 1 + \mathrm{e}^{-i\boldsymbol{k}\cdot\boldsymbol{d_1}} + \mathrm{e}^{-i\boldsymbol{k}\cdot\boldsymbol{d_2}} + \mathrm{e}^{-i\boldsymbol{k}\cdot\boldsymbol{d_3}} && (2.14)\\
4g_1 &\equiv 1 + \mathrm{e}^{-i\boldsymbol{k}\cdot\boldsymbol{d_1}} - \mathrm{e}^{-i\boldsymbol{k}\cdot\boldsymbol{d_2}} - \mathrm{e}^{-i\boldsymbol{k}\cdot\boldsymbol{d_3}} && (2.15)\\
4g_2 &\equiv 1 - \mathrm{e}^{-i\boldsymbol{k}\cdot\boldsymbol{d_1}} + \mathrm{e}^{-i\boldsymbol{k}\cdot\boldsymbol{d_2}} - \mathrm{e}^{-i\boldsymbol{k}\cdot\boldsymbol{d_3}} && (2.16)\\
4g_3 &\equiv 1 - \mathrm{e}^{-i\boldsymbol{k}\cdot\boldsymbol{d_1}} - \mathrm{e}^{-i\boldsymbol{k}\cdot\boldsymbol{d_2}} + \mathrm{e}^{-i\boldsymbol{k}\cdot\boldsymbol{d_3}} && (2.17)
\end{aligned}
$$

where

$$
\begin{aligned}
\boldsymbol{d}_1 &= (0,1,1)a/2 && (2.18)\\
\boldsymbol{d}_2 &= (1,0,1)a/2 && (2.19)\\
\boldsymbol{d}_3 &= (1,1,0)a/2\,. && (2.20)
\end{aligned}
$$

Figure 2.6 shows the bandstructure calculated by diagonalizing Eq. (2.13) for each value of $\boldsymbol{k}$ along the $\Gamma - X$ and $\Gamma - L$ directions. Parameters are summarized in Table. 2.1 [8, 10].

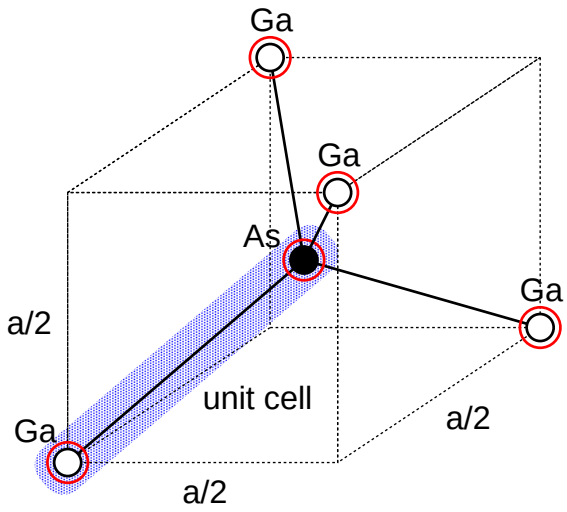

Figure 2.5: Schematic of the unit cell. The As atom has four nearest neighbor Ga atoms, one of which is in the same unit cell. They are coupled by 4s-, 4p-, and 5s-orbitals.

2.2.1 Eigenstates at the Γ-point

In typical experiments, the Fermi energy of semiconductors are lying at 10-100 meV above (below) the edge of the conduction (valence) band. For this reason, we are especially interested in the vicinity of the Γ-point ($\boldsymbol{k} = 0$). At the Γ-point, the factors g_1, g_2, and g_3 in Eqs. (2.15)-(2.17) become equal to zero. This means that the 4s-, 4p-, and 5s-orbitals are decoupled each other (Fig. 2.7). The wave functions at the points 1 and 5 in Fig. 2.8 are simply given by the linear combination of 4s-orbitals in anion (As) and cation (Ga) atoms while those at the points 2, 3, 4 and 6, 7, 8 are given by that of 4p-orbitals. The wave function at the point 9 and 10 is given by the 5s-orbital in cation (Ga) and that in anion (As), respectively. It shows that, in the vicinity of the Γ-point, the 4s-orbitals are dominant in the conduction band (blue line with No.5 at the Γ-point in Fig. 2.8) while the 4p-orbitals are dominant in the valence band (red and green lines with No.2,3,4 at the Γ-point in Fig. 2.8).

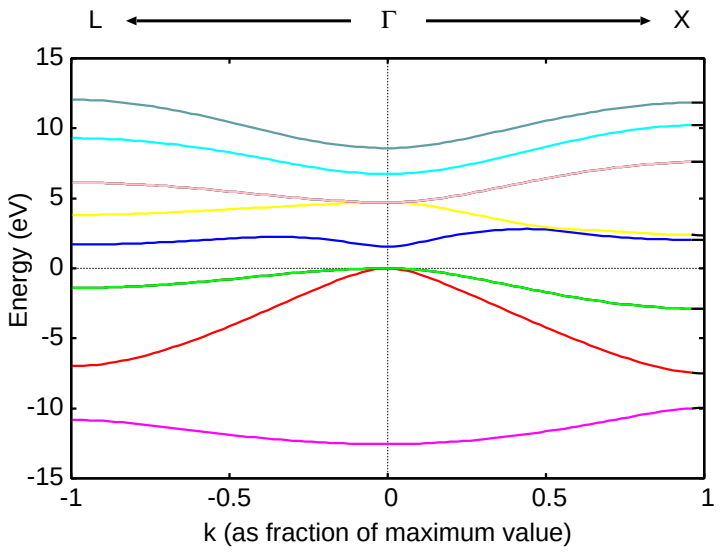

Figure 2.6: The bandstructre of GaAs for $\boldsymbol{k}$ along the $\Gamma - X$ (from $\boldsymbol{k} = (0,0,0)$ to $(1,0,0)2\pi/a$) and $\Gamma - X$ (from $\boldsymbol{k} = (0,0,0)$ to $(1,1,1)\pi/a$) directions. Some bands are degenerate.

2.2.2 Conduction band

It is well known that the sp^3s^* model gives a reasonably accurate bandstructure. What happens if we ignore the contribution from 4p-orbitals or 5s-orbitals? Figure 2.9 shows the bandstructure of the conduction band of GaAs for the restricted hopping terms. We take into account the hopping between Ga and As atom via (1) only 4s-orbitals, (2) 4s- and 4p- orbitals, and (3) 4s-, 4p- and 5s-orbitals (Fig. 2.10). It is shown that if we assume the hopping via 4s-orbitals only, the conduction band becomes antiparabolic. This is not realistic at all. By including the contribution of 4p-orbitals, the bandstructure becomes quite accurate in the vicinity of the Γ-point, but is not for large $\boldsymbol{k}$.

2.3 Effect of spin-orbit couping

When electrons are traveling at very high velocities, relativistic effects become significant and one need to use the Dirac equation instead of the

E_{sa}	-8.3431	$4E_{ss}$	-6.4513
E_{sc}	-2.6569	$4E_{xx}$	1.9546
E_{pa}	1.0414	$4E_{xy}$	5.0779
E_{pc}	3.6686	$4E_{sapc}$	4.48
E_{s^*a}	8.5914	$4E_{pasc}$	-5.7839
E_{s^*c}	6.7386	$4E_{sa^*pc}$	4.8422
		$4E_{pas^*c}$	-4.8077

Table 2.1: Parameters for GaAs in the unit of eV.

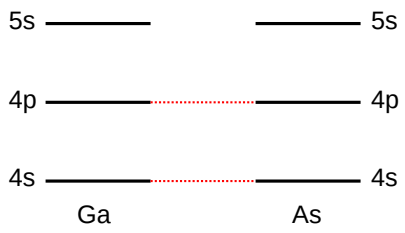

Figure 2.7: Schematic of the coupling between Ga and As atom at the Γ-point ($\boldsymbol{k} = 0$). The 4s-, 4p-, and 5s-orbitals are decoupled each other.

Schrödinger equation. In solids, the velocity of electrons is not so high that one can include relativistic effects into the the Schrödinger equation by perturbation (see Sec. 2.6).

One of these relativistic corrections is the spin-orbit coupling,

$$H_{so} = -\frac{\hbar}{4m^2c^2}\boldsymbol{\sigma} \cdot (\boldsymbol{p} \times \nabla U_0(\boldsymbol{r})). \tag{2.21}$$

The spin-orbit coupling is usually very weak. But it can not be ignored when electrons are traveling around the nuclei of atoms where the electric field is very high. If we assume the spherically symmetric atomic potential $U_0(r)$, the spin-orbit term can be written by

$$H_{so} = \frac{\hbar}{4m^2c^2}\frac{1}{r}\frac{dU_0(r)}{dr}\boldsymbol{l} \cdot \boldsymbol{\sigma} \tag{2.22}$$

where $\boldsymbol{l} = \boldsymbol{r} \times \boldsymbol{p}$.

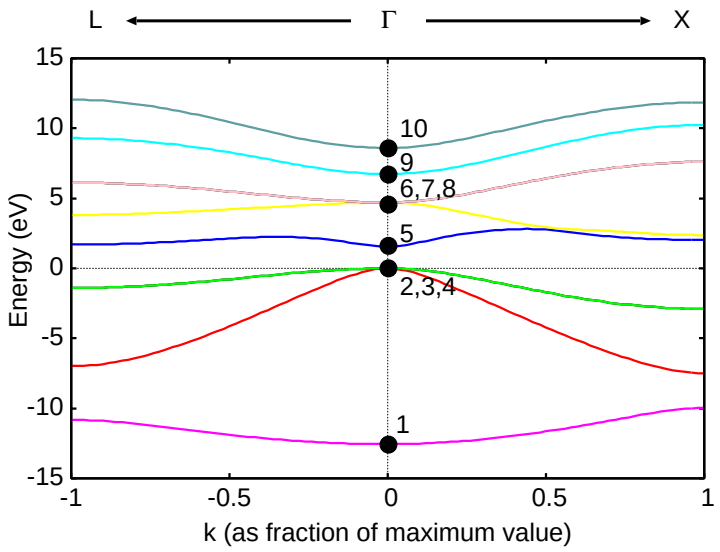

Figure 2.8: The bandstructre of GaAs.

The operator $\boldsymbol{l}\cdot\boldsymbol{\sigma}$ can be evaluated by the total angular momentum state $\left|j = l \pm \frac{1}{2}\right\rangle$ $(l \neq 0)$ as [11]

$$\boldsymbol{l}\cdot\boldsymbol{\sigma}\left|l+\frac{1}{2}\right\rangle = \quad l \quad \left|l+\frac{1}{2}\right\rangle, \tag{2.23}$$

$$\boldsymbol{l}\cdot\boldsymbol{\sigma}\left|l-\frac{1}{2}\right\rangle = \quad -(l+1) \quad \left|l-\frac{1}{2}\right\rangle. \tag{2.24}$$

Hence the spin-orbit coupling induces the band splitting for the p-orbital $(l = 1)$ states. In other words, the spin-orbit coupling mixes the spin up and down states of the p-orbitals as shown in Fig. 2.11.

In the matrix representation, the spin-orbit coupling can be expressed in terms of a single number δ_a for the anionic orbitals,

$$\begin{array}{c} \\ X_a \\ Y_a \\ Z_a \\ \bar{X}_a \\ \bar{Y}_a \\ \bar{Z}_a \end{array} \begin{array}{c} \begin{array}{cccccc} X_a & Y_a & Z_a & \bar{X}_a & \bar{Y}_a & \bar{Z}_a \end{array} \\ \begin{pmatrix} 0 & -i\delta_a & 0 & 0 & 0 & \delta_a \\ i\delta_a & 0 & 0 & 0 & 0 & -i\delta_a \\ 0 & 0 & 0 & -\delta_a & i\delta_a & 0 \\ 0 & 0 & -\delta_a & 0 & i\delta_a & 0 \\ 0 & 0 & -i\delta_a & -i\delta_a & 0 & 0 \\ \delta_a & i\delta_a & 0 & 0 & 0 & 0 \end{pmatrix} \end{array}, \tag{2.25}$$

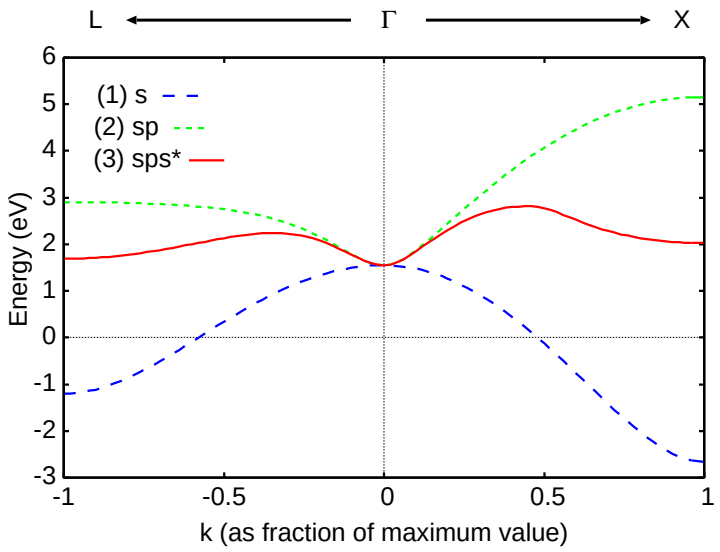

Figure 2.9: The conduction band of GaAs for the restricted hopping terms. The hopping between Ga and As atom is taken into account via (1) only 4s-orbitals, (2) 4s- and 4p- orbitals, and (3) 4s-, 4p- and 5s-orbitals (Fig. 2.10).

and in terms of a single number δ_c for the cationic orbitals,

$$\begin{array}{c} \\ X_c \\ Y_c \\ Z_c \\ \bar{X}_c \\ \bar{Y}_c \\ \bar{Z}_c \end{array} \begin{array}{c} \begin{array}{cccccc} X_c & Y_c & Z_c & \bar{X}_c & \bar{Y}_c & \bar{Z}_c \end{array} \\ \begin{pmatrix} 0 & -i\delta_c & 0 & 0 & 0 & \delta_c \\ i\delta_c & 0 & 0 & 0 & 0 & -i\delta_c \\ 0 & 0 & 0 & -\delta_c & i\delta_c & 0 \\ 0 & 0 & -\delta_c & 0 & i\delta_c & 0 \\ 0 & 0 & -i\delta_c & -i\delta_c & 0 & 0 \\ \delta_c & i\delta_c & 0 & 0 & 0 & 0 \end{pmatrix} \end{array}. \tag{2.26}$$

The spin-orbit splitting Δ_c (or Δ_a) is given by

$$\Delta_c(\text{or}\Delta_a) = 3\delta_c(\text{or}\delta_a). \tag{2.27}$$

The values of the spin-orbit splitting is well-known from both theory and experiment for all the atoms. For example, Ga has a spin-orbit splitting of 0.013eV while that of As is 0.38eV [8].

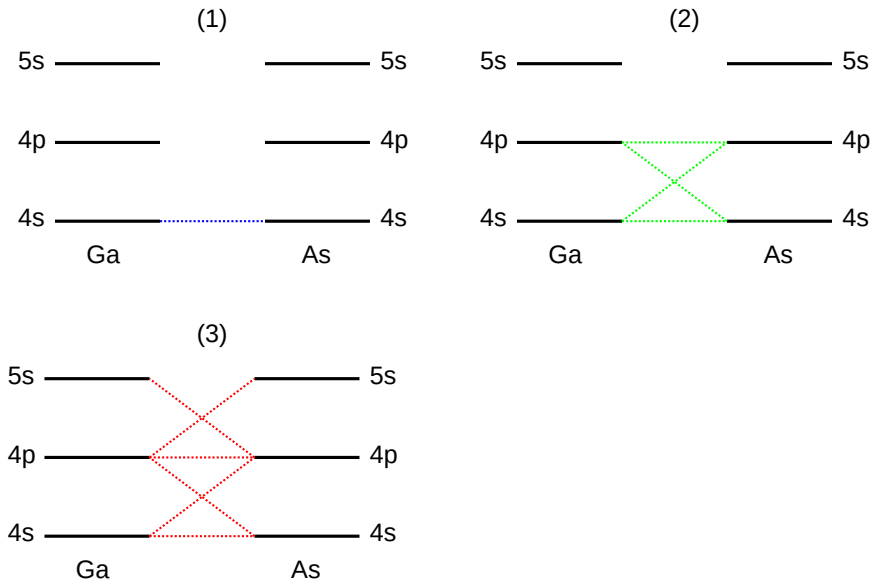

Figure 2.10: Schematic of the coupling between Ga and As atom for the restricted hopping terms.

By including the effect of the spin-orbit coupling, one now need to diagonalize the (20×20) Hamiltonian given by

$$H_0 = \begin{array}{c} \\ \langle\uparrow| \\ \langle\downarrow| \end{array} \begin{array}{c} \begin{array}{cc} |\uparrow\rangle & |\downarrow\rangle \end{array} \\ \begin{pmatrix} h(\boldsymbol{k}) & 0 \\ 0 & h(\boldsymbol{k}) \end{pmatrix} \end{array} + H_{\text{so}} \tag{2.28}$$

where $h(\boldsymbol{k})$ is the (10×10) Hamiltonian in Eq. (2.13).

Figure 2.12 shows the bandstructure of GaAs including the effect of spin-orbit coupling.

2.3.1 Eigenstates at the Γ-point

As we discussed in the previous section, the 4s-, 4p-, and 5s-orbitals are decoupled at the Γ-point. In the presence of spin-orbit coupling, the p-orbital ($l = 1$) states are further decoupled into the $j = 3/2$ and $j = 1/2$ states. We have summarized the eigenstates at the Γ-point for the p-like

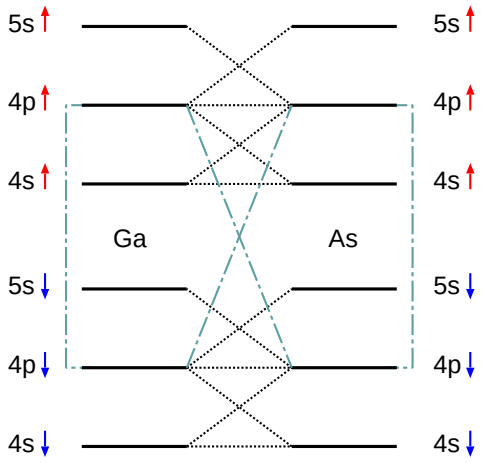

Figure 2.11: Schematic of the coupling between Ga and As atom in the presence of spin-orbit coupling. The up and down spin states of 4p-orbitals are coupled by spin-orbit coupling.

conduction band (Γ_{8c}, Γ_{7c}), the conduction band (Γ_{6c}), and the valence band (Γ_{8v}, Γ_{7v}) in Table. 2.2 [9].

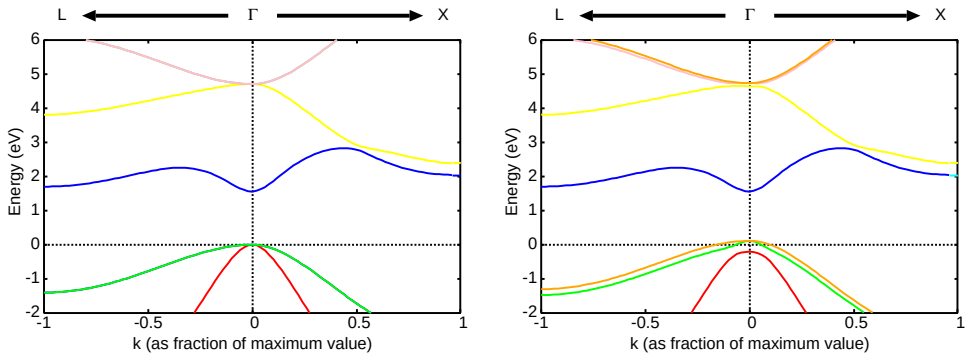

Figure 2.12: The bandstructre of GaAs. Left: without spin-orbit coupling (as same as Fig. 2.6). Right: with spin-orbit coupling. The spin-orbit coupling induces the band splitting in the valence band and the p-like conduction band at the Γ-point.

2.4 Eigenstate basis

So far, we have shown that the band structure can be obtained by diagonalizing the $\boldsymbol{k}$-dependent 20×20 Hamiltonian for each value of $\boldsymbol{k}$. However, our main interest is the conduction band in the vicinity of the Γ-point. In this case, it is convenient to rewrite the Hamiltonian by the basis of eigenstates at the Γ-point instead of orbital states. In the eigenstate representation, the coupling between bands are well described by the $\boldsymbol{k}\cdot\boldsymbol{P}$ model or the envelope function approximation (EFA) [9],

$$\sum_{n',\sigma'} \quad \left\{ \left[E_{n'} + \frac{(\hbar\boldsymbol{k} + e\boldsymbol{A})^2}{2m} + U \right] \delta_{nn'}\delta_{\sigma\sigma'} + \frac{g_0}{2}\mu_B \boldsymbol{\sigma}\cdot\boldsymbol{B}\delta_{nn'} \right. \\ \left. + \frac{1}{m}(\hbar\boldsymbol{k} + e\boldsymbol{A})\cdot\boldsymbol{P}_{nn'}\delta_{\sigma\sigma'} + \Delta_{n\sigma,n'\sigma'} \right\} c_{n'\sigma'} = E c_{n\sigma} \tag{2.29}$$

where

$$\boldsymbol{P}_{nn'} = \langle n|\,\boldsymbol{p}\,|n'\rangle \tag{2.30}$$

$$\Delta_{n\sigma,n'\sigma'} = \frac{\hbar}{4m^2c^2}\langle n\sigma|\,\boldsymbol{p}\cdot(\boldsymbol{\sigma}\times(\nabla V_0))\,|n'\sigma'\rangle\,. \tag{2.31}$$

Here E_n denotes the eigen energy at the Γ-point for the band n, $\boldsymbol{P}_{nn'}$ is the momentum matrix element between the band n and n', and $\Delta_{n\sigma,n'\sigma'}$ is the

Γ_{8c}	$\left\vert \frac{3}{2} \quad \frac{3}{2} \right\rangle_{c'}$	$=$	$-\frac{1}{\sqrt{2}}$	$\left\vert \begin{matrix} X'+iY' \\ 0 \end{matrix} \right\rangle$	$\left\vert \frac{3}{2} \quad \frac{1}{2} \right\rangle_{c'}$	$=$	$\frac{1}{\sqrt{6}}$	$\left\vert \begin{matrix} 2Z' \\ -(X'+iY') \end{matrix} \right\rangle$
	$\left\vert \frac{3}{2} \quad -\frac{1}{2} \right\rangle_{c'}$	$=$	$\frac{1}{\sqrt{6}}$	$\left\vert \begin{matrix} X'-iY' \\ 2Z' \end{matrix} \right\rangle$	$\left\vert \frac{3}{2} \quad -\frac{3}{2} \right\rangle_{c'}$	$=$	$\frac{1}{\sqrt{2}}$	$\left\vert \begin{matrix} 0 \\ X'-iY \end{matrix} \right\rangle$
Γ_{7c}	$\left\vert \frac{1}{2} \quad \frac{1}{2} \right\rangle_{c'}$	$=$	$-\frac{1}{\sqrt{3}}$	$\left\vert \begin{matrix} Z' \\ X'+iY' \end{matrix} \right\rangle$	$\left\vert \frac{1}{2} \quad -\frac{1}{2} \right\rangle_{c'}$	$=$	$-\frac{1}{\sqrt{3}}$	$\left\vert \begin{matrix} X'-iY' \\ -Z' \end{matrix} \right\rangle$
Γ_{6c}	$\left\vert \frac{1}{2} \quad \frac{1}{2} \right\rangle_{c}$	$=$		$\left\vert \begin{matrix} S \\ 0 \end{matrix} \right\rangle$	$\left\vert \frac{1}{2} \quad -\frac{1}{2} \right\rangle_{c}$	$=$		$\left\vert \begin{matrix} 0 \\ S \end{matrix} \right\rangle$
Γ_{8v}	$\left\vert \frac{3}{2} \quad \frac{3}{2} \right\rangle_{v}$	$=$	$-\frac{1}{\sqrt{2}}$	$\left\vert \begin{matrix} X+iY \\ 0 \end{matrix} \right\rangle$	$\left\vert \frac{3}{2} \quad \frac{1}{2} \right\rangle_{v}$	$=$	$\frac{1}{\sqrt{6}}$	$\left\vert \begin{matrix} 2Z \\ -(X+iY) \end{matrix} \right\rangle$
	$\left\vert \frac{3}{2} \quad -\frac{1}{2} \right\rangle_{v}$	$=$	$\frac{1}{\sqrt{6}}$	$\left\vert \begin{matrix} X-iY \\ 2Z \end{matrix} \right\rangle$	$\left\vert \frac{3}{2} \quad -\frac{3}{2} \right\rangle_{v}$	$=$	$\frac{1}{\sqrt{2}}$	$\left\vert \begin{matrix} 0 \\ X-iY \end{matrix} \right\rangle$
Γ_{7v}	$\left\vert \frac{1}{2} \quad \frac{1}{2} \right\rangle_{v}$	$=$	$-\frac{1}{\sqrt{3}}$	$\left\vert \begin{matrix} Z \\ X+iY \end{matrix} \right\rangle$	$\left\vert \frac{1}{2} \quad -\frac{1}{2} \right\rangle_{v}$	$=$	$-\frac{1}{\sqrt{3}}$	$\left\vert \begin{matrix} X-iY \\ -Z \end{matrix} \right\rangle$

Table 2.2: Eigenstates at the Γ-point for the p-like conduction band (Γ_{8c}, Γ_{7c}), the conduction band (Γ_{6c}), and the valence band (Γ_{8v}, Γ_{7v}).

matrix element of spin-orbit interaction. The V_0 denotes a rapidly oscillating microscopic lattice-periodic potential while U represents a slowly varying potential over a whole sample.

Each bands are weakly coupled for the small value of $\boldsymbol{k}$ so that one can decouple the conduction band from the other bands by using the Löwdin partitioning (perturbation). After the perturbation, one can finally obtain the 2×2 effective Hamiltonian for the conduction band.

2.5 Calculation of effective Hamiltonian

In this section, we will show how to obtain the effective Hamiltonian for the particular band around the particular k. Let us consider the 3×3 k-dependent Hamiltonian $h(k)$ for example. Assume that we are interested in the band A in the vicinity of $k = k_0$ as shown in Fig. 2.13.

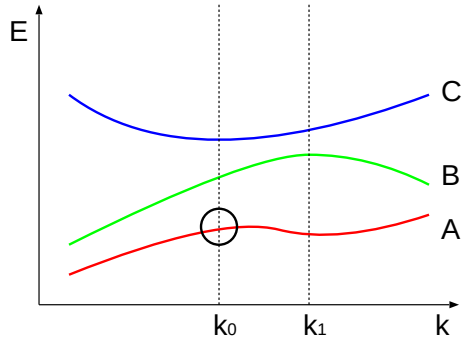

Figure 2.13: Schematic dispersion relation. We are interested in the band A in the vicinity of $k = k_0$.

The Hamiltonian at $k = k_0$ can be written by

$$h(k_0) = \begin{array}{c} \\ \langle a_0| \\ \langle b_0| \\ \langle c_0| \end{array} \begin{array}{c} \begin{array}{ccc} |a_0\rangle & |b_0\rangle & |c_0\rangle \end{array} \\ \begin{pmatrix} E_{A0} & 0 & 0 \\ 0 & E_{B0} & 0 \\ 0 & 0 & E_{C0} \end{pmatrix} \end{array} \tag{2.32}$$

where $|a_0\rangle$, $|b_0\rangle$, and $|c_0\rangle$ are eigenstates of $h(k_0)$. Similarly, one can write

down the Hamiltonian at $k = k_1$ as

$$h(k_1) = \begin{array}{c} \\ \langle a_1| \\ \langle b_1| \\ \langle c_1| \end{array} \begin{array}{c} \begin{array}{ccc} |a_1\rangle & |b_1\rangle & |c_1\rangle \end{array} \\ \begin{pmatrix} E_{A1} & 0 & 0 \\ 0 & E_{B1} & 0 \\ 0 & 0 & E_{C1} \end{pmatrix} \end{array} \tag{2.33}$$

where $|a_1\rangle$, $|b_1\rangle$, and $|c_1\rangle$ are eigenstates of $h(k_1)$. The important point is that this Hamiltonian can be also written by $|a_0\rangle$, $|b_0\rangle$, and $|c_0\rangle$ as

$$h(k_1) = \begin{array}{c} \\ \langle a_0| \\ \langle b_0| \\ \langle c_0| \end{array} \begin{array}{c} \begin{array}{ccc} |a_0\rangle & |b_0\rangle & |c_0\rangle \end{array} \\ \begin{pmatrix} H_{AA} & H_{AB} & H_{AC} \\ H_{BA} & H_{BB} & H_{BC} \\ H_{CA} & H_{CB} & H_{CC} \end{pmatrix} \end{array}, \tag{2.34}$$

since each set of eigenstates gives a complete and orthonormal set of the basis. One can further rewrite the Hamiltonian by $h(k_0)$ and the additional term,

$$h(k_1) = h(k_0) + \lambda h'(k_1) = H(\lambda) \tag{2.35}$$

$$= \begin{pmatrix} E_{A0} + \lambda x_{AA} & \lambda x_{AB} & \lambda x_{AC} \\ \lambda x_{BA} & E_{B0} + \lambda x_{BB} & \lambda x_{BC} \\ \lambda x_{CA} & \lambda x_{CB} & E_{C0} + \lambda x_{CC} \end{pmatrix} \tag{2.36}$$

where λ denotes the strength of coupling and $h'(k_1)$ the matrix elements between each bands.

If $k_0 \simeq k_1$, each bands are weakly coupled ($\lambda \ll 1$) so that one can separate them by perturbation. By applying the unitary transformation, one can decouple the band A from the others as (Fig. 2.14)

$$\tilde{H}(\lambda) = U(\lambda) H(\lambda) U^{\dagger}(\lambda) \tag{2.37}$$

$$= \begin{pmatrix} \tilde{H}_{AA} & 0 & 0 \\ 0 & \tilde{H}_{BB} & \tilde{H}_{BC} \\ 0 & \tilde{H}_{CB} & \tilde{H}_{CC} \end{pmatrix}. \tag{2.38}$$

The effective Hamiltonian for the band A around $k = k_0$ is then given by

$$\tilde{H}_{AA} = H_{AA}^{(0)} + \lambda H_{AA}^{(1)} + \lambda^2 H_{AA}^{(2)} + \lambda^3 H_{AA}^{(3)} + \cdots \tag{2.39}$$

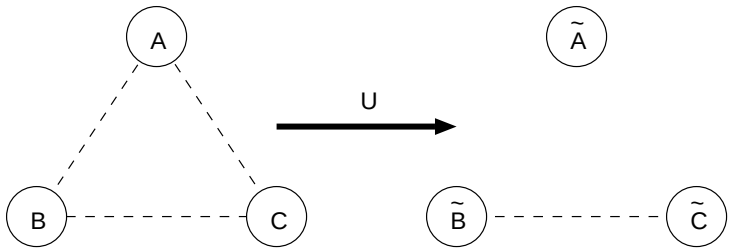

Figure 2.14: Schematic of weakly coupled systems. The focused system (A) can be decoupled from the others (B and C) by the unitary transformation.

for any order of λ. This decoupling of the system in interest from other systems are called Löwdin partitioning [9].

We have summarized the value of $H_{AA}^{(i)}$ up to $i = 3$,

$$H_{AA}^{(0)} = E_{A0} \tag{2.40}$$

$$H_{AA}^{(1)} = x_{AA} \tag{2.41}$$

$$H_{AA}^{(2)} = \sum_{l=B,C} \frac{x_{Al}x_{lA}}{E_A - E_l} \tag{2.42}$$

$$H_{AA}^{(3)} = \sum_{l,l'} \frac{x_{Al}x_{ll'}x_{l'A}}{(E_A - E_l)(E_A - E_{l'})} - \sum_{l} \frac{x_{Al}x_{lA}x_{AA} + x_{AA}x_{Al}x_{lA}}{2(E_A - E_l)^2} \tag{2.43}$$

In general, an effective Hamiltonian is given by [9],

$$H_{mm'}^{(0)} = H_{mm'}^{0} \tag{2.44}$$

$$H_{mm'}^{(1)} = H'_{mm'} \tag{2.45}$$

$$H_{mm'}^{(2)} = \frac{1}{2}\sum_{l} H'_{ml}H'_{lm'}\left[\frac{1}{E_m - E_l} + \frac{1}{E'_m - E_l}\right] \tag{2.46}$$

$$\begin{aligned} H_{mm'}^{(3)} &= \frac{1}{2}\sum_{l,l'} H'_{ml}H'_{ll'}H'_{l'm'}\left[\frac{1}{(E_m - E_l)(E_m - E'_l)} + \frac{1}{(E'_m - E_l)(E'_m - E'_l)}\right] \\ &- \frac{1}{2}\sum_{l,m''}\left[\frac{H'_{ml}H'_{lm''}H'_{m''m'}}{(E_{m'} - E_l)(E_{m''} - E_l)} + \frac{H'_{mm''}H'_{m''l}H'_{lm'}}{(E_m - E_l)(E_{m''} - E_l)}\right]. \end{aligned} \tag{2.47}$$

where the indices m, m', m'' correspond to states in the focused band, and l, l', l'' correspond to states in the other bands.

2.6 Relativistic effect

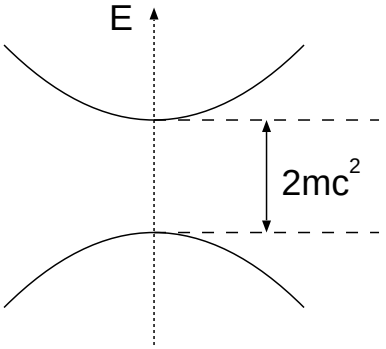

Figure 2.15: Schematic band structure for the Dirac equation.

Before dealing with the multi-band Hamiltonian for semiconductor systems, we would like to review how the effective Hamiltonian for the positive energy branch can be derived from the Dirac equation.

The Hamiltonian in the Dirac equation is defined by [12]

$$H = \begin{array}{c} \\ \langle + | \\ \langle - | \end{array} \begin{array}{c} \begin{array}{cc} |+\rangle & |-\rangle \end{array} \\ \begin{pmatrix} mc^2 + U & c\boldsymbol{\sigma} \cdot \boldsymbol{p'} \\ c\boldsymbol{\sigma} \cdot \boldsymbol{p'} & -mc^2 + U \end{pmatrix} \end{array} \tag{2.48}$$

where $\boldsymbol{p'} = \boldsymbol{p} + e\boldsymbol{A}$.

In the third order perturbation, the effective Hamiltonian for the positive energy branch in the vicinity of $\boldsymbol{p} = 0$ can be calculated as

$$\tilde{H}_{++} = H_{++}^{(0)} + H_{++}^{(1)} + H_{++}^{(2)} + H_{++}^{(3)} \tag{2.49}$$

where

$$H_{++}^{(0)} = mc^2 \tag{2.50}$$

$$H_{++}^{(1)} = U \tag{2.51}$$

$$H_{++}^{(2)} = \frac{c^2}{2mc^2}(\boldsymbol{\sigma} \cdot \boldsymbol{p'})(\boldsymbol{\sigma} \cdot \boldsymbol{p'}) \tag{2.52}$$

$$= \frac{\boldsymbol{p'}^2}{2m} + \frac{e\hbar}{2m}\boldsymbol{\sigma} \cdot (\nabla \times \boldsymbol{A}) \tag{2.53}$$

$$
\begin{aligned}
H_{++}^{(3)} &= \frac{c^2}{(2mc^2)^2}\frac{2(\boldsymbol{\sigma}\cdot\boldsymbol{p'})U(\boldsymbol{\sigma}\cdot\boldsymbol{p'}) - \{U(\boldsymbol{\sigma}\cdot\boldsymbol{p'})(\boldsymbol{\sigma}\cdot\boldsymbol{p'}) + (\boldsymbol{\sigma}\cdot\boldsymbol{p'})(\boldsymbol{\sigma}\cdot\boldsymbol{p'})U\}}{2} \\
&= -\frac{\hbar}{4m^2c^2}\boldsymbol{\sigma}\cdot(\boldsymbol{p'}\times\nabla U) + \frac{\hbar^2}{8m^2c^2}\Delta U. \qquad (2.54)
\end{aligned}
$$

Here, we have used the following relations,

$$
\begin{aligned}
(\boldsymbol{\sigma}\cdot\boldsymbol{A})(\boldsymbol{\sigma}\cdot\boldsymbol{B}) &= \boldsymbol{A}\cdot\boldsymbol{B} + i\boldsymbol{\sigma}\cdot(\boldsymbol{A}\times\boldsymbol{B}) \qquad (2.55)\\
2\boldsymbol{ABA} - (\boldsymbol{BAA} + \boldsymbol{AAB}) &= [[\boldsymbol{A},\boldsymbol{B}],\boldsymbol{A}] \qquad (2.56)\\
\left[\boldsymbol{r}_i, \boldsymbol{p}_j\right] &= i\hbar\delta_{ij}. \qquad (2.57)
\end{aligned}
$$

One can rewrite the effective Hamiltonian as

$$
\tilde{H}_{++} = mc^2 + U + \frac{\boldsymbol{p'}^2}{2m} + \frac{g_0}{2}\mu_B\boldsymbol{\sigma}\cdot\boldsymbol{B} + \frac{\lambda_{\rm so}}{\hbar}\boldsymbol{\sigma}\cdot(\boldsymbol{p'}\times\nabla U) + \frac{\hbar^2}{8m^2c^2}\Delta U, \quad (2.58)
$$

where

$$
\boldsymbol{B} = \nabla\times\boldsymbol{A} \qquad (2.59)
$$

and

$$
\begin{aligned}
g_0 &= 2 \qquad (2.60)\\
\mu_B &= \frac{e\hbar}{2m} \qquad (2.61)\\
\lambda_{\rm so} &= -\frac{\hbar^2}{4m^2c^2}. \qquad (2.62)
\end{aligned}
$$

The band gap, the Bohr magneton, and the strength of the spin-orbit coupling are estimated as

$$
\begin{aligned}
2mc^2 &\simeq 1\mathrm{MeV}\,, \qquad (2.63)\\
\mu_B &\simeq 9.27\times10^{-24}\mathrm{JT}^{-1}\,, \qquad (2.64)\\
\lambda_{\rm so} &\simeq -3.7\times10^{-6}\mathrm{\AA}^2\,, \qquad (2.65)
\end{aligned}
$$

respectively.

2.7 Effective Hamiltonian for conduction band

The main properties of electrons in semiconductors are well described only by considering the coupling between the conduction and valence band. The

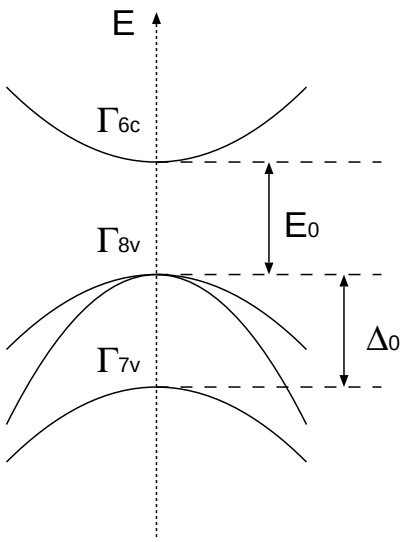

Figure 2.16: Schematic band structure for the 8×8 Kane model.

multi-band Hamiltonian is given by 8×8 Kane model,

$$H_{8\times 8} = \begin{pmatrix} H_{6c6c} & H_{6c8v} & H_{6c7v} \\ H_{8v6c} & H_{8v8v} & H_{8v7v} \\ H_{7v6c} & H_{7v8v} & H_{7v7v} \end{pmatrix}. \tag{2.66}$$

In the third order perturbation, the effective Hamiltonian for the conduction band can be calculated as [9]

$$\tilde{H}_{6c6c} = H^{(0)}_{6c6c} + H^{(1)}_{6c6c} + H^{(2)}_{6c6c} + H^{(3)}_{6c6c} \tag{2.67}$$

with

$$H^{(0)}_{6c6c} = E_c \tag{2.68}$$

$$H^{(1)}_{6c6c} = U + \frac{\hbar^2 \boldsymbol{k'}^2}{2m} + \frac{g_0}{2}\mu_B \boldsymbol{\sigma}\cdot\boldsymbol{B} \tag{2.69}$$

$$\begin{aligned} H^{(2)}_{6c6c} &= \frac{\hbar^2}{m^2}\sum_{|8v\rangle}\frac{(\boldsymbol{k'}\cdot\boldsymbol{P}_{6c8v})(\boldsymbol{k'}\cdot\boldsymbol{P}_{8v6c})}{E_0} + \frac{\hbar^2}{m^2}\sum_{|7v\rangle}\frac{(\boldsymbol{k'}\cdot\boldsymbol{P}_{6c7v})(\boldsymbol{k'}\cdot\boldsymbol{P}_{7v6c})}{E_0+\Delta_0} \\ &= \frac{P^2}{3}\left(\frac{2}{E_0} + \frac{1}{E_0+\Delta_0}\right)\boldsymbol{k'}^2 - \frac{eP^2}{3\hbar}\left(\frac{1}{E_0} - \frac{1}{E_0+\Delta_0}\right)\boldsymbol{\sigma}\cdot\boldsymbol{B} \end{aligned} \tag{2.70}$$

$$
\begin{aligned}
H^{(3)}_{6c6c} & \\
&= \frac{\hbar^2}{m^2}\sum_{|8v\rangle}\frac{2(\boldsymbol{k'}\cdot\boldsymbol{P}_{6c8v})U(\boldsymbol{k'}\cdot\boldsymbol{P}_{8v6c})-\{U(\boldsymbol{k'}\cdot\boldsymbol{P}_{6c8v})(\boldsymbol{k'}\cdot\boldsymbol{P}_{8v6c})+(\boldsymbol{k'}\cdot\boldsymbol{P}_{6c8v})(\boldsymbol{k'}\cdot\boldsymbol{P}_{8v6c})U\}}{2E_0^2} \\
&+ \frac{\hbar^2}{m^2}\sum_{|7v\rangle}\frac{2(\boldsymbol{k'}\cdot\boldsymbol{P}_{6c7v})U(\boldsymbol{k'}\cdot\boldsymbol{P}_{7v6c})-\{U(\boldsymbol{k'}\cdot\boldsymbol{P}_{6c7v})(\boldsymbol{k'}\cdot\boldsymbol{P}_{7v6c})+(\boldsymbol{k'}\cdot\boldsymbol{P}_{6c7v})(\boldsymbol{k'}\cdot\boldsymbol{P}_{7v6c})U\}}{2(E_0+\Delta_0)^2} \\
&= \frac{P^2}{3}\left(\frac{1}{E_0^2}-\frac{1}{(E_0+\Delta_0)^2}\right)\boldsymbol{\sigma}\cdot(\boldsymbol{k'}\times\nabla U)+\frac{P^2}{6}\left(\frac{2}{E_0^2}+\frac{1}{(E_0+\Delta_0)^2}\right)\Delta U
\end{aligned}
\tag{2.71}
$$

where

$$
\boldsymbol{k'} = \boldsymbol{k}+\frac{e}{\hbar}\boldsymbol{A} \tag{2.72}
$$

and

$$
P = \frac{\hbar}{m}\langle S|\, p_x\,|X\rangle\,. \tag{2.73}
$$

One can rewrite the effective Hamiltonian as

$$
\tilde{H}_{6c6c} = E_c + U + \frac{\hbar^2\boldsymbol{k'}^2}{2m^*}+\frac{g^*}{2}\mu_B\boldsymbol{\sigma}\cdot\boldsymbol{B}+\frac{a_{46}}{e}\boldsymbol{\sigma}\cdot(\boldsymbol{k'}\times\nabla U)+\gamma\Delta U \tag{2.74}
$$

where

$$
\begin{aligned}
\frac{m}{m^*} &= 1+\frac{2m}{\hbar^2}\frac{P^2}{3}\left(\frac{2}{E_0}+\frac{1}{E_0+\Delta_0}\right) && (2.75)\\
\frac{g^*}{2} &= \frac{g_0}{2}-\frac{2m}{\hbar^2}\frac{P^2}{3}\left(\frac{1}{E_0}-\frac{1}{E_0+\Delta_0}\right) && (2.76)\\
a_{46} &= \frac{eP^2}{3}\left(\frac{1}{E_0^2}-\frac{1}{(E_0+\Delta_0)^2}\right) && (2.77)\\
\gamma &= \frac{P^2}{6}\left(\frac{2}{E_0^2}+\frac{1}{(E_0+\Delta_0)^2}\right). && (2.78)
\end{aligned}
$$

The band parameters for typical Ⅲ-Ⅴ semiconductors are summarized in Table 2.3 in comparison with those of free electrons in the Dirac equation [9].

2.8 Dresselhaus spin-orbit coupling

Let us consider the effect of the p-like conduction band (Γ_{7c}, Γ_{8c}) in addition to the valence band (Γ_{7v}, Γ_{8v}). The multi-band Hamiltonian is given by the

	unit	GaAs	InAs	InSb	free e^-
E_0	eV	1.519	0.418	0.237	$\simeq 10^6$
Δ_0	eV	0.341	0.380	0.810	-
m^*	m	0.0665	0.0229	0.0139	1
g^*	-	-0.44	-14.9	-51.56	2
a_{46}	eÅ^2	5.206	117.1	523.0	-3.7 $\times 10^{-6}$

Table 2.3: Band parameters for typical Ⅲ -V semiconductors.

14×14 Kane model,

$$H_{14\times 14} = \begin{pmatrix} H_{6c6c} & H_{6c8v} & H_{6c7v} & H_{6c7c} & H_{6c8c} \\ H_{8v6c} & H_{8v8v} & H_{8v7v} & H_{8v7c} & H_{8v8c} \\ H_{7v6c} & H_{7v8v} & H_{7v7v} & H_{7v7c} & H_{7v8c} \\ H_{7c6c} & H_{7c8v} & H_{7c7v} & H_{7c7c} & H_{7c8c} \\ H_{8c6c} & H_{8c8v} & H_{8c7v} & H_{8c7c} & H_{8c8c} \end{pmatrix}. \tag{2.79}$$

One can calculate the effective Hamiltonian for the conduction band in the third order perturbation as [9]

$$\tilde{H}_{6c6c} = H^{(0)}_{6c6c} + H^{(1)}_{6c6c} + H^{(2)}_{6c6c} + H^{(3)}_{6c6c}. \tag{2.80}$$

The third order perturbation gives

$$\begin{aligned} H^{(3)}_{6c6c} &= \frac{\hbar^3}{m^3} \sum_{|8v\rangle} \sum_{|7c\rangle} \frac{(\boldsymbol{k'} \cdot \boldsymbol{P}_{6c8v})(\boldsymbol{k'} \cdot \boldsymbol{P}_{8v7c})(\boldsymbol{k'} \cdot \boldsymbol{P}_{7c6c})}{E_0(E_0 - E'_0)} \\ &+ \frac{\hbar^3}{m^3} \sum_{|7v\rangle} \sum_{|8c\rangle} \frac{(\boldsymbol{k'} \cdot \boldsymbol{P}_{6c7v})(\boldsymbol{k'} \cdot \boldsymbol{P}_{7v8c})(\boldsymbol{k'} \cdot \boldsymbol{P}_{8c6c})}{(E_0 + \Delta_0)(E_0 - E'_0 - \Delta'_0)} \\ &= a_{42} \left[\sigma_x \{k'_x, k'^2_y - k'^2_z\} + \sigma_y \{k'_y, k'^2_z - k'^2_x\} + \sigma_z \{k'_z, k'^2_x - k'^2_y\} \right] \end{aligned} \tag{2.81}$$

where

$$\boldsymbol{k'} = \boldsymbol{k} + \frac{e}{\hbar} \boldsymbol{A} \tag{2.82}$$

$$a_{42} = -\frac{4i}{3} PP'Q \left[\frac{1}{(E_0 + \Delta_0)(E_0 - E'_0 - \Delta'_0)} - \frac{1}{E_0(E_0 - E'_0)} \right] \tag{2.83}$$

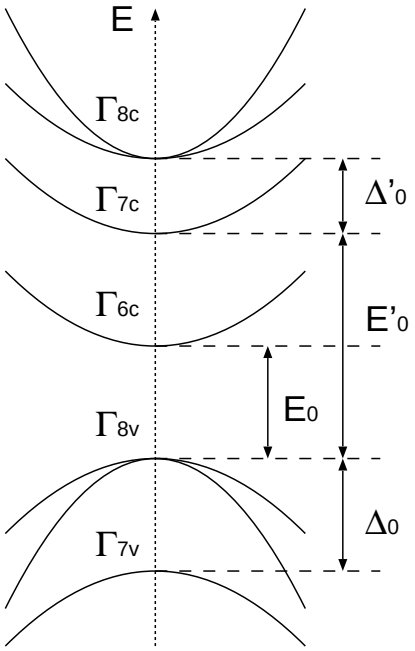

Figure 2.17: Schematic band structure for the 14×14 extended Kane model.

$$\{A, B\} = \frac{1}{2}(AB + BA) \tag{2.84}$$

$$P' = \frac{\hbar}{m} \langle S | p_x | X' \rangle \tag{2.85}$$

$$Q = \frac{\hbar}{m} \langle X | p_y | Z' \rangle . \tag{2.86}$$

Here we have taken the directions of coordinates as $\hat{x} = [100]$, $\hat{y} = [010]$, and $\hat{z} = [001]$. The above term that arises from the third order perturbation is called the Dresselhaus spin-orbit coupling [13]. We have summarized the strength of Dresselhaus coupling for typical Ⅲ -V semiconductors in Table 2.4 [9].

	unit	GaAs	InAs	InSb
a_{42}	eÅ^3	27.58	27.18	760.1

Table 2.4: The strength of Dresselhaus spin-orbit coupling for typical Ⅲ -V semiconductors.

Chapter 3

Two-dimensional systems

In this chapter, we derive the Hamiltonian for two-dimensional electron systems from the effective Hamiltonian in the previous chapter and discuss the basic properties induced by spin-orbit coupling. The asymmetric confinement results in the so-called Rashba spin-orbit coupling (RSO). For the Dresselhaus spin-orbit coupling (DSO), we have considered the confinement in the [001] direction and only focused on the k-linear term. This Hamiltonian for 2DES in the presence of RSO and DSO is a starting point of our investigation. We have further described it in the matrix representation by using the discrete lattice model for numerical simulations. The spin orientation at the Fermi energy and the spin-dependnet effective magnetic field induced by spin-orbit coupling are also discussed.

3.1 Rashba spin-orbit coupling

Let us separate the potential term as

$$U(\boldsymbol{r}) = U_1(x,y) + U_2(z). \tag{3.1}$$

From Eq. (2.74), the effective Hamiltonian for the conduction band in the absence of magnetic field can be written by

$$\begin{aligned}\tilde{H}_{6c6c} &= E_c + U_1 + U_2 + \frac{\hbar^2 \boldsymbol{k}^2}{2m^*} + \gamma\left(\frac{\partial^2 U_1}{\partial x^2} + \frac{\partial^2 U_1}{\partial y^2} + \frac{\partial^2 U_2}{\partial z^2}\right) \\ &+ \frac{a_{46}}{e}\sigma_z\left(k_x\frac{\partial U_1}{\partial y} - k_y\frac{\partial U_1}{\partial x}\right) + \frac{a_{46}}{e}k_z\left(\frac{\partial U_1}{\partial x}\sigma_y - \frac{\partial U_1}{\partial y}\sigma_x\right)\end{aligned}$$

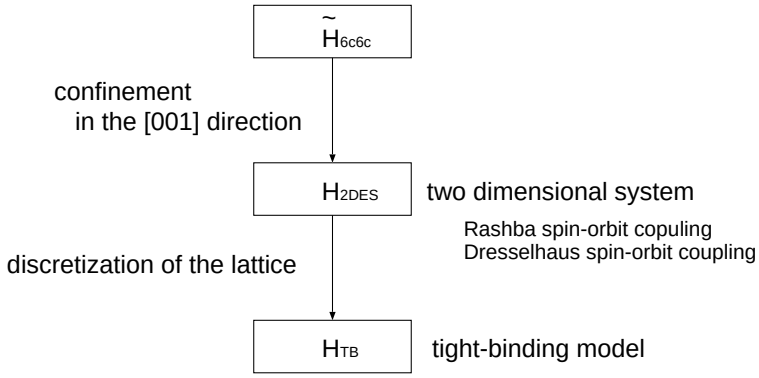

Figure 3.1: Flowchart of deriving the effective Hamiltonian for two-dimensional systems.

$$+ \quad \frac{a_{46}}{e}\frac{\partial U_2}{\partial z}(\sigma_x k_y - \sigma_y k_x). \tag{3.2}$$

By taking the average of the z-dependent operators, one can obtain the Hamiltonian for two-dimensional electron systems (2DES),

$$\begin{aligned} H_{\rm 2DES} &= E_c + U_1 + \langle U_2 \rangle + \frac{\hbar^2(k_x^2+k_y^2)}{2m^*} + \frac{\hbar^2\langle k_z^2\rangle}{2m^*} \\ &+ \gamma\left(\frac{\partial^2 U_1}{\partial x^2} + \frac{\partial^2 U_1}{\partial y^2}\right) + \gamma\left\langle\frac{\partial^2 U_2}{\partial z^2}\right\rangle + \frac{a_{46}}{e}\sigma_z\left(k_x\frac{\partial U_1}{\partial y} - k_y\frac{\partial U_1}{\partial x}\right) \\ &+ \left\langle\frac{a_{46}}{e}\frac{\partial U_2}{\partial z}\right\rangle(\sigma_x k_y - \sigma_y k_x) \end{aligned} \tag{3.3}$$

where $\langle k_z\rangle = 0$. Here we replace k_z by $\partial/i\partial z$. We also note that the band parameters are modified by the confinement. More delicate approach can be found in Ref. [14]. The last term in Eq. (3.3) is called Rashba spin-orbit coupling (RSO) [1].

In this thesis, we have defined the Rashba Hamiltonian as

$$H_{\rm rso} = \frac{\alpha}{\hbar}(\sigma_x p_y - \sigma_y p_x) \tag{3.4}$$

where

$$\alpha = \left\langle\frac{a_{46}}{e}\frac{\partial U_2}{\partial z}\right\rangle. \tag{3.5}$$

3.2 Dresselhaus spin-orbit coupling

3.2.1 Confinement in the [001] direction

From Eq. (2.81), the Dresselhaus spin-orbit coupling (DSO) in 2DES confined in the [001] direction is given by

$$H^{(3)}_{\mathrm{2DES[001]}} = -a_{42}\left\langle k_z^2 \right\rangle (\sigma_x k_x - \sigma_y k_y) + a_{42} k_x k_y (\sigma_x k_y - \sigma_y k_x). \tag{3.6}$$

In this thesis, we have ignored the second term in Eq. (3.6) and defined the Dresselhaus Hamiltonian as

$$H_{\mathrm{dso}} = \frac{\beta}{\hbar}(\sigma_x p_x - \sigma_y p_y) \tag{3.7}$$

where

$$\beta = -a_{42}\left\langle k_z^2 \right\rangle. \tag{3.8}$$

We have compared the strength of RSO and DSO for typical Ⅲ-V semiconductors (Table 3.1). We note that this is a rough estimation since we directly use the band parameters for three-dimensional system (Table. 2.3). The accurate values must be evaluated by experiments. Still, these values are useful to know the order of the strength and explain why RSO is dominant in InAs while is comparable with DSO in GaAs.

	unit	GaAs	InAs	InSb
α	meVÅ	5.206	117.1	523.0
β	meVÅ	-9.93	-9.78	-273.6

Table 3.1: The comparison of the strength of Rashba and Dresselhaus spin-orbit couplings in 2DES. We use the band parameters a_{46} and a_{42} in Table. 2.3 and assume $\langle \partial U_2/\partial z \rangle = 1$ mVÅ^{-1} [2] and $\langle k_z^2 \rangle = 3.6 \times 10^{-4}$ Å^{-2} [15] for evaluating α and β.

3.2.2 Confinement in the [110] direction

If one choose the direction of confinement as [110] instead of [001], DSO in 2DES can be given by

$$H^{(3)}_{\mathrm{2DES[110]}} = a_{42}\left\{\frac{\langle k_z^2 \rangle}{2} - \frac{k_x^2}{2} + k_y^2\right\} k_x \sigma_z \tag{3.9}$$

where we set $\hat{x} = [1\bar{1}0]$, $\hat{y} = [001]$, and $\hat{z} = [110]$. In contrast to the DSO confined in the [001] direction, the DSO in the [110] direction does not induce effective in-plane magnetic field [15]. In other words, the spin precession can be suppressed in this confinement. Especially, the DSO in the [110] direction can be erased when a current is flowing in the y- ([001]) direction [16].

3.3 Effect of potential curvature

From Eq. (3.3), the Hamiltonian for 2DES confined in symmetric potential is given by

$$H = \frac{\hbar^2 \boldsymbol{k}^2}{2m^*} + \frac{a_{46}}{e}\sigma_z \left(k_x \frac{\partial U_1}{\partial y} - k_y \frac{\partial U_1}{\partial x} \right) + U_1 + \gamma \Delta U_1. \tag{3.10}$$

One can rewrite the Hamiltonian as

$$H = \frac{\hbar^2}{2m^*} \left(\boldsymbol{k} + \frac{e}{\hbar}\tilde{\boldsymbol{A}} \right)^2 - \frac{m^* a_{46}^2}{2e^2\hbar^2} \left[\left(\frac{\partial U_1}{\partial x} \right)^2 + \left(\frac{\partial U_1}{\partial y} \right)^2 \right] + U_1 + \gamma \Delta U_1 \tag{3.11}$$

where

$$\tilde{\boldsymbol{A}} = \frac{m^* a_{46}\sigma_z}{e^2\hbar} \left(\frac{\partial U_1}{\partial y}, -\frac{\partial U_1}{\partial x}, 0 \right). \tag{3.12}$$

This effective vector potential corresponds to the effective magnetic field,

$$\tilde{\boldsymbol{B}} = \nabla \times \tilde{\boldsymbol{A}} \tag{3.13}$$

$$= \left(0, 0, -\frac{m^* a_{46}\sigma_z}{e^2\hbar} \Delta U_1 \right). \tag{3.14}$$

This implies that electrons feel spin-dependent effective magnetic field depending on the curvature of potential.

The simplest example of this effect is a quasi one-dimensional wire with parabolic confinement. The parabolic confinement $U_1(y) = m\omega^2 y^2/2$ results in the effective magnetic field proportional to $m\omega^2\sigma_z$. Spin accumulation due to this effective field has been reported by several numerical investigations [17, 18, 19, 20].

3.4 Matrix representation of Hamiltonian

In order to perform numerical simulations, we would like to represent the Hamiltonian by matrix based on the discrete lattice (tight-binding) model.

Let us consider the Hamiltonian with RSO and DSO,

$$H = \frac{p^2}{2m^*} + \frac{\alpha}{\hbar}(\sigma_x p_y - \sigma_y p_x) + \frac{\beta}{\hbar}(\sigma_x p_x - \sigma_y p_y). \tag{3.15}$$

This Hamiltonian can be separated in the x- and y-directions as

$$H = H_x + H_y \tag{3.16}$$

where

$$H_x = \frac{p_x^2}{2m^*} + \frac{-\alpha\sigma_y + \beta\sigma_x}{\hbar} p_x \tag{3.17}$$

and

$$H_y = \frac{p_y^2}{2m^*} + \frac{\alpha\sigma_x - \beta\sigma_y}{\hbar} p_y. \tag{3.18}$$

In the discrete lattice model, the kinetic term in Eq.(3.17) can be given by [21]

$$\frac{p_x^2}{2m^*} = 2V_0 - V_0 \begin{pmatrix} 1 & 0 \\ 0 & 1 \end{pmatrix} (|i\rangle \langle i+\hat{x}| + |i\rangle \langle i-\hat{x}|) \tag{3.19}$$

where $V_0 = \hbar^2/2m^*a^2$ with the unit lattice spacing a. The spin-orbit term can be given by

$$\begin{aligned} \frac{-\alpha\sigma_y + \beta\sigma_x}{\hbar} p_x &= 2V_0 a(-\theta\sigma_y + \phi\sigma_x) \frac{|i\rangle \langle i+\hat{x}| - |i\rangle \langle i-\hat{x}|}{2ia} \\ &= -V_0(-i\theta\sigma_y + i\phi\sigma_x)(|i\rangle \langle i+\hat{x}| - |i\rangle \langle i-\hat{x}|) \\ &= -V_0 \begin{pmatrix} 0 & -\theta + i\phi \\ \theta + i\phi & 0 \end{pmatrix} (|i\rangle \langle i+\hat{x}| - |i\rangle \langle i-\hat{x}|) \end{aligned} \tag{3.20}$$

where $\alpha = 2\theta V_0 a$ and $\beta = 2\phi V_0 a$.

Now we can describe the Hamiltonian in the x-direction as

$$H_x = 2V_0 - V_{i,i+\hat{x}} - V_{i,i-\hat{x}} \tag{3.21}$$

where

$$V_{i,i+\hat{x}} = V_0 \begin{pmatrix} 1 & -\theta + i\phi \\ \theta + i\phi & 1 \end{pmatrix} \tag{3.22}$$

and

$$V_{i,i-\hat{x}} = V_{i,i+\hat{x}}^{\dagger}. \tag{3.23}$$

Here $V_{i,i+\hat{x}}$ denotes the hopping from the site $i + \hat{x}$ to i.

Similarly, the Hamiltonian in the y-direction can be described by

$$H_y = 2V_0 - V_{i,i+\hat{y}} - V_{i,i-\hat{y}} \tag{3.24}$$

where

$$V_{i,i+\hat{y}} = V_0 \begin{pmatrix} 1 & i\theta - \phi \\ i\theta + \phi & 1 \end{pmatrix} \tag{3.25}$$

and

$$V_{i,i-\hat{y}} = V_{i,i+\hat{y}}^{\dagger}. \tag{3.26}$$

One can summarize the Hamiltonian in the discrete lattice model as

$$H_{\mathrm{TB}} = -\sum_{\langle ij\rangle\sigma\sigma'} V_{i\sigma,j\sigma'} c_{i\sigma}^{\dagger} c_{j\sigma'} \tag{3.27}$$

with $V_{i,i+\hat{x}}$ and $V_{i,i+\hat{y}}$.

3.5 Spin orientation at Fermi energy

In this section, we discuss the spin orientation at the Fermi energy and the spin precession of propagating electrons. Let us consider the Hamiltonian with RSO and DSO,

$$H = \frac{p^2}{2m^*} + \frac{\alpha}{\hbar}\left(\sigma_x p_y - \sigma_y p_x\right) + \frac{\beta}{\hbar}\left(\sigma_x p_x - \sigma_y p_y\right). \tag{3.28}$$

The eigenvalues are given by

$$E_{\pm} = \frac{1}{2m^*}\left(p \pm \frac{m^*}{\hbar}\sqrt{\alpha^2 + \beta^2 + 2\alpha\beta\sin 2\phi}\right)^2 - \frac{m^*}{2\hbar^2}\left(\alpha^2 + \beta^2 + 2\alpha\beta\sin 2\phi\right) \tag{3.29}$$

with the eigen functions,

$$\begin{pmatrix} \uparrow \\ \downarrow \end{pmatrix}_{\pm} = \begin{pmatrix} 1 \\ \pm\frac{\alpha e^{i\widetilde{\phi}}+\beta e^{i\phi}}{\sqrt{\alpha^2+\beta^2+2\alpha\beta\sin 2\phi}} \end{pmatrix} \tag{3.30}$$

where $\phi = \tan^{-1}(p_y/p_x)$ and $\widetilde{\phi} = \pi/2 - \phi$.

The magnitude of momentum at the Fermi energy is given by

$$|p|_{\pm} = \sqrt{2m^*E_F + \frac{m^{*2}}{\hbar^2}(\alpha^2+\beta^2+2\alpha\beta\sin 2\phi)} \mp \frac{m^*}{\hbar}\sqrt{\alpha^2+\beta^2+2\alpha\beta\sin 2\phi}. \tag{3.31}$$

Figure 3.2 shows the spin orientation at the Fermi energy in the presence of RSO and DSO. In the presence of only RSO (A), a transport is isotropic and the direction of effective in-plane magnetic field is always perpendicular to that of propagating electrons. In other words, the spin precession occurs on the plane parallel to the direction of a current. In the presence of only DSO (B), a transport is also isotropic but the direction of effective in-plane magnetic field depends on that of propagating electrons. On the one hand, the plane of spin precession is perpendicular to the direction of a current when the current is flowing along the [100] and [010] directions. On the other hand, the plane of spin precession is parallel to the direction of a current when the current is flowing along the [110] and [$\bar{1}$10] directions.

In the presence of both RSO and DSO (C), a transport becomes anisotropic [22]. If the strength of RSO is equal to DSO, the direction of effective in-plane magnetic field is always parallel to the [$\bar{1}$10] direction. This means that the direction of the spin precession is fixed in the [110] direction. In this case, the diffusion of spin direction induced by impurities (D'yakonov-Perel' relaxation [23]) is suppressed. Schliemann *et.al* have been proposed the non-diffusive spin FET based on this property [24].

3.6 Spin-dependent effective magnetic field

In this section, we will show that RSO and DSO induce the spin-dependent effective magnetic field perpendicular to 2DES. Let us consider the Hamiltonian with RSO and DSO,

$$H = \frac{p^2}{2m^*} + \frac{\alpha}{\hbar}(\sigma_x p_y - \sigma_y p_x) + \frac{\beta}{\hbar}(\sigma_x p_x - \sigma_y p_y). \tag{3.32}$$

Firstly, we derive the effective magnetic field by evaluating the time derivative of velocity operator. The velocity operator can be calculated as

$$v_x = \frac{d}{dt}x = \frac{1}{i\hbar}[x, H] = \frac{p_x}{m^*} + \frac{-\alpha\sigma_y + \beta\sigma_x}{\hbar} \tag{3.33}$$

$$v_y = \frac{d}{dt}y = \frac{1}{i\hbar}[y, H] = \frac{p_y}{m^*} + \frac{\alpha\sigma_x - \beta\sigma_y}{\hbar}. \tag{3.34}$$

It clearly shows that $m^*\boldsymbol{v} \neq \boldsymbol{p}$. Similarly, the time derivative of velocity operator can be calculated as

$$\frac{d}{dt}\boldsymbol{v} = \frac{1}{i\hbar}[\boldsymbol{v}, H] = \frac{e}{m^*}\left[\frac{\boldsymbol{p}}{m^*} \times \tilde{\boldsymbol{B}}\right] \tag{3.35}$$

where

$$\tilde{\boldsymbol{B}} = \left(0, 0, \frac{2m^{*2}(\alpha^2 - \beta^2)}{e\hbar^3}\sigma_z\right). \tag{3.36}$$

Another convenient way of deriving the effective magnetic field is to estimate the flux per plaquette from the Aharanov-Bohm phase. Let us consider the Hamiltonian given by Eq. (3.27). The hopping term can be simplified as

$$V_{i,i+\hat{x}} = V_0 \exp\left[-i(\theta\sigma_y - \phi\sigma_x)\right] \tag{3.37}$$

$$V_{i,i+\hat{y}} = V_0 \exp\left[i(\theta\sigma_x - \phi\sigma_y)\right] \tag{3.38}$$

for an infinitesimal lattice spacing a. Let an electron initially be at (i, j) and consider the closed path as shown in Fig. 3.3,

$$\begin{aligned} C &= V_{i,i+\hat{y}}V_{i,i+\hat{x}}V^\dagger_{i,i+\hat{y}}V^\dagger_{i,i+\hat{x}} \\ &= \exp\left[i(\theta\sigma_x - \phi\sigma_y)\right]\exp\left[-i(\theta\sigma_y - \phi\sigma_x)\right] \\ &\times \exp\left[-i(\theta\sigma_x - \phi\sigma_y)\right]\exp\left[i(\theta\sigma_y - \phi\sigma_x)\right] \\ &\simeq \exp\left[i(\theta+\phi)(\sigma_x - \sigma_y) + i(\theta^2 - \phi^2)\sigma_z\right] \\ &\times \exp\left[-i(\theta+\phi)(\sigma_x - \sigma_y) + i(\theta^2 - \phi^2)\sigma_z\right] \\ &\simeq \exp\left[2i(\theta^2 - \phi^2)\sigma_z\right]. \end{aligned} \tag{3.39}$$

Here we have used the Campbell-Hausdorff formula,

$$\exp(\lambda X)\exp(\lambda Y) = \exp\left(\lambda(X+Y) + \frac{\lambda^2}{2}[X, Y] + O(\lambda^3)\right) \tag{3.40}$$

and have dropped terms higher than λ^2. The acquired phase can be related to an effective magnetic field as

$$2(\theta^2 - \phi^2)\sigma_z = \frac{e}{\hbar}\tilde{B}_z a^2 \tag{3.41}$$

that is,

$$\tilde{B}_z = \frac{2\hbar(\theta^2 - \phi^2)}{ea^2}\sigma_z. \tag{3.42}$$

By substituting $\alpha = 2\theta V_0 a$, $\beta = 2\phi V_0 a$, and $V_0 = \hbar^2/2m^* a^2$, one can obtain

$$\tilde{B}_z = \frac{2m^{*2}(\alpha^2 - \beta^2)}{e\hbar^3}\sigma_z. \tag{3.43}$$

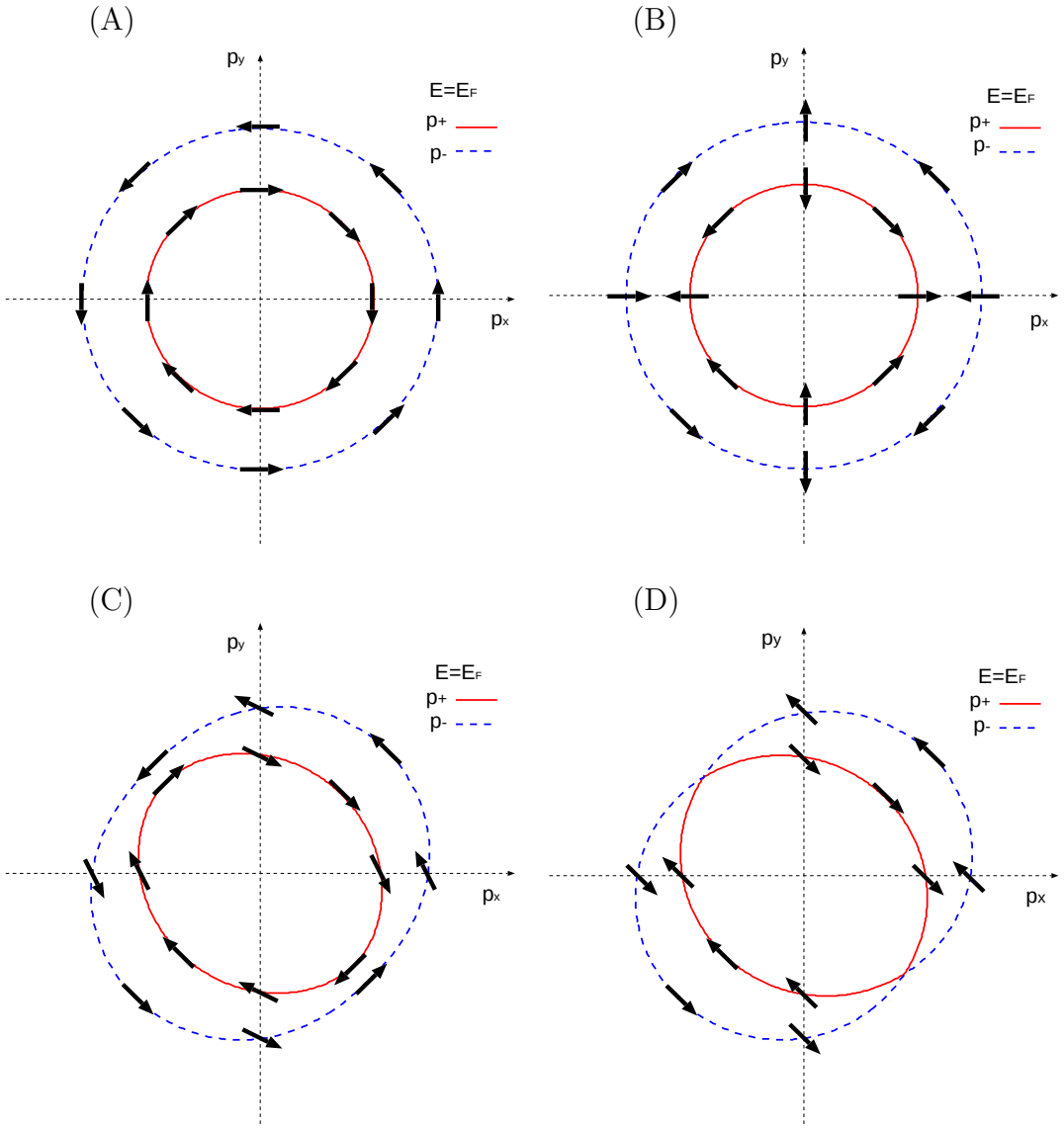

Figure 3.2: Spin orientation at the Fermi energy in the presence of RSO (A), DSO (B), both RSO and DSO (C), the same strength of RSO and DSO (D).

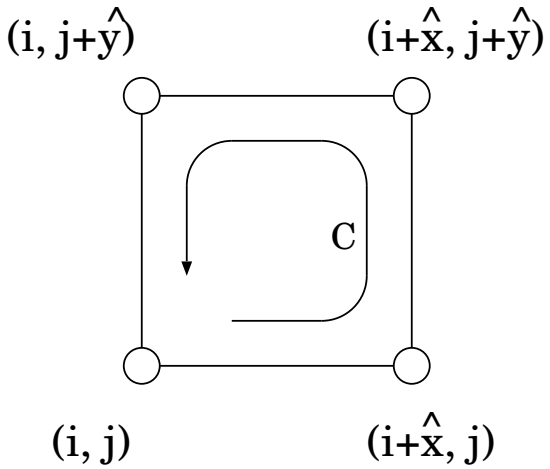

Figure 3.3: Closed path C inside a square lattice.

Chapter 4

Recursive Green function method

The measurement of an electric current is one of the most fundamental experiments in order to investigate material properties. In this chapter, we will introduce the recursive Green function method to calculate the conductance and current distribution in mesoscopic systems for linear response regime. We start with the one-dimensional wire in two-terminal geometry in order to show the basic idea of the Green function method. Then we expand the model to the finite width. Finally, we consider the multi-terminal geometry.

4.1 Two-terminal geometry

4.1.1 One-dimensional wire

Firstly, let us consider an infinite one-dimentioanl (1D) wire as shown in Fig. 4.1. A finite sample region (•) is attached to two reservoirs via semi-infinite ideal probes (○).

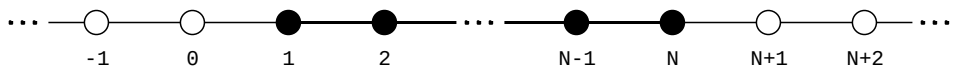

Figure 4.1: Schematic of a one-dimensional wire. Black and white circles represent a sample and ideal probe region, respectively.

The Hamiltonian can be written by

$$\boldsymbol{\mathcal{H}} = \sum_i \mathcal{H}_i a_i^\dagger a_i - \sum_{\langle ij \rangle} V_{ij} a_i^\dagger a_j \,, \tag{4.1}$$

where $a_i^\dagger(a_i)$ denotes the creation (annihilation) operator of an electron on the site i, $\mathcal{H}_i$ the potential on the site i, and V_{ij} the hopping term between the site i and j. The hopping is restricted to nearest neighbors. Here we set

$$\mathcal{H}_i = \begin{cases} \mathcal{H}_i & (1 \le i \le N) \\ \mathcal{H}_0 & (i \le 0, N+1 \le i) \end{cases} \,, \tag{4.2}$$

and

$$V_{i,i+1} \;=\; \begin{cases} V & (1 \le i \le N-1) \\ 1 & (i \le 0, N \le i) \end{cases} \,, \tag{4.3}$$

respectively. The hopping in the reverse direction is given by $V_{i+1,i} = V_{i,i+1}^\dagger$.

The Schrödinger equation in the matrix form can be written by

$$\begin{pmatrix} \ddots & \ddots & & & & & & & \\ \ddots & \mathcal{H}_0 - E & -1 & & & & & & \\ & -1 & \mathcal{H}_1 - E & -V & & & & & \\ & & -V^\dagger & \ddots & \ddots & & & & \\ & & & \ddots & \ddots & -V & & & \\ & & & & -V^\dagger & \mathcal{H}_N - E & -1 & & \\ & & & & & -1 & \mathcal{H}_0 - E & \ddots & \\ & & & & & & \ddots & \ddots & \end{pmatrix} \begin{pmatrix} \vdots \\ c_0 \\ c_1 \\ \vdots \\ \vdots \\ c_N \\ c_{N+1} \\ \vdots \end{pmatrix} = \mathbf{0} \,, \tag{4.4}$$

where E denotes the Fermi energy and c_i the component of the wave function on the cite i. We note that the wave function can be decomposed into the right- and left-going solutions which also satisfy Eq. (4.4).

Let us consider the transport from the left to the right reservoir. The component of the right-going solution on the site -1 can be described by that on the site 0 as

$$\begin{aligned} c_{-1} &= c_{-1}(+) + c_{-1}(-) \\ &= \mathrm{e}^{-ik} c_0(+) + \mathrm{e}^{ik} c_0(-) \\ &= \mathrm{e}^{-ik} c_0(+) + \mathrm{e}^{ik}(c_0 - c_0(+)) \\ &= \mathrm{e}^{ik} c_0 + (\mathrm{e}^{-ik} - \mathrm{e}^{ik}) c_0(+) \,, \end{aligned} \tag{4.5}$$

where the index $+(-)$ represents the right- (left-) going component. The wave number k is given by

$$\cos k = \frac{\mathcal{H}_0 - E}{2}\,, \tag{4.6}$$

where $-2 < E < 2$. One can substitute Eq. (4.5) into Eq. (4.4) for the site 0 as

$$\begin{aligned} -c_{-1} + (\mathcal{H}_0 - E)c_0 - c_1 &= 0 \\ -\{\mathrm{e}^{ik}c_0 + (\mathrm{e}^{-ik} - \mathrm{e}^{ik})c_0(+)\} + (\mathcal{H}_0 - E)c_0 - c_1 &= 0 \\ (\mathcal{H}_0 - \mathrm{e}^{ik} - E)c_0 - c_1 &= (\mathrm{e}^{-ik} - \mathrm{e}^{ik})c_0(+)\,. \end{aligned} \tag{4.7}$$

Similarly, the component of the right-going solution on the site $N+2$ can be described by that on the site $N+1$,

$$\begin{aligned} c_{N+2} &= c_{N+2}(+) \\ &= \mathrm{e}^{ik}c_{N+1}(+) \\ &= \mathrm{e}^{ik}c_{N+1}. \end{aligned} \tag{4.8}$$

By substituting Eq. (4.8) into Eq. (4.4) for the site $N+1$, one can obtain

$$\begin{aligned} -c_N + (\mathcal{H}_0 - E)c_{N+1} - c_{N+2} &= 0 \\ -c_N + (\mathcal{H}_0 - \mathrm{e}^{ik} - E)c_{N+1} &= 0\,. \end{aligned} \tag{4.9}$$

By using Eqs.(4.7) and (4.9), Eq. (4.4) for infinite sites (Fig. 4.1) can be reduced to the equation for finite sites (Fig. 4.2),

$$\begin{pmatrix} \mathcal{H}_0 - \mathrm{e}^{ik} - E & -1 & & & & & \\ -1 & \mathcal{H}_1 - E & -V & & & & \\ & -V^\dagger & \ddots & \ddots & & & \\ & & \ddots & \ddots & -V & & \\ & & & -V^\dagger & \mathcal{H}_N - E & -1 & \\ & & & & -1 & \mathcal{H}_0 - \mathrm{e}^{ik} - E \end{pmatrix} \begin{pmatrix} c_0 \\ c_1 \\ \vdots \\ \vdots \\ c_N \\ c_{N+1} \end{pmatrix} = \begin{pmatrix} (\mathrm{e}^{-ik} - \mathrm{e}^{ik})c_0(+) \\ 0 \\ \vdots \\ \vdots \\ \vdots \\ 0 \end{pmatrix}. \tag{4.10}$$

Now we define the Green function as

$$\boldsymbol{G} \equiv \frac{1}{\boldsymbol{\mathcal{H}}_s + \boldsymbol{\Sigma} - E\boldsymbol{I}}\,, \tag{4.11}$$

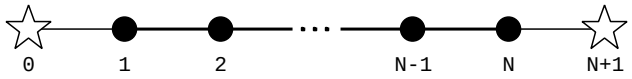

Figure 4.2: Schematic of a finite one-dimensional wire. The effects of semi-infinite ideal probes are included into the sites 0 and $N+1$.

where $\boldsymbol{\mathcal{H}}_s$ denotes the $(N+2)\times(N+2)$ Hamiltonian for the sample region in Eq. (4.10), $\boldsymbol{\Sigma}$ the effect of ideal probes, and $\boldsymbol{I}$ the unit matrix. The matrix element of $\boldsymbol{\Sigma}$ is given by

$$\Sigma_{ij} = \begin{cases} -\mathrm{e}^{ik} & (i=j=0, N+1) \\ 0 & (\text{otherwise}) \end{cases} . \tag{4.12}$$

By multiplying the Green function $\boldsymbol{G}$ to the left-hand side of Eq. (4.10), one can obtain

$$\begin{pmatrix} c_0 \\ c_1 \\ \vdots \\ c_N \\ c_{N+1} \end{pmatrix} = \begin{pmatrix} G(0,0) & \cdots & G(0,N+1) \\ \vdots & \ddots & \vdots \\ G(N+1,0) & \cdots & G(N+1,N+1) \end{pmatrix} \begin{pmatrix} (\mathrm{e}^{-ik}-\mathrm{e}^{ik})c_0(+) \\ 0 \\ \vdots \\ 0 \end{pmatrix} , \tag{4.13}$$

where $G(i,j)$ denotes the matrix element of $\boldsymbol{G}$.

The reflection and transmission coefficients are given by

$$r = \frac{c_0(-)}{c_0(+)} = \frac{c_0}{c_0(+)} - 1 = G(0,0)(\mathrm{e}^{-ik}-\mathrm{e}^{ik}) - 1 , \tag{4.14}$$

$$t = \frac{c_{N+1}(+)}{c_0(+)} = \frac{c_{N+1}}{c_0(+)} = G(N+1,0)(\mathrm{e}^{-ik}-\mathrm{e}^{ik}) , \tag{4.15}$$

while the component of the right-going solution on the site i is given by

$$c_i = G(i,0)(\mathrm{e}^{-ik}-\mathrm{e}^{ik})c_0(+) \qquad \text{for} \quad 1 \le i \le N , \tag{4.16}$$

where one can set $c_0(+)=1$. The current distribution on the site i is given by $|c_i|^2$.

The transport from the right to the left reservoir can be evaluated simply by changing the right-hand side of Eq. (4.10) from

$$\Big((\mathrm{e}^{-ik}-\mathrm{e}^{ik})c_0(+), 0, \cdots, 0\Big)^T , \tag{4.17}$$

to

$$\left(0, \cdots, 0, (\mathrm{e}^{-ik} - \mathrm{e}^{ik}) c'_{N+1}(-)\right)^T , \tag{4.18}$$

where $c'_{N+1}(-)$ denotes the left-going component of the left-going solution at the site $N+1$. We note that this is not the case if the magnetic field exists in ideal probes. More careful treatment is necessary in the presence of magnetic field [25].

We summarize the reflection and transmission coefficients as the scattering matrix,

$$\begin{aligned} \boldsymbol{S} &= \begin{pmatrix} r & t' \\ t & r' \end{pmatrix} \\ &= \begin{pmatrix} G(0,0) & G(0,N+1) \\ G(N+1,0) & G(N+1,N+1) \end{pmatrix} \begin{pmatrix} \mathrm{e}^{-ik} - \mathrm{e}^{ik} & 0 \\ 0 & \mathrm{e}^{-ik} - \mathrm{e}^{ik} \end{pmatrix} - \begin{pmatrix} 1 & 0 \\ 0 & 1 \end{pmatrix} , \end{aligned} \tag{4.19}$$

where r' and t' represent the reflection and transmission coefficients for the left-going transport, respectively. The corresponding right- and left-going solutions are given by

$$c_i = G(i,0)(\mathrm{e}^{-ik} - \mathrm{e}^{ik}) c_0(+) , \tag{4.20}$$

$$c'_i = G(i,N+1)(\mathrm{e}^{-ik} - \mathrm{e}^{ik}) c'_{N+1}(-) , \tag{4.21}$$

where one can set $c_0(+) = c'_{N+1}(-) = 1$.

4.1.2 Quasi one-dimensional wire

Secondly, let us consider an infinite quasi one-dimentioanl (Q1D) wire as shown in Fig. 4.3. The sample region is attached to two reservoirs via semi-infinite ideal probes.

The Hamiltonian can be written by

$$\hat{\boldsymbol{\mathcal{H}}} = \sum_{ij} W_{ij} a^\dagger_{ij} a_{ij} - \sum_{ij} V_{i,i+\hat{x};\,j} a^\dagger_{ij} a_{i+\hat{x},j} - \sum_{ij} V_{i;\,j,j+\hat{y}} a^\dagger_{ij} a_{i,j+\hat{y}} + \text{c.c.} , \tag{4.22}$$

where $a^\dagger_{ij}(a_{ij})$ denotes the creation (annihilation) operator of an electron on the site (i,j), W_{ij} the potential on the site (i,j), $V_{i,i+\hat{x};\,j}(V_{i;\,j,j+\hat{y}})$ the hopping term in the $x(y)$-direction, and c.c the complex conjugate.

We decompose the sample region into a series of the slices along the y-direction (Fig. 4.3). The Hamiltonian can be rewritten as

$$\hat{\boldsymbol{\mathcal{H}}} = \sum_i \boldsymbol{\mathcal{H}}_i - \sum_{ij} V_{i,i+\hat{x};\,j} a^\dagger_{ij} a_{i+\hat{x},j} + \text{c.c.} , \tag{4.23}$$

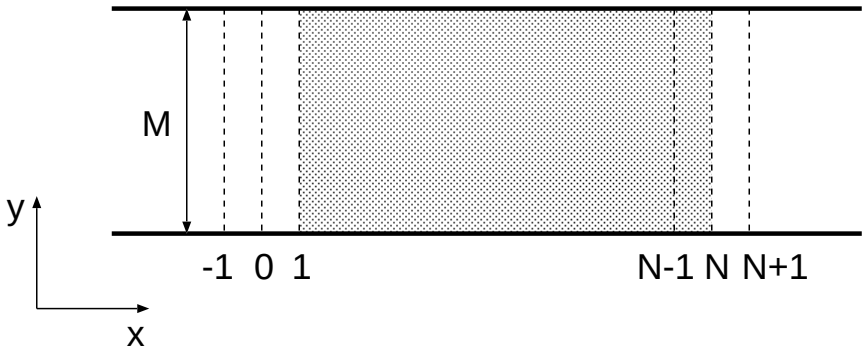

Figure 4.3: Schematic of a quasi one-dimensional wire. Shaded area represents the $N \times M$ sample region.

with

$$\boldsymbol{\mathcal{H}}_i = \sum_j W_{ij} a_{ij}^\dagger a_{ij} - \sum_j V_{i;\,j,j+\hat{y}} a_{ij}^\dagger a_{i,j+\hat{y}} + \text{c.c.}\,. \tag{4.24}$$

Here we set

$$\boldsymbol{\mathcal{H}}_i = \begin{cases} \boldsymbol{\mathcal{H}}_i & (1 \le i \le N) \\ \boldsymbol{\mathcal{H}}_0 & (i \le 0, N+1 \le i) \end{cases}, \tag{4.25}$$

and

$$V_{i,i+\hat{x};\,j} = \begin{cases} V_x & (1 \le i \le N-1) \\ 1 & (i \le 0, N \le i) \end{cases}, \tag{4.26}$$

$$V_{i;\,j,j+\hat{y}} = \begin{cases} V_y & (1 \le i \le N-1) \\ 1 & (i \le 0, N \le i) \end{cases}. \tag{4.27}$$

The Schrödinger equation in the matrix form can be written by

$$\begin{pmatrix} \ddots & \ddots & & & & & & & \\ \ddots & \boldsymbol{\mathcal{H}}_0 - E\boldsymbol{I} & -\boldsymbol{I} & & & & & & \\ & -\boldsymbol{I} & \boldsymbol{\mathcal{H}}_1 - E\boldsymbol{I} & -\boldsymbol{V} & & & & & \\ & & -\boldsymbol{V}^\dagger & \ddots & \ddots & & & & \\ & & & \ddots & \ddots & -\boldsymbol{V} & & & \\ & & & & -\boldsymbol{V}^\dagger & \boldsymbol{\mathcal{H}}_N - E\boldsymbol{I} & -\boldsymbol{I} & & \\ & & & & & -\boldsymbol{I} & \boldsymbol{\mathcal{H}}_0 - E\boldsymbol{I} & \ddots & \\ & & & & & & \ddots & \ddots & \end{pmatrix} \begin{pmatrix} \vdots \\ \boldsymbol{C}_0 \\ \boldsymbol{C}_1 \\ \vdots \\ \vdots \\ \boldsymbol{C}_N \\ \boldsymbol{C}_{N+1} \\ \vdots \end{pmatrix} = \boldsymbol{0}\,,$$

(4.28)

where E denotes the Fermi energy, $\boldsymbol{C}_i = (c_1^i, \cdots, c_M^i)^T$ the M components of the wave function on the slice i, and $\boldsymbol{I}$ the unit matrix. The matrix element of the hopping $\boldsymbol{V}$ is given by $V_{ij} = V_x \delta_{ij}$. We note that the wave function can be decomposed into the right- and left-going solutions which also satisfy Eq. (4.28).

Let us consider the transport from the left to the right reservoir. Firstly, we change the real-space representation of $\boldsymbol{C}_i$ in the ideal probe to the k-space representation $\boldsymbol{D}_i = (d_1^i, \cdots, d_M^i)^T$ as

$$\boldsymbol{D}_i = \boldsymbol{U}_p^\dagger \boldsymbol{C}_i \qquad (i \leq 0, N+1 \leq i)\,, \tag{4.29}$$

with

$$\boldsymbol{U}_p = (\boldsymbol{u}_1, \cdots, \boldsymbol{u}_M)\ , \tag{4.30}$$

where the transverse wave function $\boldsymbol{u}_\mu$ can be obtained by diagonalizing the Hamiltonian in the ideal probe,

$$\boldsymbol{\mathcal{H}}_0 \boldsymbol{u}_\mu = E_\mu^y \boldsymbol{u}_\mu \qquad (\mu = 1, \cdots, M)\,. \tag{4.31}$$

Here E_μ^y denotes the transverse confinement energy of the μ-th channel.

The components of the right-going solution on the slice -1 can be described by those on the slice 0 as

$$\begin{aligned} \boldsymbol{D}_{-1} &= \boldsymbol{D}_{-1}(+) + \boldsymbol{D}_{-1}(-) \\ &= \boldsymbol{\Lambda}^{-1}\boldsymbol{D}_0(+) + \boldsymbol{\Lambda}\boldsymbol{D}_0(-) \\ &= \boldsymbol{\Lambda}^{-1}\boldsymbol{D}_0(+) + \boldsymbol{\Lambda}(\boldsymbol{D}_0 - \boldsymbol{D}_0(+)) \\ &= \boldsymbol{\Lambda}\boldsymbol{D}_0 + (\boldsymbol{\Lambda}^{-1} - \boldsymbol{\Lambda})\boldsymbol{D}_0(+)\,, \end{aligned} \tag{4.32}$$

where the matrix element of $\boldsymbol{\Lambda}$ is given by $\Lambda_{\mu\nu} = \exp(ik_\mu^x)\delta_{\mu\nu}$. Here the index $+(-)$ represents the right- (left-) going component. The wave number k_μ^x of the channel μ is given by

$$\cos k_\mu^x = \frac{E_\mu^y - E}{2}\,, \tag{4.33}$$

where $-4 < E < 4$. Here we note that it is necessary to calculate not only the real number of k_μ^x but also the complex number of it. All wave numbers can be obtained by solving the equation,

$$\lambda_\mu^2 - (E_\mu^y - E)\lambda_\mu + 1 = 0\,, \tag{4.34}$$

where $\lambda_\mu = \exp(ik_\mu^x)$. The real number of k_μ^x corresponds to the propagating mode while the complex number to the evanescent mode. Although the evanescent modes

do not contribute to the conductance, they must be included into $\boldsymbol{\Lambda}$ in order to satisfy the unitarity of the scattering matrix.

In the real-space representation, the components of the right-going solution on the slice -1 can be described as

$$\begin{aligned}\boldsymbol{C}_{-1} &= \boldsymbol{U}_p\boldsymbol{D}_{-1} \\ &= \boldsymbol{U}_p\{\boldsymbol{\Lambda}\boldsymbol{D}_0 + (\boldsymbol{\Lambda}^{-1} - \boldsymbol{\Lambda})\boldsymbol{D}_0(+)\} \\ &= \boldsymbol{U}_p\boldsymbol{\Lambda}\boldsymbol{U}_p^\dagger\boldsymbol{C}_0 + \boldsymbol{U}_p(\boldsymbol{\Lambda}^{-1} - \boldsymbol{\Lambda})\boldsymbol{U}_p^\dagger\boldsymbol{C}_0(+)\,, \end{aligned} \tag{4.35}$$

where we use $\boldsymbol{U}_p^\dagger\boldsymbol{U}_p = \boldsymbol{I}$. By substituting Eq. (4.35) into Eq. (4.28) for the slice 0, one can obtain

$$\begin{aligned} -\boldsymbol{C}_{-1} + (\boldsymbol{\mathcal{H}}_0 - E\boldsymbol{I})\boldsymbol{C}_0 - \boldsymbol{C}_1 &= \boldsymbol{0} \\ -\{\boldsymbol{U}_p\boldsymbol{\Lambda}\boldsymbol{U}_p^\dagger\boldsymbol{C}_0 + \boldsymbol{U}_p(\boldsymbol{\Lambda}^{-1} - \boldsymbol{\Lambda})\boldsymbol{U}_p^\dagger\boldsymbol{C}_0(+)\} + (\boldsymbol{\mathcal{H}}_0 - E\boldsymbol{I})\boldsymbol{C}_0 - \boldsymbol{C}_1 &= \boldsymbol{0} \\ (\boldsymbol{\mathcal{H}}_0 - \boldsymbol{U}_p\boldsymbol{\Lambda}\boldsymbol{U}_p^\dagger - E\boldsymbol{I})\boldsymbol{C}_0 - \boldsymbol{C}_1 &= \boldsymbol{U}_p(\boldsymbol{\Lambda}^{-1} - \boldsymbol{\Lambda})\boldsymbol{U}_p^\dagger\boldsymbol{C}_0(+)\,. \end{aligned} \tag{4.36}$$

Similarly, the components of the right-going solution on the slice $N+2$ can be described by those on the slice $N+1$,

$$\begin{aligned}\boldsymbol{C}_{N+2} &= \boldsymbol{C}_{N+2}(+) \\ &= \boldsymbol{U}_p\boldsymbol{\Lambda}\boldsymbol{U}_p^\dagger\boldsymbol{C}_{N+1}(+) \\ &= \boldsymbol{U}_p\boldsymbol{\Lambda}\boldsymbol{U}_p^\dagger\boldsymbol{C}_{N+1}. \end{aligned} \tag{4.37}$$

By substituting Eq. (4.37) into Eq. (4.28) for the slice $N+1$, one can obtain

$$\begin{aligned} -\boldsymbol{C}_N + (\boldsymbol{\mathcal{H}}_0 - E\boldsymbol{I})\boldsymbol{C}_{N+1} - \boldsymbol{C}_{N+2} &= \boldsymbol{0} \\ -\boldsymbol{C}_N + (\boldsymbol{\mathcal{H}}_0 - \boldsymbol{U}_p\boldsymbol{\Lambda}\boldsymbol{U}_p^\dagger - E\boldsymbol{I})\boldsymbol{C}_{N+1} &= \boldsymbol{0}\,. \end{aligned} \tag{4.38}$$

By using Eqs.(4.36) and (4.38), Eq. (4.28) for infinite slices can be reduced to the equation for finite slices,

$$\begin{pmatrix} \boldsymbol{\mathcal{H}}_0 - \boldsymbol{U}_p\boldsymbol{\Lambda}\boldsymbol{U}_p^\dagger - E\boldsymbol{I} & -\boldsymbol{I} & & & & & \\ -\boldsymbol{I} & \boldsymbol{\mathcal{H}}_1 - E\boldsymbol{I} & -\boldsymbol{V} & & & & \\ & -\boldsymbol{V}^\dagger & \ddots & \ddots & & & \\ & & \ddots & \ddots & -\boldsymbol{V} & & \\ & & & -\boldsymbol{V}^\dagger & \boldsymbol{\mathcal{H}}_N - E\boldsymbol{I} & -\boldsymbol{I} & \\ & & & & -\boldsymbol{I} & \boldsymbol{\mathcal{H}}_0 - \boldsymbol{U}_p\boldsymbol{\Lambda}\boldsymbol{U}_p^\dagger - E\boldsymbol{I} \end{pmatrix} \begin{pmatrix} \boldsymbol{C}_0 \\ \boldsymbol{C}_1 \\ \vdots \\ \vdots \\ \boldsymbol{C}_N \\ \boldsymbol{C}_{N+1} \end{pmatrix}$$

$$= \begin{pmatrix} \boldsymbol{U}_p(\boldsymbol{\Lambda}^{-1} - \boldsymbol{\Lambda})\boldsymbol{U}_p^\dagger\boldsymbol{C}_0(+) \\ \boldsymbol{0} \\ \vdots \\ \vdots \\ \vdots \\ \boldsymbol{0} \end{pmatrix}.$$

(4.39)

Now we define the Green function as

$$\hat{\boldsymbol{G}} \equiv \frac{1}{\hat{\boldsymbol{\mathcal{H}}}_s + \hat{\boldsymbol{\Sigma}} - E\boldsymbol{I}}\,, \tag{4.40}$$

where $\hat{\boldsymbol{\mathcal{H}}}_s$ denotes the $M(N+2) \times M(N+2)$ Hamiltonian for the sample region in Eq. (4.39), $\hat{\boldsymbol{\Sigma}}$ the effect of ideal probes, and $\boldsymbol{I}$ the unit matrix. The $M \times M$ sub-matrix of $\hat{\boldsymbol{\Sigma}}$ is given by

$$\hat{\boldsymbol{\Sigma}}(i,j) = \begin{cases} -\boldsymbol{U}_p \boldsymbol{\Lambda} \boldsymbol{U}_p^\dagger & (i = j = 0, N+1) \\ \boldsymbol{0} & (\text{otherwise}) \end{cases}\,. \tag{4.41}$$

Here we need to invert the $M(N+2)\times M(N+2)$ matrix in order to obtain the Green function $\hat{\boldsymbol{G}}$. However, the direct inversion takes much time especially for a large system since the number of numerical operations required for the inversion of the matrix increases as L^3 with L the size of the matrix. By using the recursive method as shown in the Appendix A, one can obtain the Green function by inverting the $M \times M$ sub-matrices of $\hat{\boldsymbol{G}}$ successively. This approach reduces the operation time significantly.

By multiplying the Green function $\hat{\boldsymbol{G}}$ to the left-hand side of Eq. (4.39), one can obtain

$$\begin{pmatrix} \boldsymbol{C}_0 \\ \boldsymbol{C}_1 \\ \vdots \\ \boldsymbol{C}_N \\ \boldsymbol{C}_{N+1} \end{pmatrix} = \begin{pmatrix} \boldsymbol{G}(0,0) & \cdots & \boldsymbol{G}(0,N+1) \\ \vdots & \ddots & \vdots \\ \boldsymbol{G}(N+1,0) & \cdots & \boldsymbol{G}(N+1,N+1) \end{pmatrix} \begin{pmatrix} \boldsymbol{U}_p(\boldsymbol{\Lambda}^{-1} - \boldsymbol{\Lambda})\boldsymbol{U}_p^\dagger \boldsymbol{C}_0(+) \\ \boldsymbol{0} \\ \vdots \\ \boldsymbol{0} \end{pmatrix}, \tag{4.42}$$

where $\boldsymbol{G}(i,j)$ denotes the $M \times M$ sub-matrix of $\hat{\boldsymbol{G}}$.

The transmission matrix element from the channel ν to μ is given by

$$t_{\mu\nu} = \sqrt{\frac{v_\mu}{v_\nu}} \frac{d_\mu^{N+1}(+)}{d_\nu^0(+)} = \sqrt{\frac{v_\mu}{v_\nu}} \{\boldsymbol{U}_p^\dagger \boldsymbol{G}(N+1,0) \boldsymbol{U}_p (\boldsymbol{\Lambda}^{-1} - \boldsymbol{\Lambda})\}_{\mu\nu}\,, \tag{4.43}$$

where $d_\mu^i(+)$ denotes the right-going components of the right-going solution on the slice i with the channel μ in the k-space representation. The velocity of electrons in the channel μ is given by [21]

$$v_\mu = 2 \sin k_\mu\,. \tag{4.44}$$

The prefactor $\sqrt{v_\mu/v_\nu}$ is necessary since the current amplitude is proportional to the square of the wave function multiplied by the veolocity [21]. Similarly, the reflection matrix from the channel ν to μ is given by

$$r_{\mu\nu} = \sqrt{\frac{v_\mu}{v_\nu}}\frac{d^0_\mu(-)}{d^0_\nu(+)} = \sqrt{\frac{v_\mu}{v_\nu}}\{\boldsymbol{U}_p^\dagger \boldsymbol{G}(0,0)\boldsymbol{U}_p(\boldsymbol{\Lambda}^{-1}-\boldsymbol{\Lambda})-\boldsymbol{I}\}_{\mu\nu}\,. \tag{4.45}$$

The components of the right-going solution on the slice i are given by

$$\boldsymbol{C}_i = \boldsymbol{G}(i,0)\boldsymbol{U}(\boldsymbol{\Lambda}^{-1}-\boldsymbol{\Lambda})\boldsymbol{D}_0(+) \qquad \text{for} \quad 1\le i\le N\,, \tag{4.46}$$

where the matrix element of $\boldsymbol{D}_0(+) = (d^0_1(+),\cdots,d^0_M(+))^T$ is

$$d^0_\mu(+) = \begin{cases} 1 & \text{(propagating mode)} \\ 0 & \text{(decay mode)} \end{cases}\,. \tag{4.47}$$

The current distribution on the slice i is given by $|\boldsymbol{C}_i|^2$.

The transport from the right to the left reservoir can be evaluated simply by changing the right-hand side of Eq. (4.39) from

$$\Big(\boldsymbol{U}_p(\boldsymbol{\Lambda}^{-1}-\boldsymbol{\Lambda})\boldsymbol{U}_p^\dagger \boldsymbol{C}_0(+),0,\cdots,0\Big)^T\,, \tag{4.48}$$

to

$$\Big(0,\cdots,0,\boldsymbol{U}_p(\boldsymbol{\Lambda}^{-1}-\boldsymbol{\Lambda})\boldsymbol{U}_p^\dagger \boldsymbol{C'}_{N+1}(-)\Big)^T\,, \tag{4.49}$$

where $\boldsymbol{C'}_{N+1}(-)$ denotes the left-going component of the left-going solution at the slice $N+1$. We note that this is not the case if the magnetic field presents in ideal probes [25].

We summarize the reflection and transmission matrices as the scattering matrix,

$$\begin{aligned} S_{\mu\nu} &= \begin{pmatrix} \boldsymbol{r} & \boldsymbol{t'} \\ \boldsymbol{t} & \boldsymbol{r'} \end{pmatrix}_{\mu\nu} \\ &= \sqrt{\frac{v_\mu}{v_\nu}}\left\{\begin{pmatrix} \boldsymbol{U}_p^\dagger & \boldsymbol{0} \\ \boldsymbol{0} & \boldsymbol{U}_p^\dagger \end{pmatrix}\begin{pmatrix} \boldsymbol{G}(0,0) & \boldsymbol{G}(0,N+1) \\ \boldsymbol{G}(N+1,0) & \boldsymbol{G}(N+1,N+1) \end{pmatrix}\begin{pmatrix} \boldsymbol{U}_p & \boldsymbol{0} \\ \boldsymbol{0} & \boldsymbol{U}_p \end{pmatrix}\right. \\ &\times \left.\begin{pmatrix} \boldsymbol{\Lambda}^{-1}-\boldsymbol{\Lambda} & 0 \\ 0 & \boldsymbol{\Lambda}^{-1}-\boldsymbol{\Lambda} \end{pmatrix} - \begin{pmatrix} \boldsymbol{I} & \boldsymbol{0} \\ \boldsymbol{0} & \boldsymbol{I} \end{pmatrix}\right\}_{\mu\nu} \end{aligned} \tag{4.50}$$

where $\boldsymbol{r'}$ and $\boldsymbol{t'}$ represent the reflection and transmission matrices for the left-going transport, respectively. The corresponding right- and left-going solutions are given by

$$\boldsymbol{C}_i = \boldsymbol{G}(i,0)\boldsymbol{U}_p(\boldsymbol{\Lambda}^{-1}-\boldsymbol{\Lambda})\boldsymbol{D}_0(+)\,, \tag{4.51}$$

$$\boldsymbol{C'}_i = \boldsymbol{G}(i,N+1)\boldsymbol{U}_p(\boldsymbol{\Lambda}^{-1}-\boldsymbol{\Lambda})\boldsymbol{D'}_{N+1}(-)\,, \tag{4.52}$$

where

$$d^0_\mu(+)\,, d'^{N+1}_\mu(-) = \begin{cases} 1 & \text{(propagating mode)} \\ 0 & \text{(decay mode)} \end{cases} . \tag{4.53}$$

4.2 Multi-terminal geometory

Let us consider the three-terminal geometry as shown in Fig. 4.4. The $N_x \times N_y$ central sample region (C) is attached to three reservoirs via probes (L, R and D). Each probe consists of a semi-infinite ideal region and a finite sample region. The size of the finite sample region is given by $N_p \times M^I$ ($I = L, R$ and D).

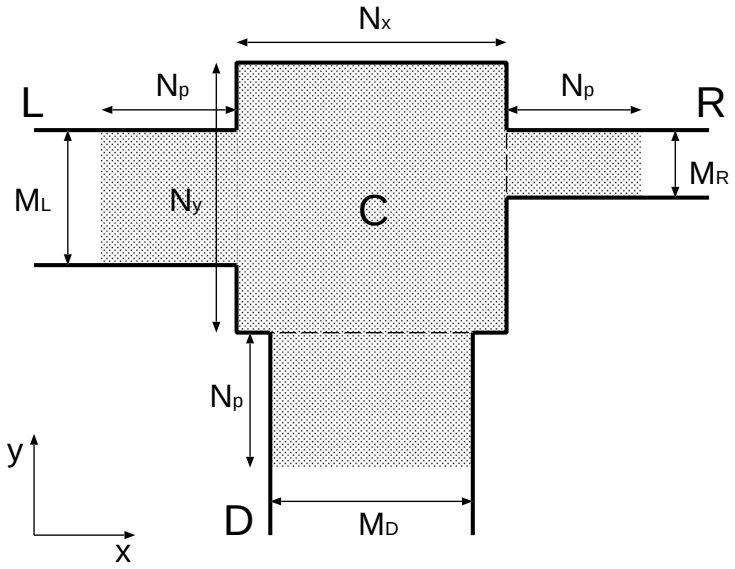

Figure 4.4: Schematic of a three terminal geometry. Shaded area represents the sample region.

The Hamiltonian is given by

$$\hat{\boldsymbol{\mathcal{H}}} = \boldsymbol{\mathcal{H}}_C + \sum_{I=L,R,D} \boldsymbol{\mathcal{H}}^I_P - \boldsymbol{V}_{PC} \tag{4.54}$$

where $\boldsymbol{\mathcal{H}}_C$ denotes the Hamiltonian for the central region (C), $\boldsymbol{\mathcal{H}}^I_P$ the Hamiltonian for the probe I, and $\boldsymbol{V}_{PC}$ the coupling between the probes and central region.

The Hamiltonian for the central region (C) is given by

$$\boldsymbol{\mathcal{H}}_C = \sum_{ij} W_{ij} a_{ij}^\dagger a_{ij} - \sum_{ij} V_{i,i+\hat{x};\,j} a_{ij}^\dagger a_{i+\hat{x},j} - \sum_{ij} V_{i;\,j,j+\hat{y}} a_{ij}^\dagger a_{i,j+\hat{y}} + \text{c.c.}\,, \quad (4.55)$$

where $a_{ij}^\dagger(a_{ij})$ denotes the creation (annihilation) operator of an electron on the site (i,j), W_{ij} the potential on the site (i,j), $V_{i,i+\hat{x};\,j}(V_{i;\,j,j+\hat{y}})$ the hopping term in the $x(y)$-direction, and c.c the complex conjugate. The hopping term is set to be $V_{i,i+\hat{x};\,j} = V_x$ and $V_{i;\,j,j+\hat{y}} = V_y$.

The Hamiltonian for the probe I is given by

$$\boldsymbol{\mathcal{H}}_P^I = \sum_{ij} W_{ij}^I {a_{ij}^I}^\dagger a_{ij}^I - \sum_{ij} V_{i,i+1;\,j}^I {a_{ij}^I}^\dagger a_{i+1,j}^I - \sum_{ij} V_{i;\,j,j+1}^I {a_{ij}^I}^\dagger a_{i,j+1}^I + \text{c.c.}\,, \quad (4.56)$$

where ${a_{ij}^I}^\dagger(a_{ij}^I)$ denotes the creation (annihilation) operator of an electron on the site (i,j), W_{ij}^I the potential on the site (i,j), and $V_{i,i+1;\,j}^I(V_{i;\,j,j+1}^I)$ the hopping term in the longitudinal (transverse) direction in the probe I. We decompose the probe region into a series of the slices along the transverse direction and gather the slices for the same longitudinal cites (Fig. 4.5). The Hamiltonian for the gathered slice is given by

$$\hat{\boldsymbol{\mathcal{H}}}_P = \sum_I \boldsymbol{\mathcal{H}}_P^I = \sum_i \boldsymbol{\mathcal{H}}_i - \sum_i \boldsymbol{V}_{i,i+1} + \text{c.c.}\,, \quad (4.57)$$

with

$$\begin{aligned} \boldsymbol{\mathcal{H}}_i &= \sum_I \sum_j W_{ij}^I {a_{ij}^I}^\dagger a_{ij}^I - \sum_I \sum_j V_{i;\,j,j+1}^I {a_{ij}^I}^\dagger a_{i,j+1}^I + \text{c.c.} \quad (4.58) \\ &= \begin{pmatrix} \boldsymbol{\mathcal{H}}_i^L & \mathbf{0} & \mathbf{0} \\ \mathbf{0} & \boldsymbol{\mathcal{H}}_i^R & \mathbf{0} \\ \mathbf{0} & \mathbf{0} & \boldsymbol{\mathcal{H}}_i^D \end{pmatrix}, \quad (4.59) \end{aligned}$$

and

$$\boldsymbol{V}_{i,i+1} = \sum_I \sum_j V_{i,i+1;\,j}^I {a_{ij}^I}^\dagger a_{i+1,j}^I\,. \quad (4.60)$$

Here we set

$$\boldsymbol{\mathcal{H}}_i = \begin{cases} \boldsymbol{\mathcal{H}}_i & (1 \le i \le N_p) \\ \boldsymbol{\mathcal{H}}_0 & (i \le 0) \end{cases}, \quad (4.61)$$

and

$$\boldsymbol{V}_{i,i+1} = \begin{cases} \boldsymbol{V} & (1 \le i \le N_p - 1) \\ \boldsymbol{I} & (i \le 0) \end{cases}, \quad (4.62)$$

with

$$\boldsymbol{V} = \begin{pmatrix} \boldsymbol{V}^L & \boldsymbol{0} & \boldsymbol{0} \\ \boldsymbol{0} & \boldsymbol{V}^R & \boldsymbol{0} \\ \boldsymbol{0} & \boldsymbol{0} & \boldsymbol{V}^D \end{pmatrix}, \tag{4.63}$$

where the hopping matrix element at each probe is given by $V_{ij}^L = V_x^\dagger \delta_{ij}$, $V_{ij}^R = V_x \delta_{ij}$, and $V_{ij}^D = V_y^\dagger \delta_{ij}$.

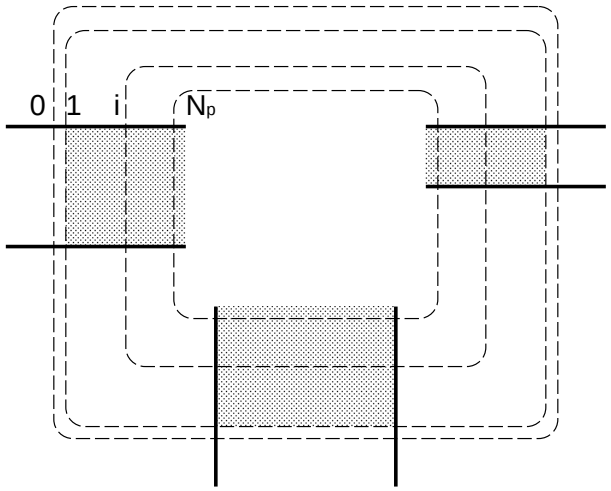

Figure 4.5: Graphical interpretation for the Hamiltonian $\boldsymbol{\mathcal{H}}_i$. The i-th slices of three probes are gathered.

Let us consider the transport from the probe L to R and D. The equation corresponding to Eq. 4.39 in the previous section is given by

$$\begin{pmatrix} \boldsymbol{\mathcal{H}}_0 - \hat{\boldsymbol{U}}_p \hat{\boldsymbol{\Lambda}} \hat{\boldsymbol{U}}_p^\dagger - E\boldsymbol{I} & -\boldsymbol{I} & & & & & \\ -\boldsymbol{I} & \boldsymbol{\mathcal{H}}_1 - E\boldsymbol{I} & -\boldsymbol{V} & & & & \\ & -\boldsymbol{V}^\dagger & \ddots & \ddots & & & \\ & & \ddots & \ddots & -\boldsymbol{V} & & \\ & & & -\boldsymbol{V}^\dagger & \boldsymbol{\mathcal{H}}_{N_p} - E\boldsymbol{I} & -\boldsymbol{V}_{PC} & \\ & & & & -\boldsymbol{V}_{PC}^\dagger & \boldsymbol{\mathcal{H}}_C - E\boldsymbol{I} & \end{pmatrix} \begin{pmatrix} \boldsymbol{C}_0 \\ \boldsymbol{C}_1 \\ \vdots \\ \vdots \\ \boldsymbol{C}_{N_p} \\ \boldsymbol{C}_C \end{pmatrix}$$

$$= \begin{pmatrix} \boldsymbol{Q}^L \boldsymbol{U}_p (\boldsymbol{\Lambda}^{-1} - \boldsymbol{\Lambda}) \boldsymbol{U}_p^\dagger \boldsymbol{C}_0(+) \\ \boldsymbol{0} \\ \vdots \\ \vdots \\ \vdots \\ \boldsymbol{0} \end{pmatrix},$$

(4.64)

where E denotes the Fermi energy and $\boldsymbol{I}$ the unit matrix. The size of the Hamiltonian for the gathered slice $\boldsymbol{\mathcal{H}}_i$ is $(\sum_I M_I)\times(\sum_I M_I)$ while that for the central region $\boldsymbol{\mathcal{H}}_C$ is $N_xN_y \times N_xN_y$. The $\boldsymbol{C}_i = (c^i_{L1}, \cdots, c^i_{LM_L}, c^i_{R1}, \cdots, c^i_{RM_R}, c^i_{D1}, \cdots, c^i_{DM_D})^T$ denotes the $M_L + M_R + M_D$ components of the wave function at the gathered slice i, and $\boldsymbol{C}_C$ the $N_x \times N_y$ components at the central region. The $\boldsymbol{C}_0(+)$ denotes the incoming solution at the gathered slice 0.

The matrix of the Fourier transformation $\hat{\boldsymbol{U}}_p$ is given by

$$\hat{\boldsymbol{U}}_p = \begin{pmatrix} \boldsymbol{U}_L & \boldsymbol{0} & \boldsymbol{0} \\ \boldsymbol{0} & \boldsymbol{U}_R & \boldsymbol{0} \\ \boldsymbol{0} & \boldsymbol{0} & \boldsymbol{U}_D \end{pmatrix} , \tag{4.65}$$

where $\boldsymbol{U}_I$ denotes the set of the transverse wave function in the probe I. The matrix of the ideal channel propagation $\hat{\boldsymbol{\Lambda}}$ is given by

$$\hat{\boldsymbol{\Lambda}} = \begin{pmatrix} \boldsymbol{\Lambda}_L & \boldsymbol{0} & \boldsymbol{0} \\ \boldsymbol{0} & \boldsymbol{\Lambda}_R & \boldsymbol{0} \\ \boldsymbol{0} & \boldsymbol{0} & \boldsymbol{\Lambda}_D \end{pmatrix} , \tag{4.66}$$

with

$$\{\boldsymbol{\Lambda}_I\}_{\mu\nu} = \exp(ik^I_\mu)\delta_{\mu\nu} , \tag{4.67}$$

where k^I_μ denotes the wave number of the channel μ in the probe I.

We define the projection matrix $\boldsymbol{Q}^I$ as

$$Q^L_{ij} = \begin{cases} \delta_{ij} & (i = 1, \cdots, M_L) \\ 0 & (\text{otherwise}) \end{cases} , \tag{4.68}$$

$$Q^R_{ij} = \begin{cases} \delta_{ij} & (i = M_L + 1, \cdots, M_L + M_R) \\ 0 & (\text{otherwise}) \end{cases} , \tag{4.69}$$

$$Q^D_{ij} = \begin{cases} \delta_{ij} & (i = M_L + M_R + 1, \cdots, M_L + M_R + M_D) \\ 0 & (\text{otherwise}) \end{cases} . \tag{4.70}$$

We use $\boldsymbol{Q}^L$ in the Eq. (4.64) since we focus on the transport from the probe L. In the absence of magnetic field at the ideal probe region, the transport from the probe R or D can be simply obtained by replacing $\boldsymbol{Q}^L$ to $\boldsymbol{Q}^R$ or $\boldsymbol{Q}^D$.

Now we define the Green function as

$$\hat{\boldsymbol{G}} \equiv \frac{1}{\hat{\boldsymbol{\mathcal{H}}}_s + \hat{\boldsymbol{\Sigma}} - E\boldsymbol{I}} , \tag{4.71}$$

where $\hat{\boldsymbol{\mathcal{H}}}_s$ denotes the $\{(\sum_I M_I)(N_p+1)+N_xN_y\}\times\{(\sum_I M_I)(N_p+1)+N_xN_y\}$ Hamiltonian for the sample region in Eq. (4.64), $\hat{\boldsymbol{\Sigma}}$ the effect of ideal probes, and $\boldsymbol{I}$ the unit matrix. The sub-matrix of $\hat{\boldsymbol{\Sigma}}$ is given by

$$\hat{\boldsymbol{\Sigma}}(i,j) = \begin{cases} -\hat{\boldsymbol{U}}_p\hat{\boldsymbol{\Lambda}}\hat{\boldsymbol{U}}_p^\dagger & (i=j=0) \\ \boldsymbol{0} & (\text{otherwise}) \end{cases} . \tag{4.72}$$

The Green function can be efficiently calculated by recursive method (see Appendix A).

By multiplying the Green function $\hat{\boldsymbol{G}}$ to the left-hand side of Eq. (4.39), one can obtain

$$\begin{pmatrix} \boldsymbol{C}_0 \\ \boldsymbol{C}_1 \\ \vdots \\ \boldsymbol{C}_{N_p} \\ \boldsymbol{C}_C \end{pmatrix} = \begin{pmatrix} \boldsymbol{G}(0,0) & \cdots & \boldsymbol{G}(0,C) \\ \vdots & \ddots & \vdots \\ \boldsymbol{G}(C,0) & \cdots & \boldsymbol{G}(C,C) \end{pmatrix} \begin{pmatrix} \hat{\boldsymbol{U}}_p(\hat{\boldsymbol{\Lambda}}^{-1}-\hat{\boldsymbol{\Lambda}})\hat{\boldsymbol{U}}_p^\dagger\boldsymbol{C}_0(+) \\ \boldsymbol{0} \\ \vdots \\ \boldsymbol{0} \end{pmatrix} , \tag{4.73}$$

where $\boldsymbol{G}(i,j)$ denotes the sub-matrix of $\hat{\boldsymbol{G}}$.

The scattering matrix element corresponding to the transport from the channel ν in the probe J to the channel μ in the probe I is given by

$$S_{\mu\nu}^{IJ} = \sqrt{\frac{v_\mu^I}{v_\nu^J}} \left\{ \hat{\boldsymbol{U}}_p^\dagger \boldsymbol{G}(0,0) \hat{\boldsymbol{U}}_p (\hat{\boldsymbol{\Lambda}}^{-1} - \hat{\boldsymbol{\Lambda}}) - \boldsymbol{I} \right\}_{\mu\nu}^{IJ} , \tag{4.74}$$

where $v_\mu^I(v_\nu^J)$ denotes the Fermi velocity of an electron at the channel $\mu(\nu)$ in the probe $I(J)$. The incoming solution from the probe I is given by

$$\boldsymbol{C}_i^I = \boldsymbol{G}(i,0)\boldsymbol{Q}^I\hat{\boldsymbol{U}}_p(\hat{\boldsymbol{\Lambda}}^{-1}-\hat{\boldsymbol{\Lambda}})\hat{\boldsymbol{U}}_p^\dagger\boldsymbol{C}_0(+) . \tag{4.75}$$

Chapter 5

Spin-dependent electronic transport in nanowire

In this chapter, we numerically investigate the spin-dependent electron transport through a quasi one-dimensional wire in the presence of Rashba spin-orbit coupling (RSO) and Dresselhaus spin-orbit coupling (DSO). We consider the sample region attached to two reservoirs via ideal probes (Fig. 5.1). The Hamiltonian for the sample region can be written by

$$H = \sum_{i,\sigma} W_i c^\dagger_{i\sigma} c_{i\sigma} - \sum_{\langle ij \rangle\, \sigma\sigma'} V_{i\sigma,j\sigma'} c^\dagger_{i\sigma} c_{j\sigma'} \tag{5.1}$$

with

$$V_{i,i+\hat{x}} = V_0 \begin{pmatrix} 1 & -\theta + i\phi \\ \theta + i\phi & 1 \end{pmatrix} \tag{5.2}$$

and

$$V_{i,i+\hat{y}} = V_0 \begin{pmatrix} 1 & i\theta - \phi \\ i\theta + \phi & 1 \end{pmatrix} \tag{5.3}$$

where W_i denotes the random potential on the site i distributed uniformly in $[-W/2, W/2]$, and $V_{i,i+\hat{x}}(V_{i,i+\hat{y}})$ the hopping matrix elements in x-(y-) directions. The parameters θ and ϕ represent the strengths of RSO and DSO, respectively. We have ignored the spin-orbit coupling induced by the random potential.

In our numerical simulation, we consider four different combinations of RSO and DSO as shown in Table 5.1. We firstly show the energy dependence of the conductance and corresponding spin polarization for the ballistic and diffusive transport. Then we show the charge and spin distribution of the current for the single-channel transport. We also show the dynamics of the wave packet for

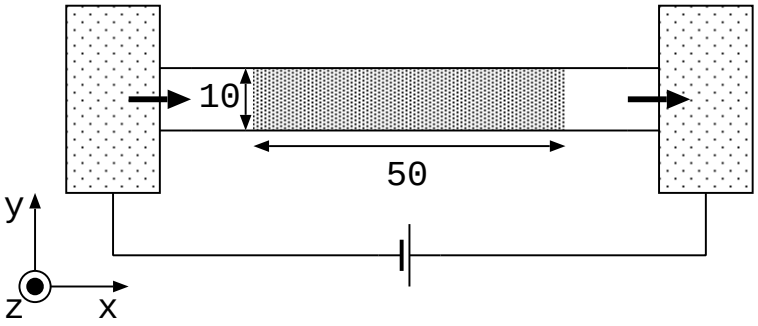

Figure 5.1: Schematic of the quasi one-dimensional wire. Shaded area represents the sample region with Rashba and Dresselhaus spin-orbit couplings.

the same system. Finally we discuss some properties obtained in our numerical simulation by symmetry of the system, self-duality of the scattering-matrix, and *Zitterbewegung*.

	RSO	DSO
A	0.06π	0
B	0	0.06π
C	0.04π	0.02π
D	0.03π	0.03π

Table 5.1: Combinations of Rashba and Dresselhaus spin-orbit couplings.

5.1 Conductance and spin polarization

In this section, we show the energy dependence of the conductance and corresponding spin polarizations. The conductance is defined by the Landauer formula [26]

$$G = G_0 \mathrm{Tr}\, t^\dagger t \tag{5.4}$$

where $G_0 \equiv e^2/h$ is the quantum conductance and t denotes the transmission matrix from the left to the right reservoir. We have calculated the transmission matrix by the recursive Green function method. The corresponding spin polarizations can

be defined by

$$P_i = \frac{\mathrm{Tr}\, t^\dagger \sigma_i t}{\mathrm{Tr}\, t^\dagger t} \tag{5.5}$$

where $\sigma_i\,(i = x, y, z)$ represents the Pauli matrices.

5.1.1 Ballistic transport

Firstly, we study the transport in the absence of impurities ($W = 0$ in Eq. (5.1)). Figure 5.2 shows the energy dependence of the conductance and corresponding spin polarizations in the presence of RSO and DSO. In the presence of RSO (A), the spin polarization in the y-direction can be high at the energies where new channels are opened ($E = -3.68V_0, -3.30V_0, \ldots$). The spin polarizations in the x- and z-directions are equal to zero for any value of energy. A quite similar result can be obtained in the presence of DSO (B) except the direction of the spin polarization is in the x-direction. These properties can be explained by the symmetry of the system (Sec. 5.4). Figure 5.2 (C) shows the result in the presence of RSO and DSO. This result is similar to that of (A) since the strength of RSO is set to be twice as that of DSO. However, there are also small polarizations in the x- and z-directions. If the strength of RSO and DSO is set to be the same (D), no spin polarization can be obtained.

5.1.2 Diffusive transport

Secondly, we study the transport in the presence of impurities (Fig. 5.3). The strength of disorder is set to be $W = 1$ in Eq. (5.1). If the transport is multi-channeled, the spin polarization in any directions can be obtained unless the strength of RSO differs from that of DSO. However, one can not obtain any spin polarization for the energy where only one channel is opened ($-3.91V_0 < E < -3.68V_0$). We will discuss this property in Sec. 5.5. As is the case in the absence of disorder, no spin polarization can be obtained if the strength of RSO is equal to that of DSO (D).

5.2 Charge and spin distribution of current

In this section, we show the charge and spin distribution of a current. We focus on a ballistic transport ($W = 0$ in Eq. (5.1)). The Fermi energy is set to be $E = -3.8V_0$ where only one channel is opened.

A: RSO

Figure 5.4 shows the charge and spin distribution of a current in the presence of RSO. The strength of RSO is set to be $\theta = 0.06\pi$. It is shown that the spin distributions of the x- and z-components are antisymmetric while that for the y-component is symmetric about x-axis (A1). This is due to the symmetry of the system (Sec. 5.4).

(A2) and (A3) show the charge and spin distribution of a current initially having the up- and down-spin components, respectively. They show not only the spin precession but also deflected trajectories. Such trajectories attribute to the spin-dependent effective magnetic field (Sec. 3.6). The combination of the spin precession and the spin-dependent deflection results in the snake motion of a propagating electron. This motion can be regarded as *Zitterbewegung* in semiconductors (Sec. 5.6).

B: DSO

Figure 5.5 shows the charge and spin distribution of a current in the presence of DSO. The strength of DSO is set to be $\phi = 0.06\pi$. It is shown that the spin distributions for the y- and z-components are antisymmetric while that for the x-component is symmetric (B1). (B2) and (B3) show the charge and spin distributions of a current initially having the up- and down-spin components, respectively. In contrast to the presence of RSO, the spin precession occurs in the y-z plane (Sec. 3.5).

C: RSO + DSO

Figure 5.6 shows the charge and spin distribution of a current in the presence of both RSO and DSO. The strengths of RSO and DSO are set to be $\theta = 0.04\pi$ and $\phi = 0.02\pi$, respectively. Spin-dependent deflection of electrons are weaken since the direction of effective magneitc field induced by RSO and DSO are opposite (Sec. 3.6). The magnitude of spin distribution in the z-direction (C1, bottom) is thus smaller than that observed in the presence of either RSO (A1, bottom) or DSO (B1, bottom).

D: RSO = DSO

Figure 5.7 shows the charge and spin distribution of a current for the same strength of RSO and DSO ($\theta = \phi = 0.03\pi$). No spin-dependent deflection (D2, D3) and no spin polarization in the z-direction (D1, bottom) can be observed. This is because the direction of effective magneitc field induced by RSO and DSO cancel out each

other (Sec. 3.6). In addition, the spin precession occurs only for electrons traveling in the $(\hat{x}+\hat{y})$-direction (Sec. 3.5).

5.3 Dynamics of wave packet

In order to visualize the snake motion of propagating electrons, we have numerically investigated the dynamics of the wave packet in this section. We use the higher-order decomposition of exponential operator for calculating the time evolution (see Appendix B).

We consider the isolated system with $(N_x \times N_y) = (150 \times 10)$ (Fig. 5.8). The range of the sample region with RSO is set to be $(51 < N_x < 100)$. The strength of RSO is $\theta = 0.06\pi$.

The initial state of the wave packet is given by

$$|\psi_\chi\rangle = N \mathrm{e}^{ik_x x} \mathrm{e}^{-\left(\frac{\Delta k_x (x-x_0)}{2}\right)^2} \sin k_y y \, |\chi\rangle \tag{5.6}$$

where N is a normalized factor and χ is a spin component. In the following simulation, we set $k_x = 0.35$, $k_y = \pi/N_y + 1$, $\Delta k_x = 0.15$, and $x_0 = 25.5$. We consider the wave packet with up-spin ($\chi = \uparrow$). The time evolution of this wave packet roughly corresponds to the current carrying state for $E = -3.8V_0$ in the previous section.

Fig. 5.8 shows the distribution of charge (upper) and of the spin z-component (lower) at certain times. It clearly shows the snake motion of the wave packet.

One can see the more detailed dynamics of the wave packet as animation in the attached CD. The CD includes the animations for 12 types of dynamics as summarized in Table 5.3. The snapshots shown in this section correspond to the type $A2$.

SO		Initial spin state		
Rashba	Dressehus	-	$\uparrow$	$\downarrow$
0.06π	0	A1	A2	A3
0	0.06π	B1	B2	B3
0.04π	0.02π	C1	C2	C3
0.03π	0.03π	D1	D2	D3

5.4 Spin polarization in symmetric systems

Let us consider the symmetric multi-terminal system in the presence of Rashba spin-orbit coupling (RSO) as shown in Fig. 5.9. The sample region is attached to reservoirs via semi-infinite ideal probes. Here the word "ideal" means that the system including probes is also symmetric. The Hamiltonian is given by

$$\mathcal{H} = \frac{\boldsymbol{p}^2}{2m^*} + \frac{\alpha}{\hbar}(\sigma_x p_y - \sigma_y p_x) + V(|y|)\,. \tag{5.7}$$

where

$$\alpha = \begin{cases} \alpha & \text{(sample region)} \\ 0 & \text{(probe region)} \end{cases} . \tag{5.8}$$

Since the size of the system including probes are infinite, there is an eigenfunction of the Hamiltonian for any value of the Fermi energy, $\mathcal{H}\,|\psi\rangle = E_F\,|\psi\rangle$. This eigenfunction can be decomposed as

$$|\psi\rangle = |\psi_1\rangle + |\psi_2\rangle + |\psi_3\rangle\ , \tag{5.9}$$

where $|\psi_I\rangle$ denotes the incoming solution from the probe I. In the previous section, we have already noted that each of $|\psi_I\rangle$ is also the eigenfunction of the Hamiltonian and the electron injected from the probe I with the energy E_F propagates through the system via the wavefunction $|\psi_I\rangle$.

Now let us focus on the wavefunction $|\psi_1\rangle$. In the coordinate representation, it can be written as

$$\begin{aligned} |\psi_1\rangle &= \int_{-\infty}^{\infty}\int_{-\infty}^{\infty} dxdy c_1(x,y)\chi_1(x,y)\,|x,y\rangle \\ &= \int_{-\infty}^{\infty} dx \int_{0}^{\infty} dy c_1(x,y)\chi_1(x,y)\,|x,y\rangle + c_1(x,-y)\chi_1(x,-y)\,|x,-y\rangle\ , \end{aligned} \tag{5.10}$$

where $c_1(x,y)$ denotes the charge component while $\chi_1(x,y)$ the (2×1) spin component at the coordinate (x,y). Since the system is symmetric about the x-axis, the charge component of $|\psi\rangle_1$ satisfies

$$|c_1(x,y)| = |c_1(x,-y)|\,. \tag{5.11}$$

The considered system with RSO has the following commutation relation,

$$[\mathcal{H},\, \sigma_y S_y] = 0\,, \tag{5.12}$$

where S_y denotes the Parity operator in the y-direction, $S_y\,|x,y\rangle = |x,-y\rangle$. This relation satisfies

$$\sigma_y S_y\,|\psi_1\rangle = \pm\,|\psi_1\rangle\ . \tag{5.13}$$

By substituting Eqs. (5.11) and (5.13) into Eq. (5.10), one can obtain

$$\chi_1(x,y) = \pm\sigma_y\chi_1(x,-y)\,. \tag{5.14}$$

Hence, the local expectation value of the spin x-component at the coordinate (x,y) relates to that at $(x,-y)$ as

$$\begin{aligned}\langle\sigma_x\rangle_{(x,y)} &= |c_1(x,y)|^2\chi_1(x,y)^\dagger\sigma_x\chi_1(x,y)\\ &= -|c_1(x,-y)|^2\chi_1(x,-y)^\dagger\sigma_x\chi_1(x,-y)\\ &= -\langle\sigma_x\rangle_{(x,-y)}\ .\end{aligned} \tag{5.15}$$

Similarly,

$$\langle\sigma_y\rangle_{(x,y)} = \langle\sigma_y\rangle_{(x,-y)}\ , \tag{5.16}$$

$$\langle\sigma_y\rangle_{(x,y)} = -\langle\sigma_z\rangle_{(x,-y)}\ . \tag{5.17}$$

In the presence of Dresselhaus spin-orbit coupling (DSO), the Hamiltonian can be written as

$$\mathcal{H} = \frac{\boldsymbol{p}^2}{2m^*} + \frac{\beta}{\hbar}(\sigma_x p_x - \sigma_y p_y) + V(|y|)\,. \tag{5.18}$$

In this case, the commutation relation is given by

$$[\mathcal{H},\,\sigma_x S_y] = 0\,, \tag{5.19}$$

and the local expectation value of the spin component satisfies

$$\langle\sigma_x\rangle_{(x,y)} = \langle\sigma_x\rangle_{(x,-y)}\ , \tag{5.20}$$

$$\langle\sigma_y\rangle_{(x,y)} = -\langle\sigma_y\rangle_{(x,-y)}\ , \tag{5.21}$$

$$\langle\sigma_y\rangle_{(x,y)} = -\langle\sigma_z\rangle_{(x,-y)}\ . \tag{5.22}$$

In the presence of both RSO and DSO, there is no such a relation of the local expectation value of the spin component.

5.5 Self-duality and single-channel transport

The system with spin-orbit coupling belongs to the symplectic universality class [27]. The scattering matrix in this class has the self-duality property by choosing a proper basis.

The self-duality is defined as follows. If a particular 2×2 spin-dependent element of the scattering matrix is given by

$$S_{ij} = \begin{pmatrix} A & B \\ C & D \end{pmatrix}, \tag{5.23}$$

its reversive elements can be represented as

$$S_{ji} = \begin{pmatrix} D & -B \\ -C & A \end{pmatrix}. \tag{5.24}$$

Now let us consider the spin polarization for the single-channel transport in two-terminal geometry in the symplectic class. In this case, the scattering matrix can be described by the 4×4 matrix,

$$S = \begin{pmatrix} r & t' \\ t & r' \end{pmatrix} = \begin{pmatrix} e & 0 & d & -b \\ 0 & e & -c & a \\ a & b & f & 0 \\ c & d & 0 & f \end{pmatrix}. \tag{5.25}$$

The spin polarization in the x-, y-, and z- directions (5.5) are given by

$$P_x = \frac{ac^* + bd^*}{|a|^2 + |b|^2 + |c|^2 + |d|^2} + \text{c.c} \tag{5.26}$$

$$P_y = \frac{i(ac^* + bd^*)}{|a|^2 + |b|^2 + |c|^2 + |d|^2} - \text{c.c} \tag{5.27}$$

$$P_z = \frac{|a|^2 + |b|^2 - |c|^2 - |d|^2}{|a|^2 + |b|^2 + |c|^2 + |d|^2} \tag{5.28}$$

where c.c denotes the complex conjugate.

On the other hand, the unitarity of the scattering matrix (Eq. (5.25)) gives

$$|a|^2 + |b|^2 - |c|^2 - |d|^2 = 0 \tag{5.29}$$

$$ac^* + bd^* = 0. \tag{5.30}$$

This immediately results in

$$P_i = 0 \tag{5.31}$$

for $i = x, y, z$. This explains that one cannot obtain any spin polarization for the single-channle transport in two-terminal geometory (Sec. 5.1).

5.6 *Zitterbewegung*

Zitterbewegung is the oscillating motion of the electron which is traveling at very high velocity. This is the interference effect between wave functions of the positive and negative energy branch in the Dirac equation (Eq. (2.48)) [12]. As we have already seen in Sec. 2.6, the relativistic spin-orbit coupling originates from the coupling between the positive and negative energy branch. Although the spin-orbit coupling in semiconductors attributes to the coupling between the conduction and valence band, the derived effective Hamiltonian looks the same as the relativistic one. Therefore, one can regard the snake motion of electrons observed in Sec. 5.2 as *Zitterbewegung* in semiconductors.

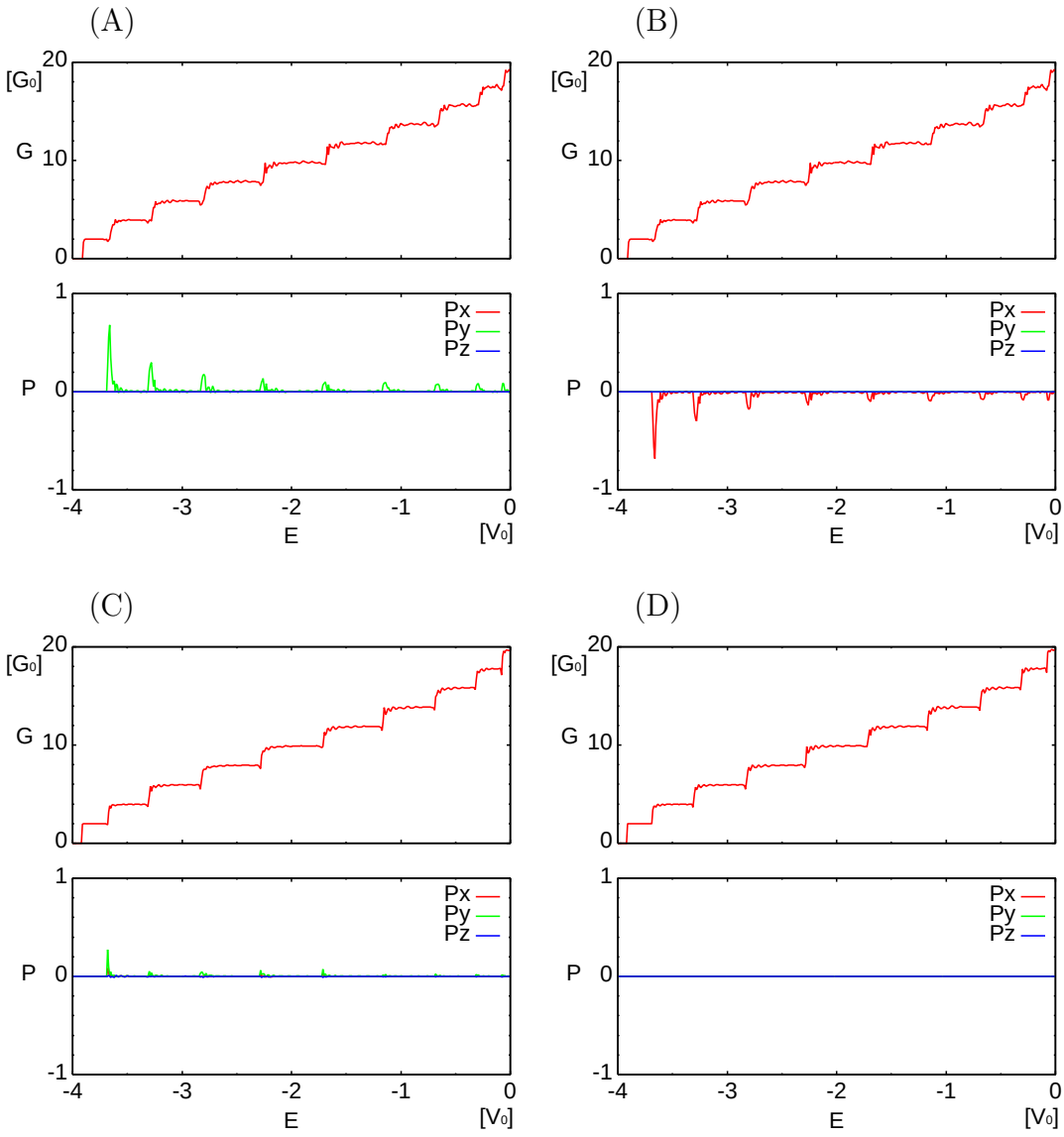

Figure 5.2: Energy dependence of the conductance (upper) and corresponding spin polarizations (lower) in the absence of disorder ($W = 0$). The strengths of RSO (θ) and DSO (ϕ) are set to be as follows. (A) $\theta = 0.06\pi$. (B) $\phi = 0.06\pi$. (C) $\theta = 0.04\pi$ and $\phi = 0.02\pi$. (D) $\theta = \phi = 0.03\pi$.

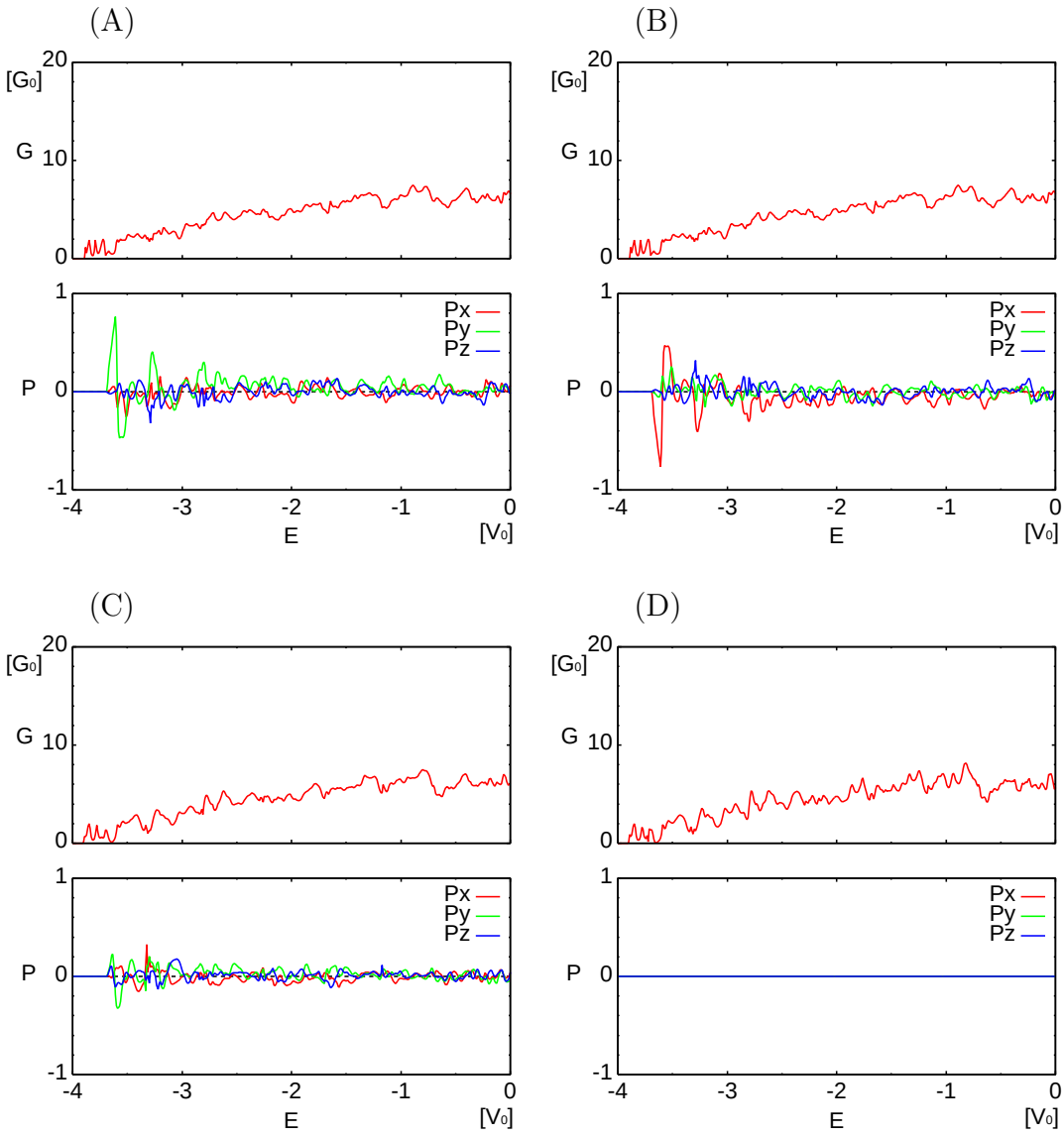

Figure 5.3: Energy dependence of the conductance (upper) and corresponding spin polarizations (lower) in the presence of disorder ($W = 1$). The strengths of RSO (θ) and DSO (ϕ) are set to be as follows. (A) $\theta = 0.06\pi$. (B) $\phi = 0.06\pi$. (C) $\theta = 0.04\pi$ and $\phi = 0.02\pi$. (D) $\theta = \phi = 0.03\pi$.

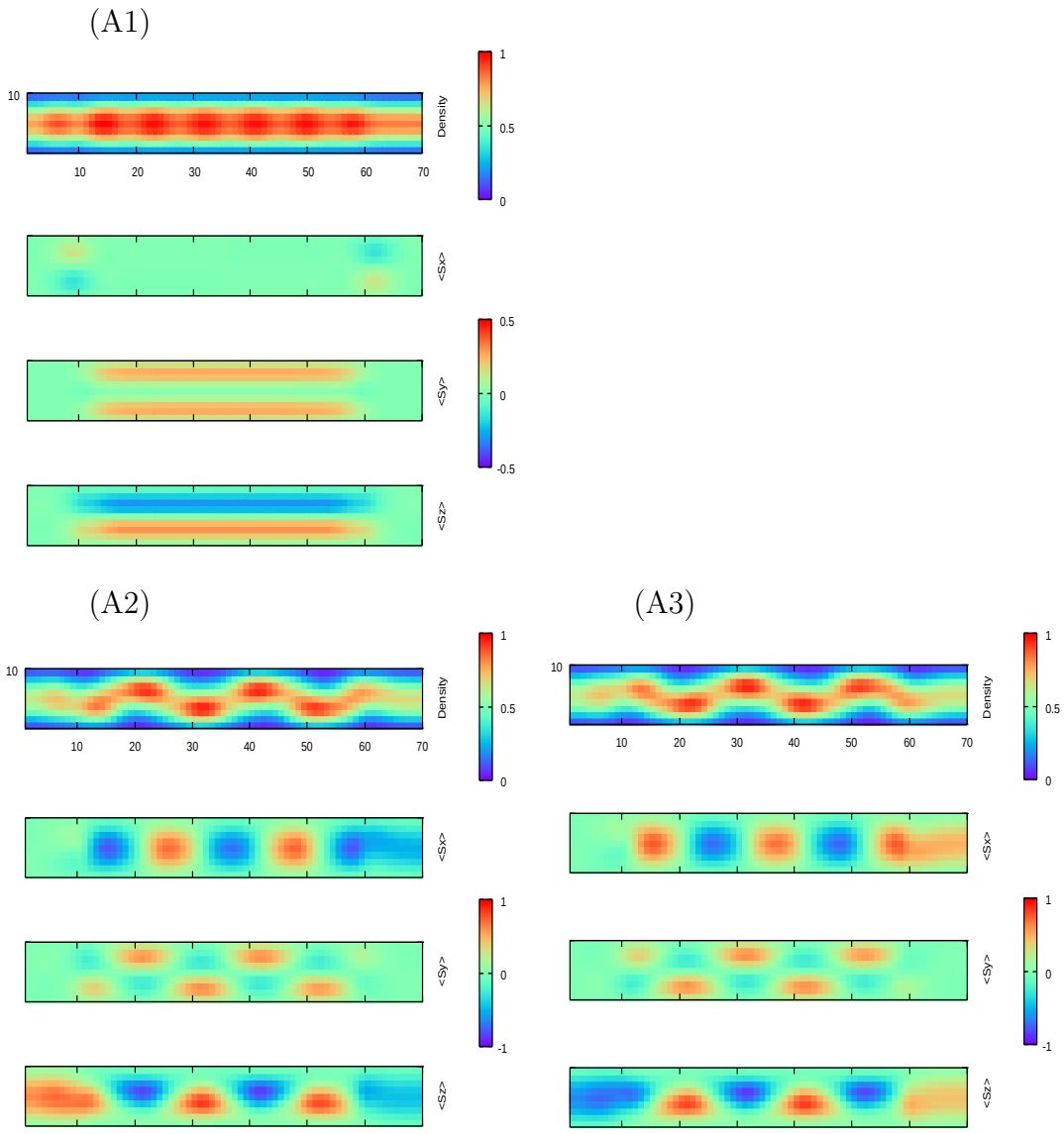

Figure 5.4: (A1) Charge and spin distribution of a current in the presence of RSO. The strength of RSO is set to be $\theta = 0.06\pi$. (A2) Up-spin component. (A3) Down-spin component.

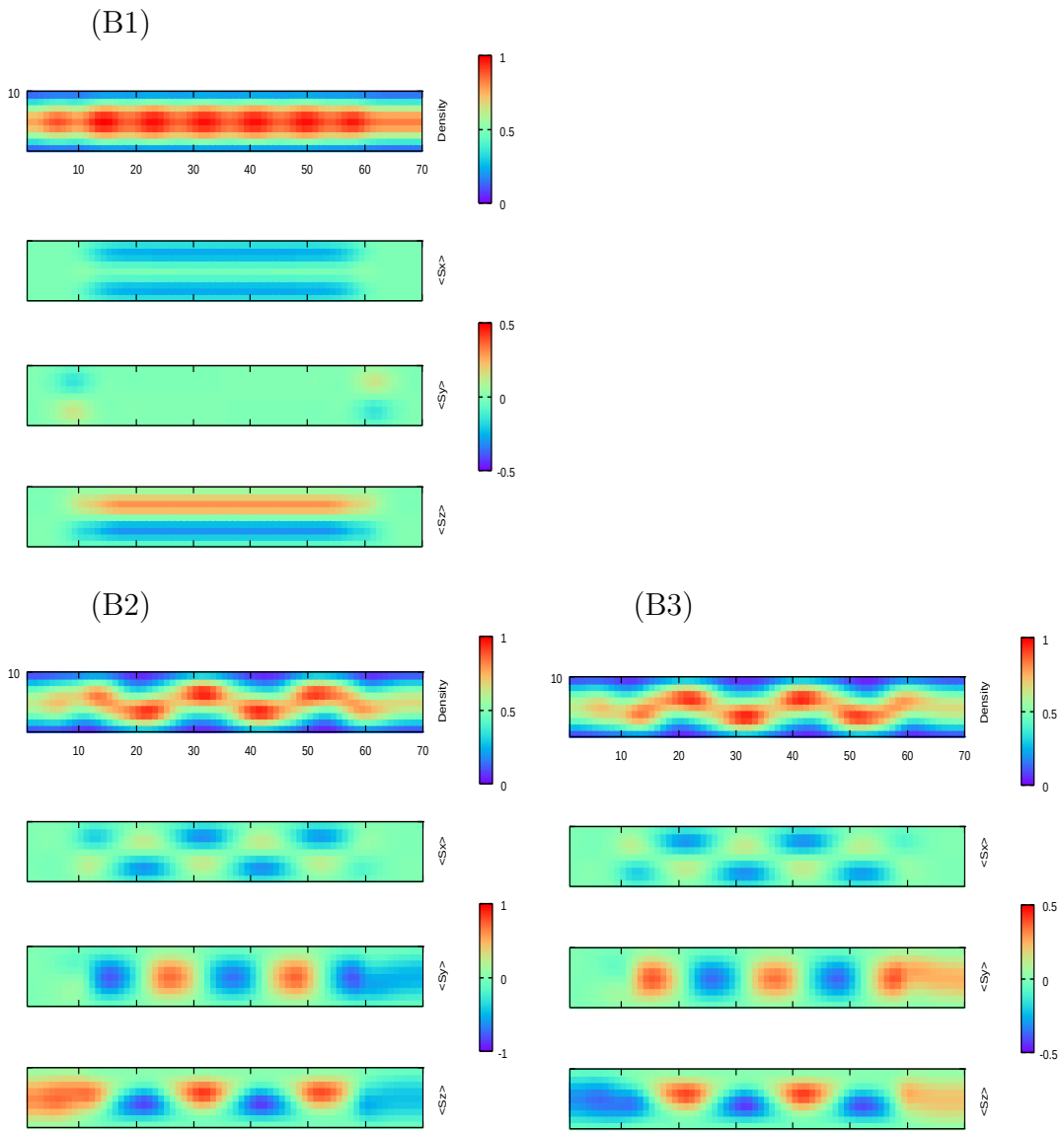

Figure 5.5: (B1) Charge and spin distribution of a current in the presence of DSO. The strength of DSO is set to be $\phi = 0.06\pi$. (B2) Up-spin component. (B3) Down-spin component.

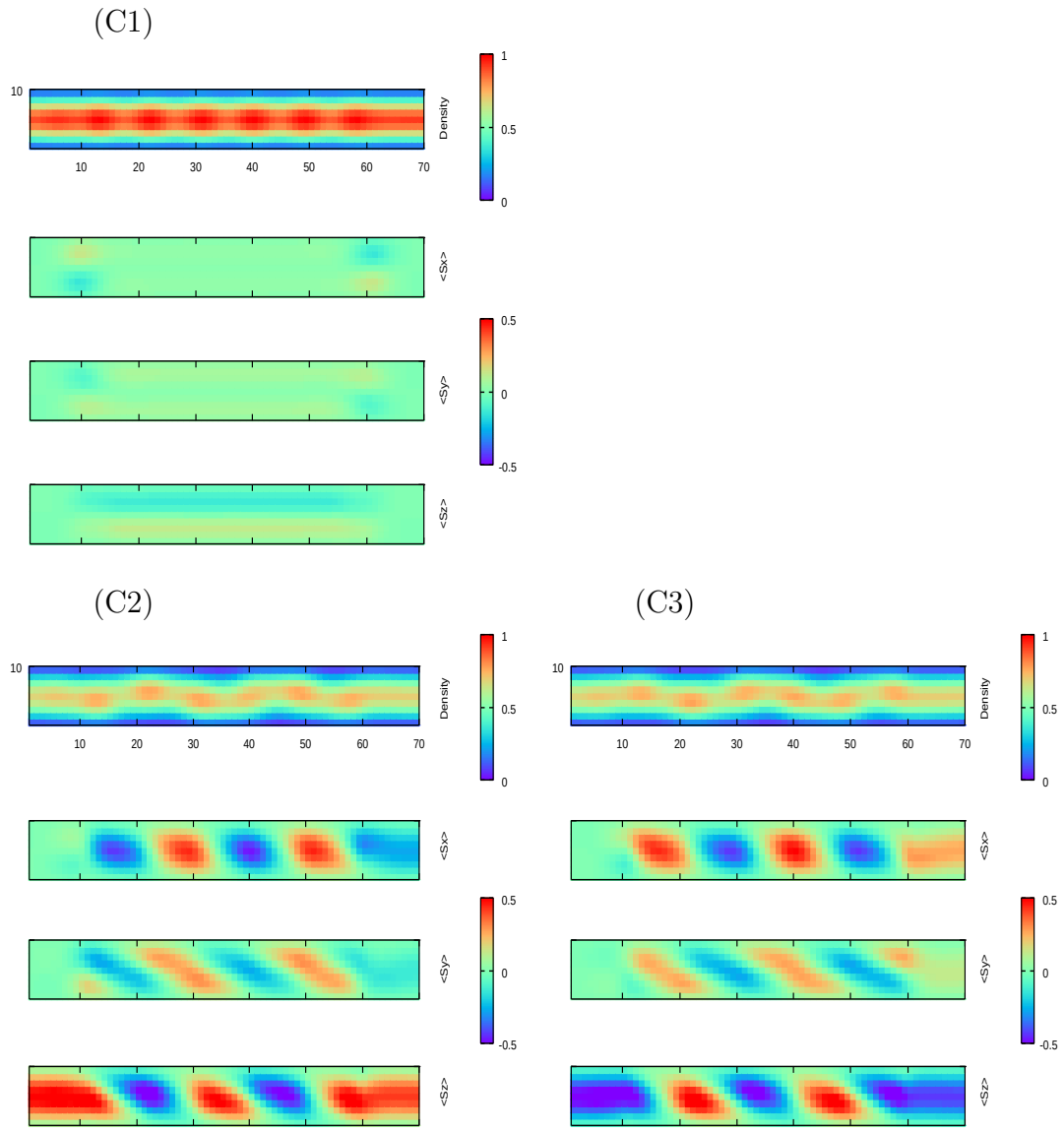

Figure 5.6: (C1) Charge and spin distribution of a current in the presence of RSO and DSO. The strength of RSO and DSO are set to be $\theta = 0.04\pi$ and $\phi = 0.02\pi$, respectively. (C2) Up-spin component. (C3) Down-spin component.

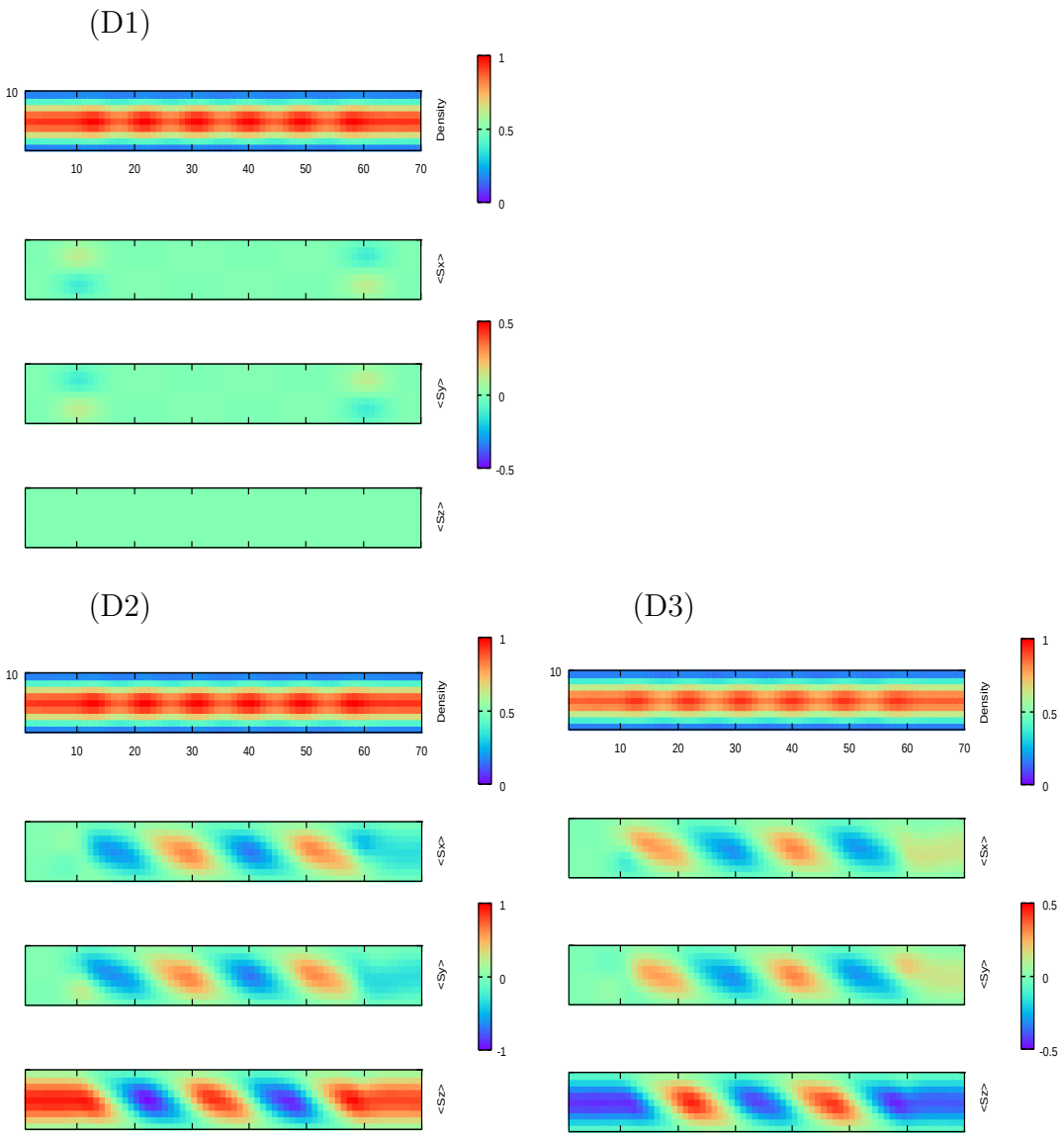

Figure 5.7: (D1) Charge and spin distribution of a current in the presence of RSO and DSO. The strength of RSO and DSO are set to be $\theta = \phi = 0.03\pi$ (D2) Up-spin component. (D3) Down-spin component.

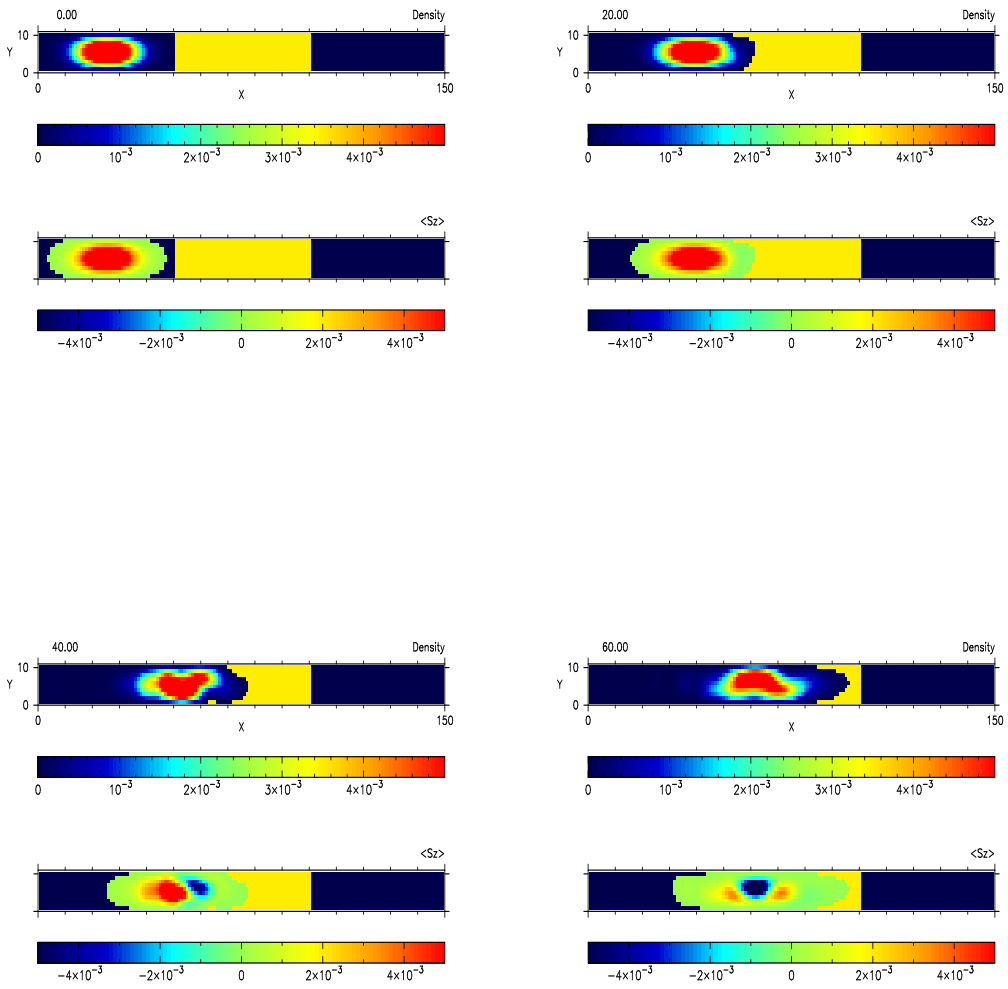

Figure 5.8: Time evolution of the wave packet. Yellow region represents the sample region with Rashba spin-orbit coupling. The time of each snapshot is $t = 0, 20, 40, \cdots$ in units of $\hbar V_0^{-1}$.

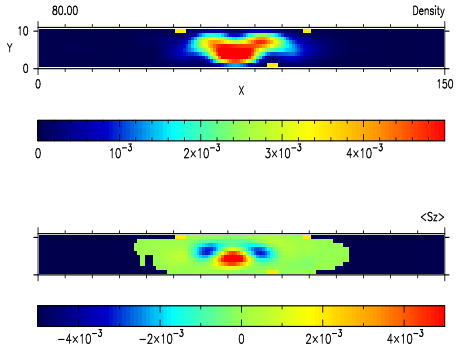
80.00
Density
Y
10
0
0
X
150
0
10^{-3}
2×10^{-3}
3×10^{-3}
4×10^{-3}
<Sz>
-4×10^{-3}
-2×10^{-3}
0
2×10^{-3}
4×10^{-3}

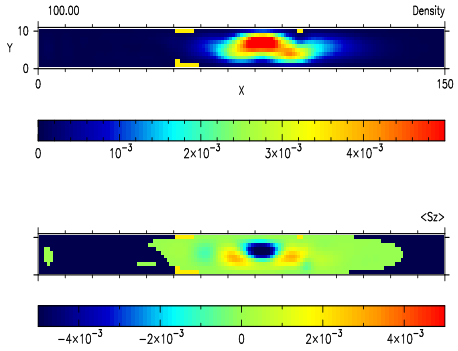
100.00
Density
Y
10
0
0
X
150
0
10^{-3}
2×10^{-3}
3×10^{-3}
4×10^{-3}
<Sz>
-4×10^{-3}
-2×10^{-3}
0
2×10^{-3}
4×10^{-3}

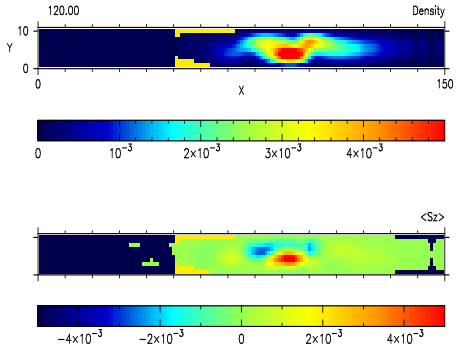
120.00
Density
Y
10
0
0
X
150
0
10^{-3}
2×10^{-3}
3×10^{-3}
4×10^{-3}
<Sz>
-4×10^{-3}
-2×10^{-3}
0
2×10^{-3}
4×10^{-3}

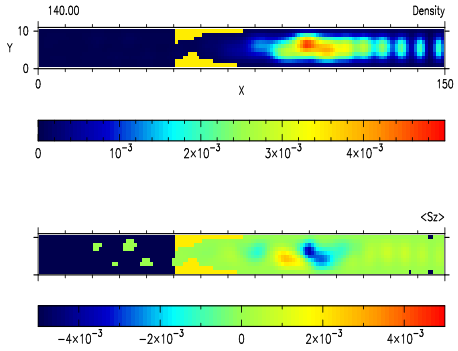
140.00
Density
Y
10
0
0
X
150
0
10^{-3}
2×10^{-3}
3×10^{-3}
4×10^{-3}
<Sz>
-4×10^{-3}
-2×10^{-3}
0
2×10^{-3}
4×10^{-3}

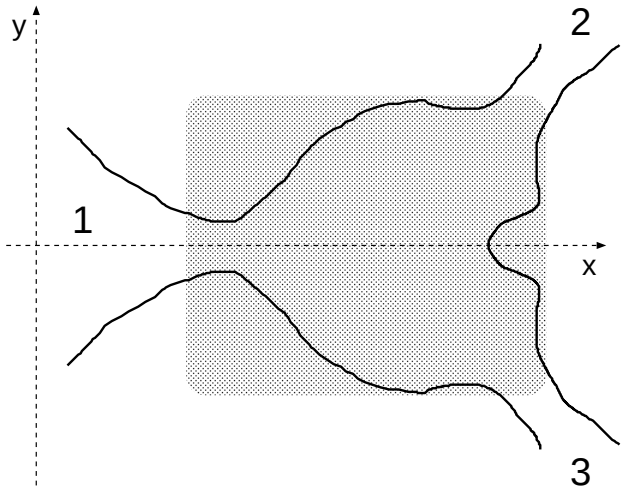

Figure 5.9: Schematic of a symmetric multi-terminal system. The shaded area represents the sample region with spin-orbit coupling.

Chapter 6

T-shape conductor

In this chapter, we have numerically investigated the spin-dependent electronic transport through the T-shape conductor as shown in Fig. 6.1. The sample region contains RSO and DSO and attached to three reservoirs via ideal probes. The Hamiltonian is given by Eq. (5.1). We have considered four different combinations of RSO and DSO as shown in Table 5.1. The system size is set to be $N_w = 10a$ and $N_l = 20a$ except Sec. 6.7. The spin-dependent transport in this system has been originally investigated by Kiselev and Kim [28]. Our results are consistent with their weak spin-orbit coupling results, while new properties have been observed for strong spin-orbit coupling [29].

6.1 Conductance and spin polarization

In this section, we show the energy dependence of the conductance and corresponding spin polarizations.

The conductance is defined by

$$G^{IJ} = G_0 \mathrm{Tr}\, t_{IJ}^{\dagger} t_{IJ} \tag{6.1}$$

where $G_0 \equiv e^2/h$ is the quantum conducntace and t_{IJ} denotes the transmission matrix from the reservoir J to I. Transmission matrix t_{IJ} can be calculated by the recursive Green function method. The corresponding spin polarizations are defined by

$$P_i^{IJ} = \frac{\mathrm{Tr}\, t_{IJ}^{\dagger} \sigma_i t_{IJ}}{\mathrm{Tr}\, t_{IJ}^{\dagger} t_{IJ}} \tag{6.2}$$

where $\sigma_i \, (i = x, y, z)$ represents the Pauli matrices.

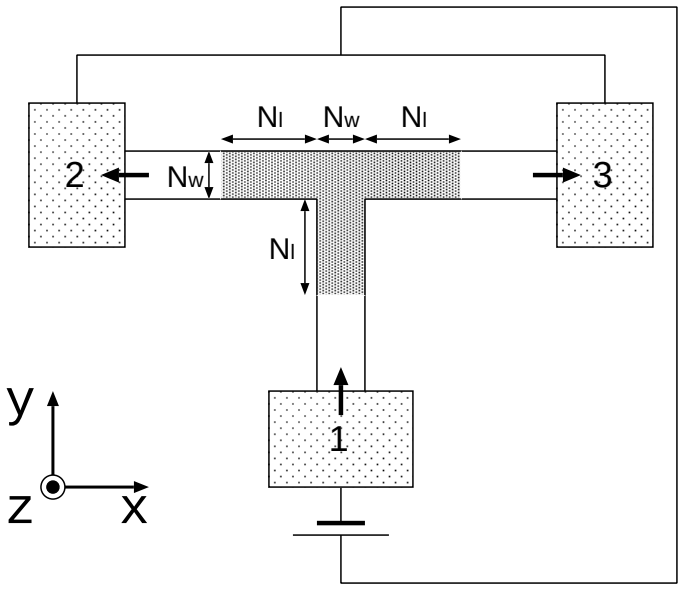

Figure 6.1: Schematic of the T-shape conductor. Shaded area represents the sample region with Rashba and Dresselhaus spin-orbit couplings.

In the following simulation, we focus on the ballistic transport ($W = 0$ in Eq. (5.1)) from the bottom reservoir ($J = 1$) to the left reservoir ($I = 2$) and right reservoir ($I = 3$).

6.1.1 Magnitude of spin polarization

Firstly, we focus on the magnitude of spin polarization,

$$|P| = \sqrt{P_x^2 + P_y^2 + P_z^2}. \tag{6.3}$$

Figure 6.2 shows the energy dependence of the conductance and corresponding spin polarization in the presence of RSO and DSO. It is shown that nearly 100% spin polarization can be obtained for the energy range of the single-channle transport in the presence of RSO (A). This result attributes to a strong spin-orbit coupling and differs from the result obtained in the precedent work in the weak coupling region [28]. In Sec. 6.4, we have compared the result obtained for strong RSO with that for weak RSO. We have also discussed the condition of this 100% spin polarization in Sec. 6.5.

The same result can be obtained for DSO (B). In the presence of both RSO and DSO (C), the spin-dependent transport becomes anisotropic. This results in

the different value of the spin polarization at the left and right probes. The spin polarization is strongly reduced when the strength of RSO is equal to that of DSO (D). We note that high polarization seems to be obtained at $E = -3.7V_0$, but corresponding conductance is quite small.

6.1.2 Direction of spin polarization

Secondly, we focus on the spin polarizations in the x-, y-, and z-directions. Figure 6.3 shows the energy dependence of each components of the spin polarization at the left and the right probes in the presence of RSO and DSO. In the presence of only RSO (A), the y- and z-components are antisymmetric while the x-component is symmetric between the left and right probes. Similar result with x and y spin directions interchanged are obtained in the presence of only DSO (B). This is due to the symmetry of the system (Sec. 5.4). In the presence of both RSO and DSO (C), the components of the spin polarization at the left and right probes are independent each other. The x- and y-components are antisymmetric each other in the same probe while the z-component is equal to zero for the same strength of RSO and DSO (D).

6.2 Charge and spin distribution of current

In this section, we show the charge and spin distribution of a current. We focus on a ballistic transport ($W = 0$ in Eq. (5.1)). The Fermi energy is set to be $E = -3.8V_0$ where only one channel is opened.

A: RSO

Figure 6.4 shows the charge and spin distribution of a current in the presence of RSO. The strength of RSO is set to be $\theta = 0.06\pi$. It is shown that the charge distribution is symmetric while the spin distribution is antisymmetric (A1). This can be explained by the symmetry of the system in Sec. 5.4.

It is well known that the direction of spin are not randomly distributed but quantized in a certain direction. This property was originally shown by the Stern-Gerlach experiment [11]. In the previous chapter, the direction of the spin quantization axis is set to be the z-direction, but one can arbitrarily choose this direction if the up and down spins are degenerated. (A2) and (A3) show the charge and spin distributions of a current initially having the up and down spin components in the particular spin quantization axis. The up and down spins are represented

by the spins parallel to the z-axis as

$$|\uparrow\rangle_{new} = \cos\frac{\theta'}{2}|\uparrow\rangle + \sin\frac{\theta'}{2}\,e^{i\phi'}|\downarrow\rangle \quad (6.4)$$

$$|\downarrow\rangle_{new} = -\sin\frac{\theta'}{2}|\uparrow\rangle + \cos\frac{\theta'}{2}\,e^{i\phi'}|\downarrow\rangle \quad (6.5)$$

with $\theta' = 0.6978\pi$ and $\phi' = -\pi/2$.

It is clearly shown that a current with up and down spins are separated at the junction of the T-shape conductor. This is due to the spin-dependent effective magnetic field (Sec. 3.6). We also give the detailed analysis in Sec. 6.5.

B: DSO

Figure 6.5 shows the charge and spin distribution of a current in the presence of DSO. The strength of DSO is set to be $\phi = 0.06\pi$. The charge distribution is the same as that of RSO while the spin distirbution is opposite since the direction of a spin-dependent effective magnetic field is antiparallel between RSO and DSO (Eq. (3.36)). This property can be clearly observed in the charge and spin distributions of a current initially having the up and down spin components ((B2) and (B3)). Here the up and down spins are represented by the spins parallel to the z-axis as

$$|\uparrow\rangle_{new} = \cos\frac{\theta'}{2}|\uparrow\rangle + \sin\frac{\theta'}{2}\,e^{i\phi'}|\downarrow\rangle \quad (6.6)$$

$$|\downarrow\rangle_{new} = -\sin\frac{\theta'}{2}|\uparrow\rangle + \cos\frac{\theta'}{2}\,e^{i\phi'}|\downarrow\rangle \quad (6.7)$$

where $\theta' = 0.3022\pi$ and $\phi' = 0$.

C: RSO + DSO

Figure 6.6 shows the charge and spin distribution of a current in the presence of both RSO and DSO. The strength of RSO and DSO are set to be $\theta = 0.04\pi$ and $\phi = 0.02\pi$, respectively. The reflection at the junction are enhanced since the strength of effective magnetic field (Eq. (3.36)) are weaken due to the coexistance of RSO and DSO. (C2) and (C3) show the charge and spin distribution of the current initially having the up and down spin components parallel to the z-axis, respectively.

D: RSO=DSO

Figure 6.7 shows the charge and spin distribution of a current for the same strength of RSO and DSO ($\theta = \phi = 0.03\pi$). The reflection at the junction are further

enhanced since the strength of effective magnetic field (Eq. 3.36) is equal to zero (D1). It is also shown that there is no spin polarization in the z-direction. (D2) and (D3) show the charge and spin distribution for the current initially having the up and down spin components parallel to the z-axis, respectively. In this case, the charge distributions of up- and down-spin components are identical.

6.3 Dynamics of wave packet

In this section, we show the dynamics of the wave packet. We have considered the isolated system which consists of the ideal probe regions and the sample region with RSO (Fig. 6.8). The size of the probe and sample regions are set to be $(N_l^{\rm probe} \times N_w^{\rm probe}) = (20 \times 10)$ and $(N_x^{\rm sample} \times N_y^{\rm sample}) = (10 \times 10)$, respectively. The size of the ideal probe is $(N_l^{\rm ideal} \times N_w^{\rm ideal}) = (40 \times 10)$. The strength of RSO is set to be $\theta = 0.06\pi$.

The initial shape of the wave packet is same as that given in Sec. 5.3. The initial spin state is given by

$$|\chi\rangle = \cos\frac{\theta'}{2}|\uparrow\rangle + \sin\frac{\theta'}{2}\mathrm{e}^{i\phi'}|\downarrow\rangle \tag{6.8}$$

where $\theta' = 0.9678\pi$ and $\phi' = -\pi/2$. One can see the more detailed dynamics of the wave packet as animation in the attached CD.

6.4 Dependence on spin-orbit coupling

Figure 6.9 shows the dependence of the conductance and the spin polarization on the Fermi energy E for weak and strong spin-orbit couplings. We consider the energy region for single-channel transport. For weaker spin-orbit coupling ($\theta = 0.02\pi$), high spin polarization is obtained for energies just before the second channel opens ($E \simeq -3.68V_0$). The corresponding conductance is small as compared to G_0. This result is consistent with that of the preceding investigation [28]. Almost perfect polarization is obtained together with a conductance close to G_0 for stronger spin-orbit coupling ($\theta = 0.06\pi$). Here, the polarization is almost insensitive to the energy except near the band edge.

Figure 6.10 shows the dependence of the conductance and the spin polarization on the strength of RSO at energy $E = -3.8V_0$. With the increase of the strength of RSO, P_y also increases monotonically while P_x and P_z oscillate. We also note that the conductance increases together with the amplitude of the polarization.

6.5 Condition for 100% spin polarization

What are the conditions for achieving almost perfect polarization? We define the π-phase spin precession length $L_{\rm so}(|P|, N_w) = \pi a/2\theta(|P|, N_w)$ where $\theta(|P|, N_w)$ is the strength of RSO giving rise to the polarization $|P|$ for the width N_w. From the plot $L_{\rm so}(|P|, N_w)$ as a function of the width of the system N_w (Fig. 6.11), one concludes that $L_{\rm so}(|P|, N_w)$ is almost linear in N_w and high polarization, $|P| > 0.99$, is achieved for $L_{\rm so}(|P|, N_w) < N_w$.

Let us use Eq.(3.42) to estimate the strength of effective magnetic field,

$$\bar{B}(\theta) = \frac{4\hbar\theta^2}{\pi e a^2} = \frac{\hbar\pi}{eL_{\rm so}^2} \tag{6.9}$$

where we have averaged σ_z to be $2/\pi$, since the variation of the expectation value of σ_z is described by the cosine function. Since the kinetic energy is comparable to the confinement energy in single-channel transport, the velocity of an injected electron can be assumed to be

$$v \simeq \frac{\hbar\pi}{m^* N_w}. \tag{6.10}$$

Then the corresponding cyclotron diameter is given by

$$2l_{\bar{B}}(\theta) = \frac{2m^* v}{e\bar{B}(\theta)} = \frac{2L_{\rm so}^2}{N_w}. \tag{6.11}$$

The cyclotron diameter becomes shorter than the wire width ($2l_{\bar{B}}(\theta) < N_w$) if the spin precession length becomes shorter than the wire width ($L_{\rm so} < N_w/\sqrt{2}$). As a result, electrons with opposite z–component spin are almost completely separated at the junction and nearly perfect spin polarization is obtained (Fig.6.12). This situation is similar to the mesoscopic cross junction in magnetic fields [30].

6.6 Influence of disorder

We now consider briefly the effect of disorder on the spin polarization (Fig. 6.13). An ensemble average is performed over 10^4 samples. The suppression of the polarization by disorder becomes more prominent as the spin-orbit coupling becomes stronger. The mean free path of a 2DES in the tight-binding model is described by [25]

$$L_m = 48 a V_0^{3/2} \frac{\sqrt{E + 4V_0}}{W^2}. \tag{6.12}$$

One can use this estimate to distinguish the ballistic regime from the diffusive one. For the present system, we obtain $W \simeq 1.53V_0$ for $L_m = 50a$ (indicated by an arrow in Fig. 6.13). As seen in the figure, the sample size must be smaller than the mean free path in order to obtain high spin polarization.

6.7 Experimental realization

In order to obtain information whether or not the predicted effects are observable in experiment, let us consider the parameters required for one of the favorable materials, InAs, with an effective mass $m^* = 0.039m$ (m is the free electron mass) and Rashba coupling $\alpha = 238$ meVÅ[31]. Let us assume that the width of the conduction band is $\Delta = 1\,\mathrm{eV}$. This gives for $V_0 = \Delta/2Z = 125\,\mathrm{meV}$ ($Z = 4$ for square lattice), and for the tight-binding lattice parameter $a = \hbar/(2m^*V_0)^{1/2} \simeq 2.8\,\mathrm{nm}$. Using the above numerical value of α one obtains $\theta = \alpha/2V_0a \simeq 0.01\pi$. This would reduce the polarization to about 10%, still a reasonable value for being observable in experiment. The crucial point, however, is the condition that the transport has to be in the single-channel regime. The wire width should be about 20 nm for single-channel transport when Fermi energy is of the order of 10 meV.

For this reason, we have investigated the transport in the system whose sizes are $N_w = 50a$ (140 nm) and $N_l = 50a$ where many channels exist. Figure 6.14 shows the dependence of the conductance and the spin polarization on the Fermi energy E for $\theta = 0.01\pi$. We focus on the energy region $-3.9V_0 < E < -3.6V_0$. In this energy region where the number of channels increases to values ranging from 5 to 10, several channels contribute to transport. While the spin polarization is reduced by channel mixing, it still stays higher than 10%. This indicates that we can observe the spin polarization experimentally.

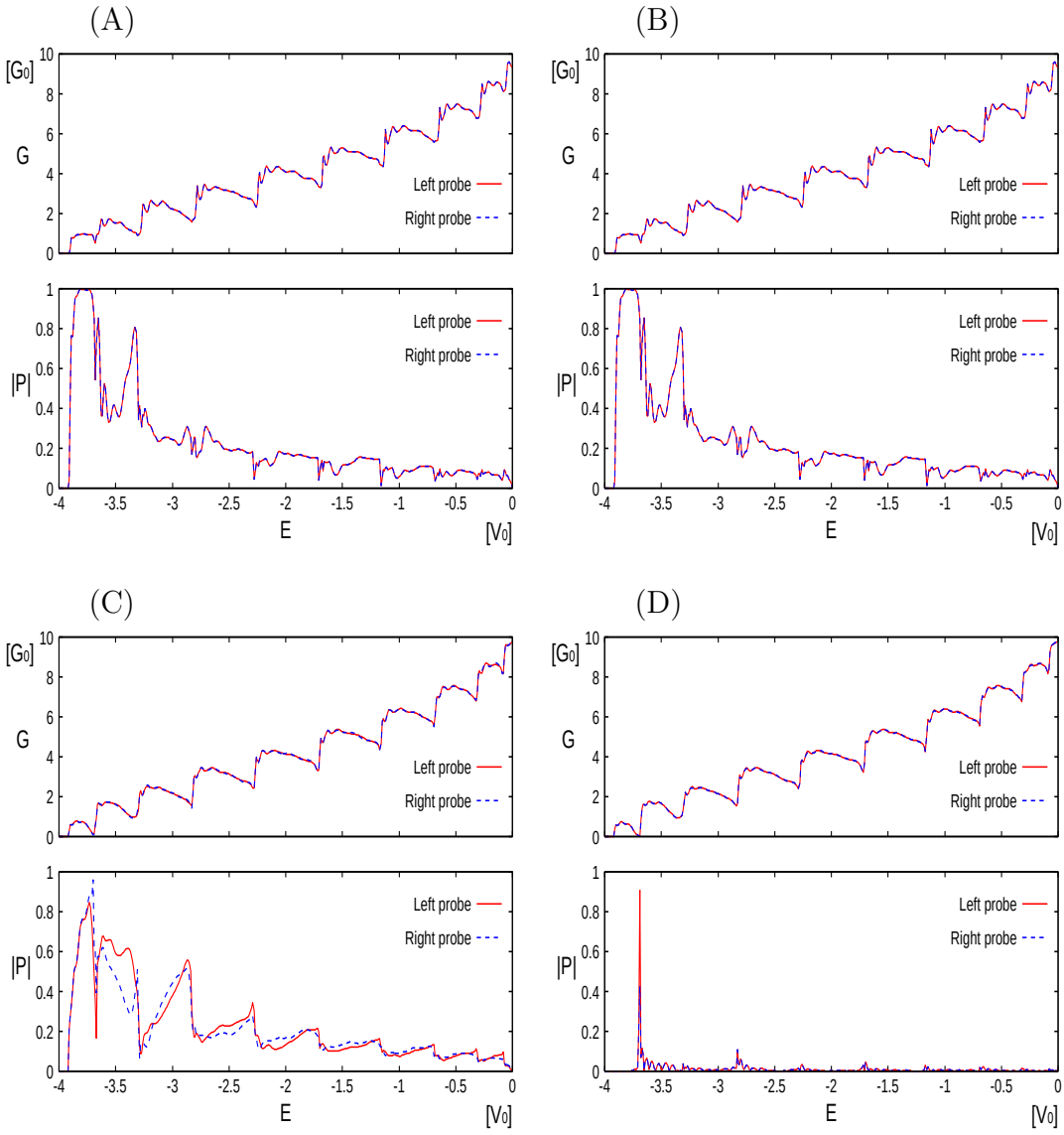

Figure 6.2: Energy dependence of the conductance (upper) and corresponding spin polarization (lower). The strengths of RSO (θ) and DSO (ϕ) are set to be as follows. (A) $\theta = 0.06\pi$. (B) $\phi = 0.06\pi$. (C) $\theta = 0.04\pi$ and $\phi = 0.02\pi$. (D) $\theta = \phi = 0.03\pi$.

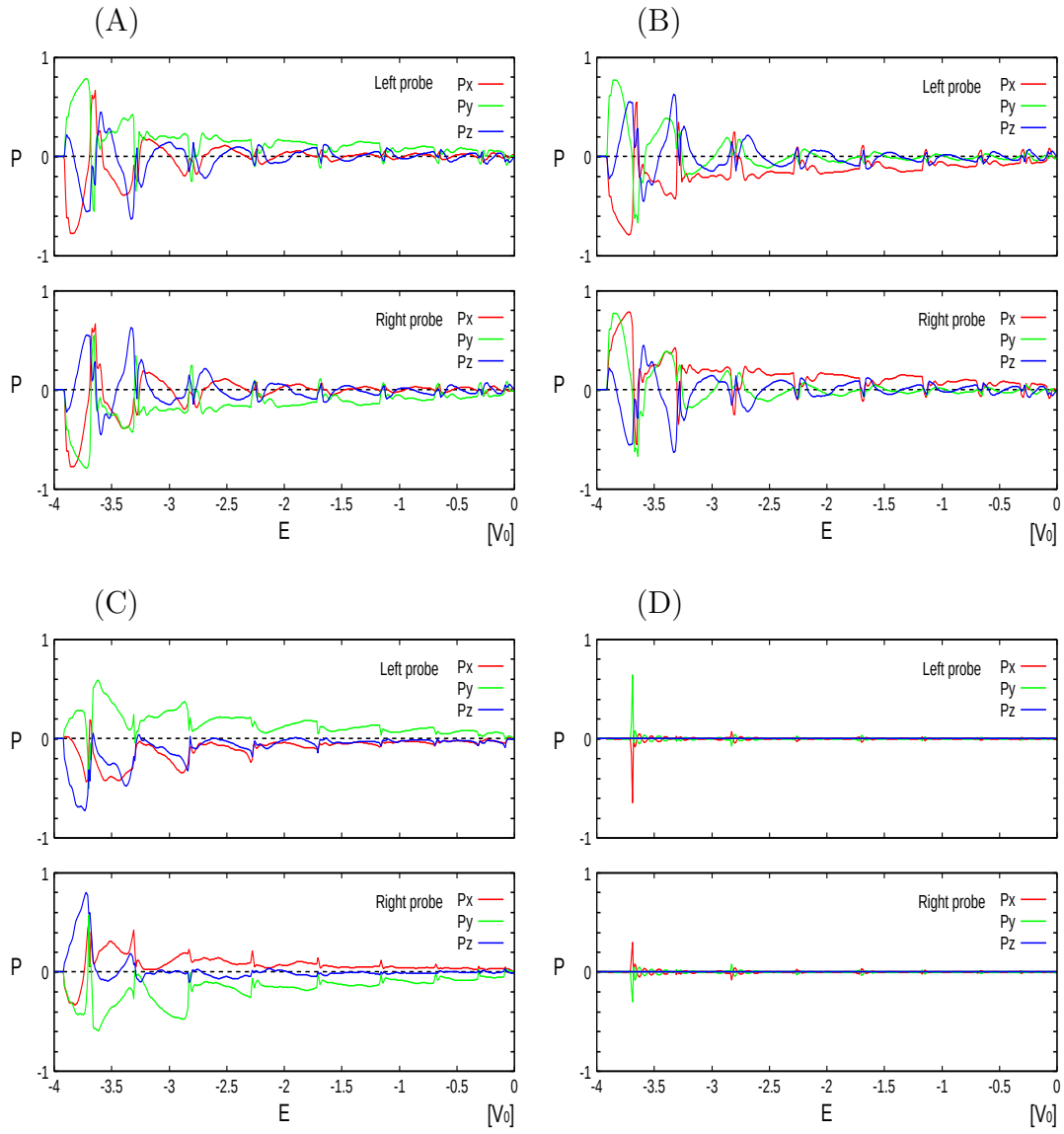

Figure 6.3: Components of spin polarization at the upper probe (upper) and the lower probe (lower). The strengths of RSO (θ) and DSO (ϕ) are set to be as follows. (A) $\theta = 0.06\pi$. (B) $\phi = 0.06\pi$. (C) $\theta = 0.04\pi$ and $\phi = 0.02\pi$. (D) $\theta = \phi = 0.03\pi$.

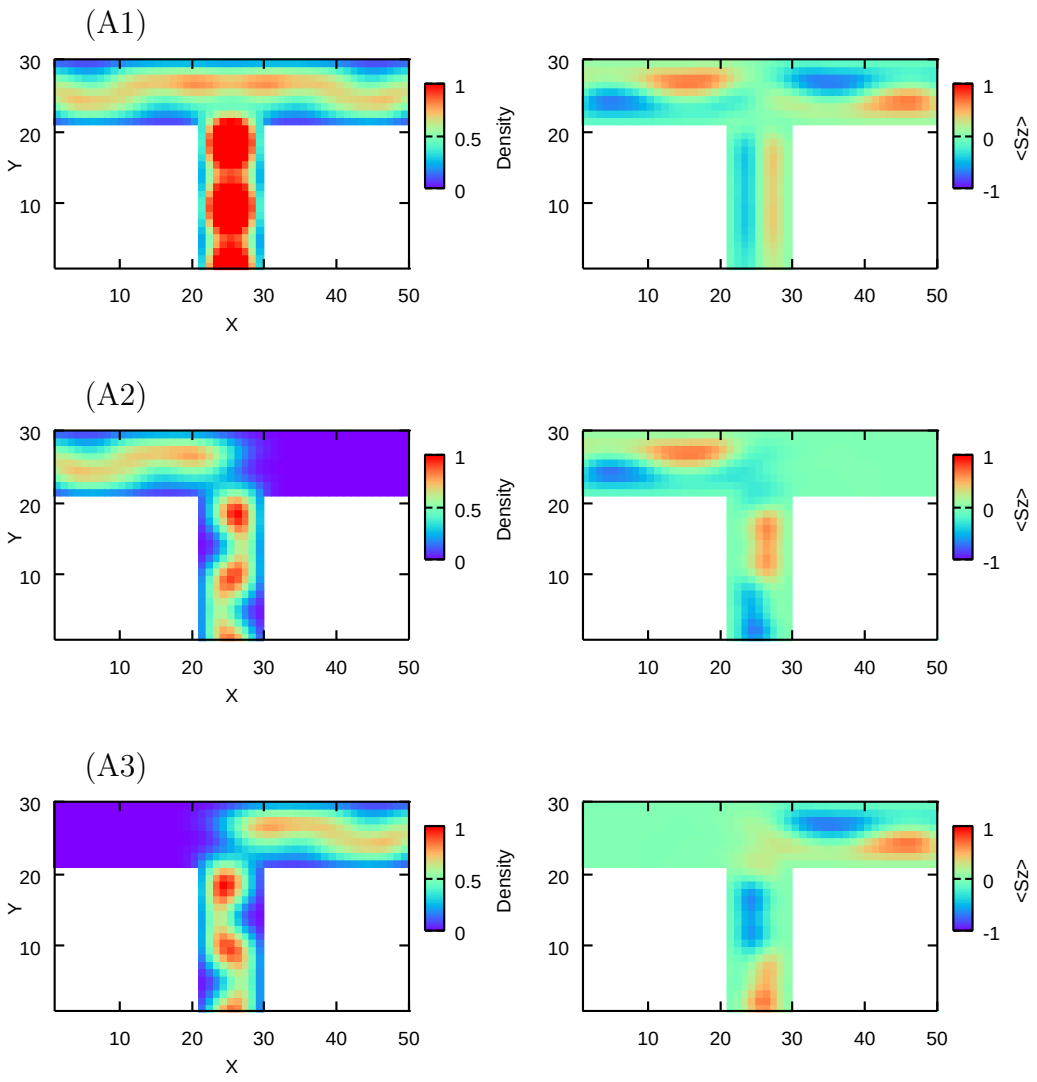

Figure 6.4: (A1) Charge and spin distribution of a current in the presence of RSO. The strength of RSO is set to be $\theta = 0.06\pi$. (A2) Left-going solution. (A3) Right-going solution.

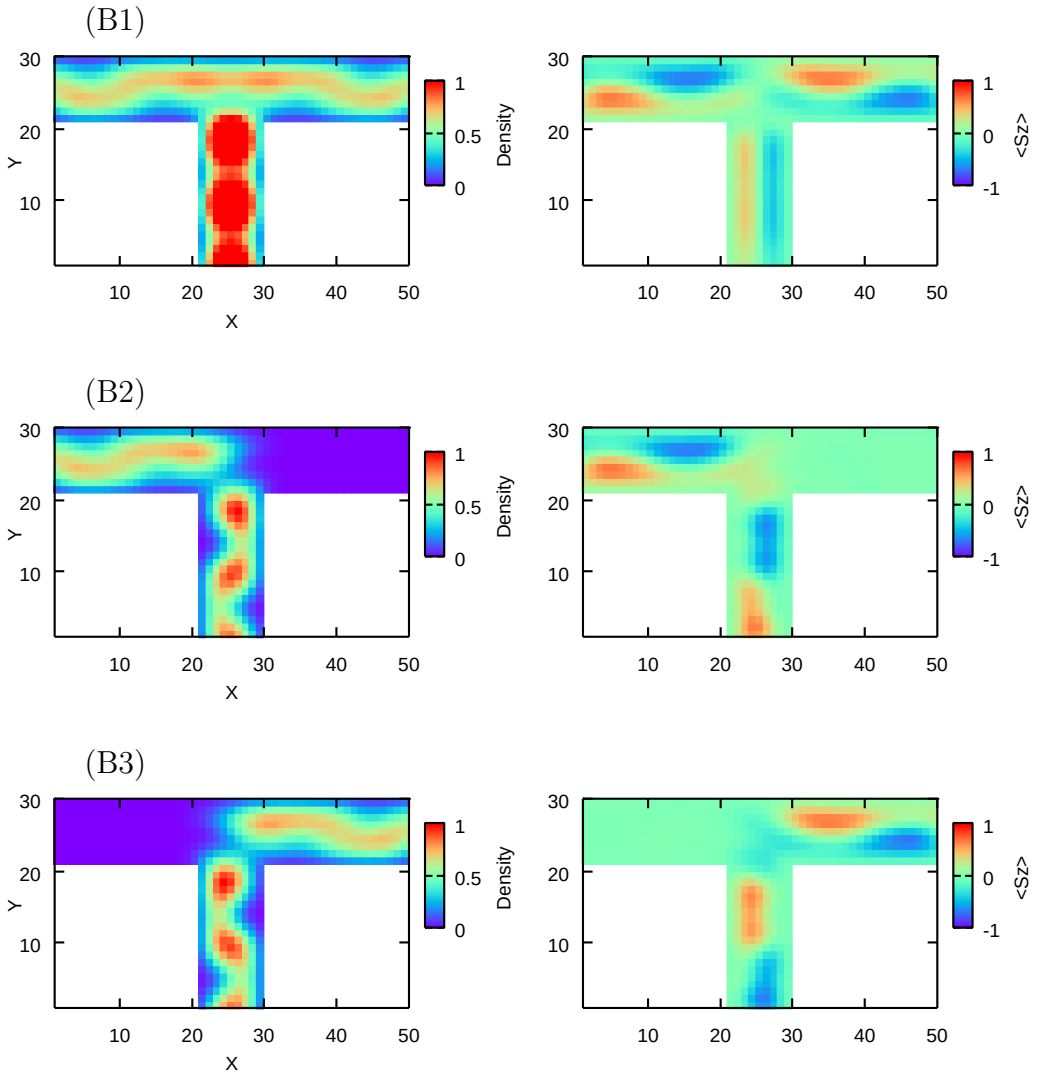

Figure 6.5: (B1) Charge and spin distribution of a current in the presence of DSO. The strength of DSO is set to be $\phi = 0.06\pi$. (B2) Left-going solution. (B3) Right-going solution.

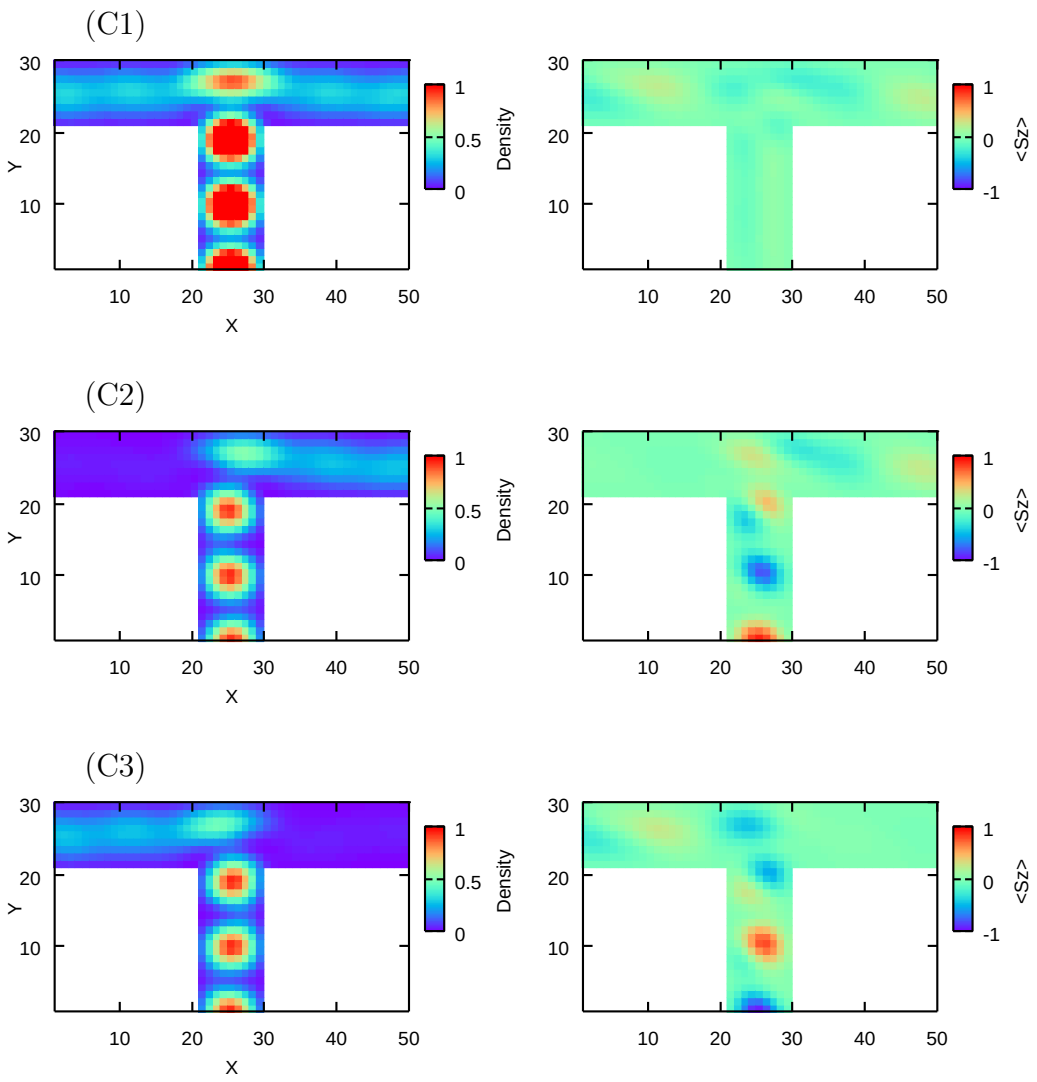

Figure 6.6: (C1) Charge and spin distribution of a current in the presence of RSO and DSO. The strengths of RSO and DSO are set to be $\theta = 0.04\pi$ and $\phi = 0.02\pi$, respectively. (C2) Up-spin component. (C3) Down-spin component.

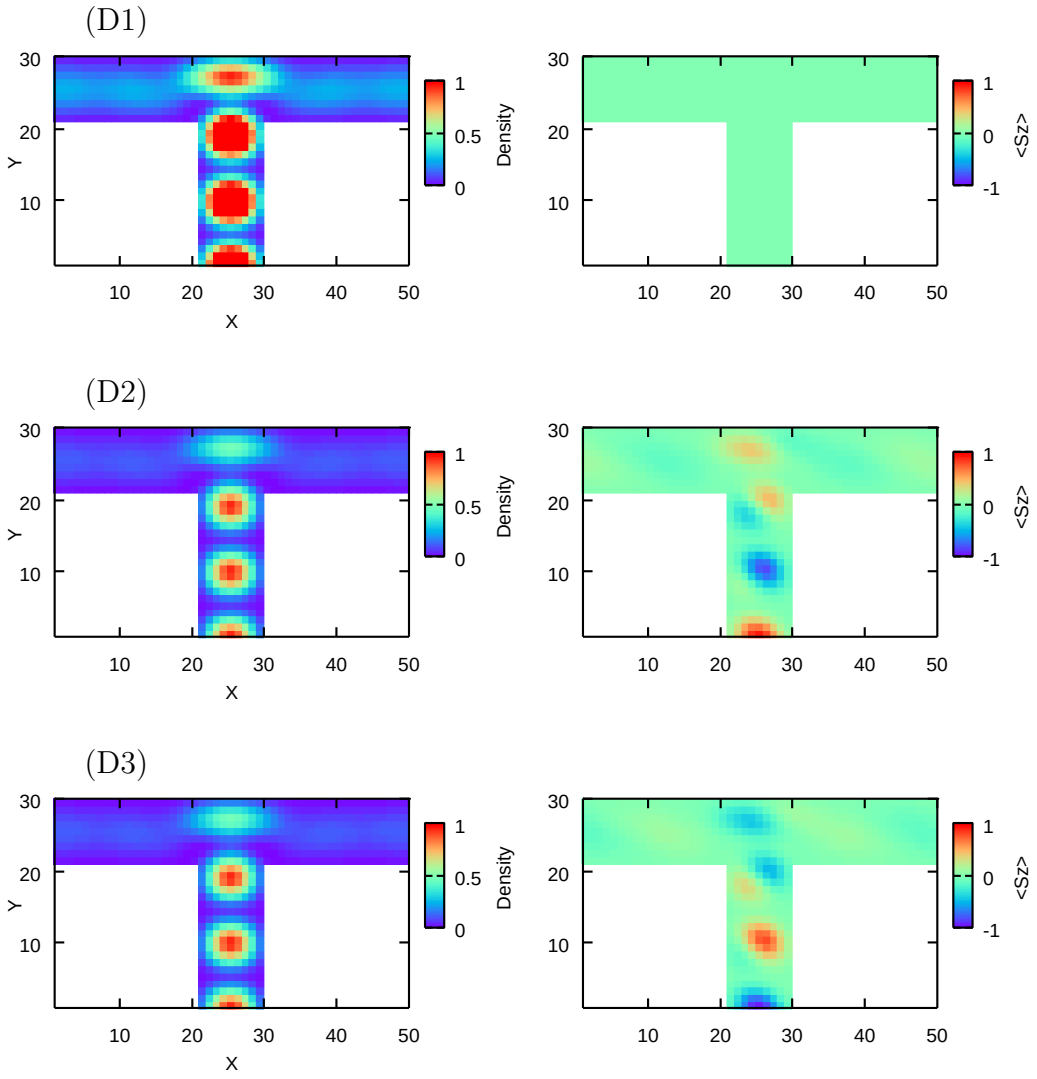

Figure 6.7: (D1) Charge and spin distribution of a current in the presence of RSO and DSO. The strengths of RSO and DSO are set to be $\theta = \phi = 0.03\pi$. (D2) Up-spin component. (D3) Down-spin component.

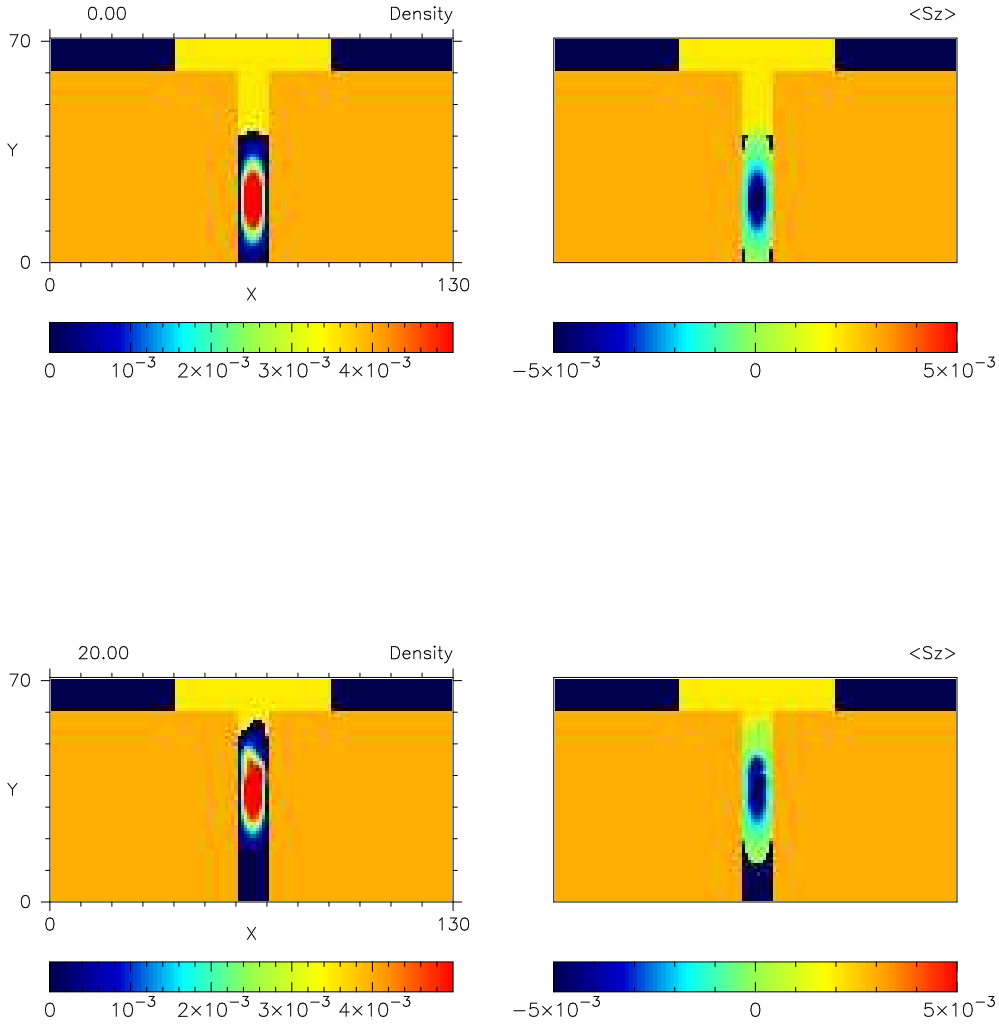

Figure 6.8: Time evolution of the wave packet. Yellow region represents the sample region with Rashba spin-orbit coupling. The time of each snapshot is $t = 0, 20, 40, \cdots$ in units of $\hbar V_0^{-1}$.

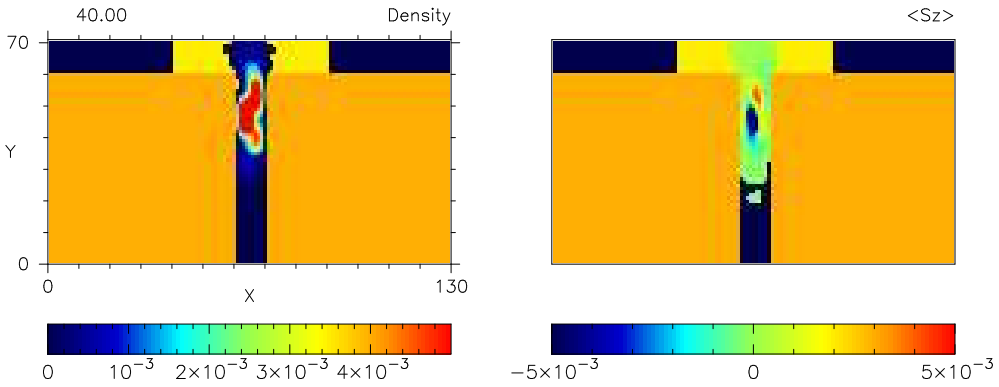
40.00
Density
70
Y
0
0
X
130
0
10^-3
2×10^-3
3×10^-3
4×10^-3
<Sz>
−5×10^-3
0
5×10^-3

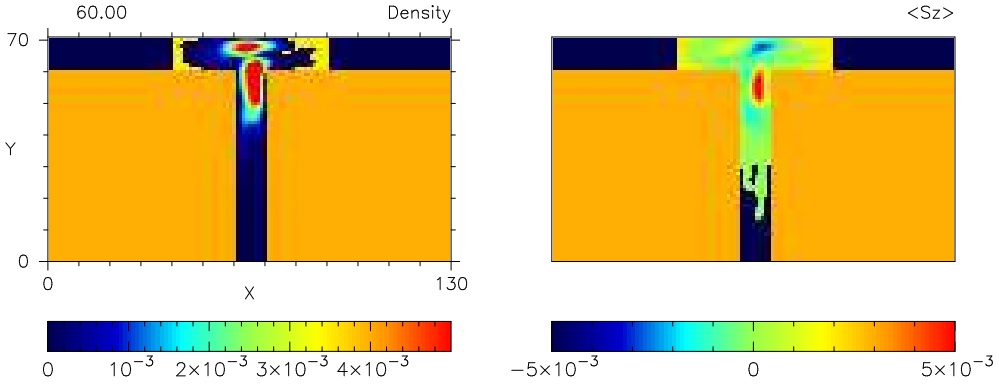
60.00
Density
70
Y
0
0
X
130
0
10^-3
2×10^-3
3×10^-3
4×10^-3
<Sz>
−5×10^-3
0
5×10^-3

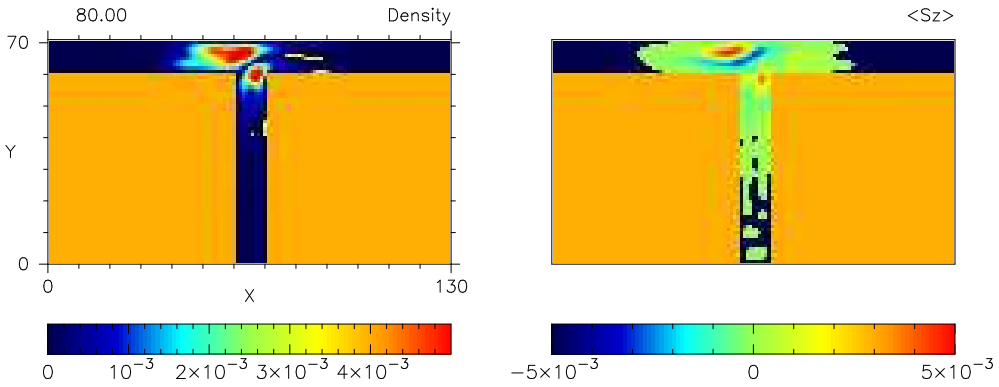
80.00
Density
70
Y
0
0
X
130
0
10^-3
2×10^-3
3×10^-3
4×10^-3
<Sz>
−5×10^-3
0
5×10^-3

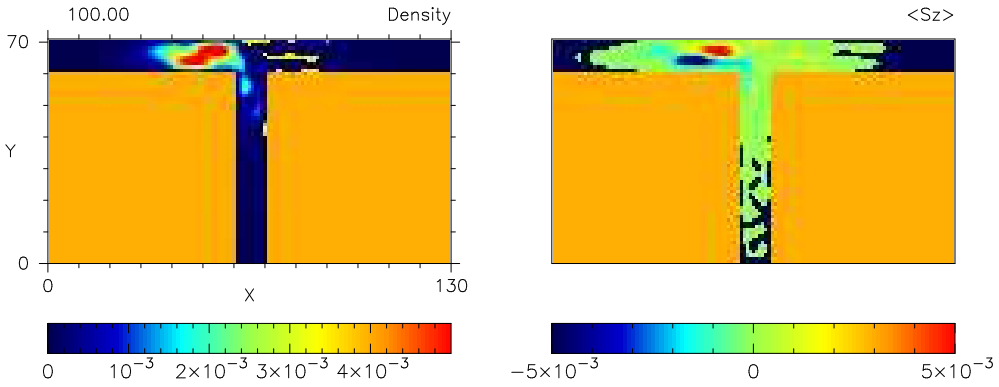
100.00
Density
70
Y
0
0
X
130
0
10^-3
2×10^-3
3×10^-3
4×10^-3
<Sz>
−5×10^-3
0
5×10^-3

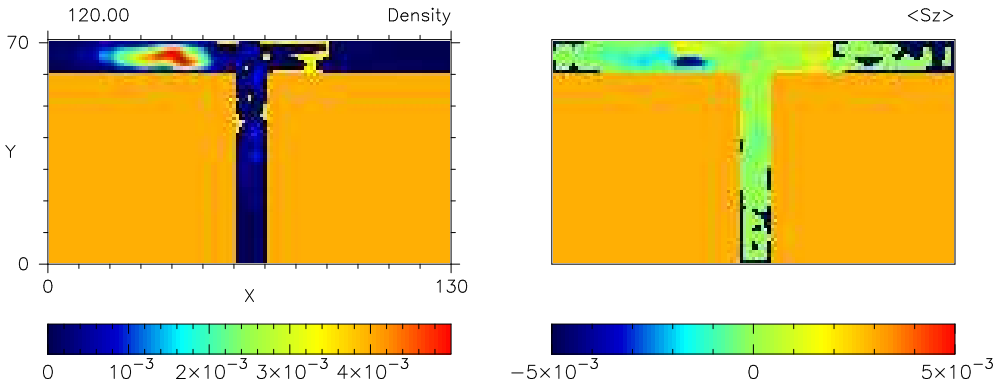
120.00
Density
70
Y
0
0
X
130
0
10^-3
2×10^-3
3×10^-3
4×10^-3
<Sz>
−5×10^-3
0
5×10^-3

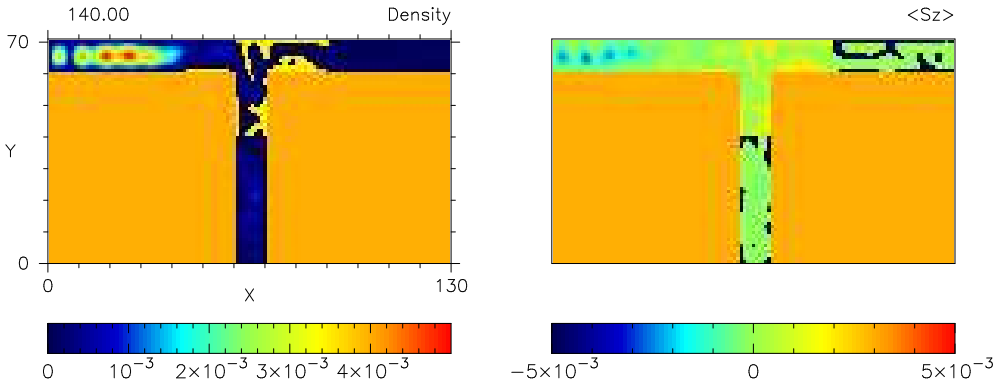
140.00
Density
70
Y
0
0
X
130
0
10^-3
2×10^-3
3×10^-3
4×10^-3
<Sz>
−5×10^-3
0
5×10^-3

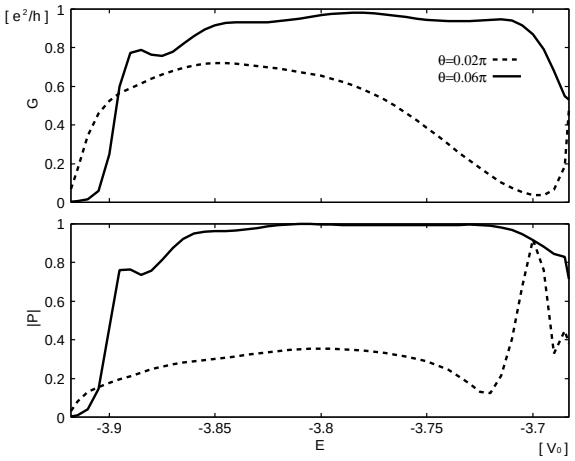

Figure 6.9: Conductance G and spin polarization $|P|$ as functions of the Fermi energy E in the region of single-channel transport in the presence of Rashba spin-orbit coupling. Almost 100% polarization is obtained together with $G \approx G_0$ for stronger spin-orbit coupling ($\theta = 0.06\pi$). For $\theta = 0.02\pi$ high polarization is obtained only at energies just before the second channel opens.

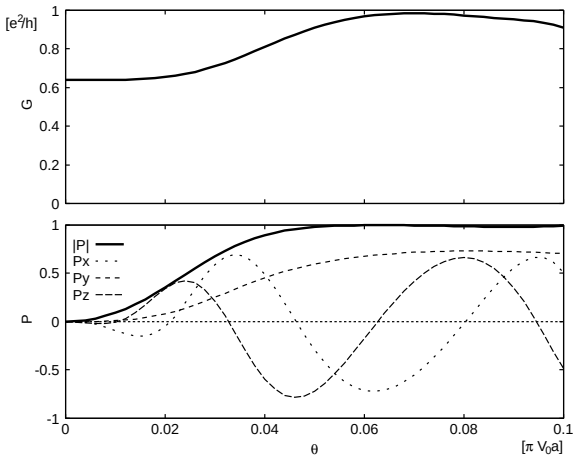

Figure 6.10: Conductance G and spin polarization P_k in the directions of $k = x, y, z$ as functions of the strength of Rashba spin-orbit coupling θ for $E = -3.8V_0$; P_y increases monotonically with increasing θ while P_x and P_z oscillate.

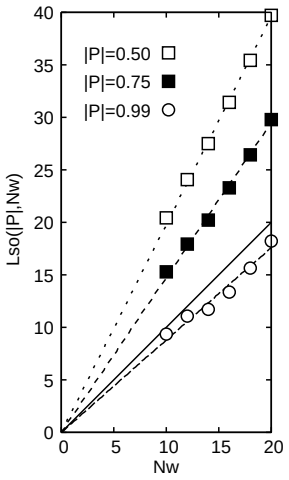

Figure 6.11: The spin precession lengths $L_{\rm so}$ for $|P| = 0.5, 0.75, 0.99$ as functions of the width of the wires N_w. Energy is set to be the middle of lowest and first excited subband, e.g., $E = -3.8V_0$ for $N_w = 10$. The polarization becomes almost perfect if the spin precession length becomes shorter than the wire width, $L_{\rm so}(|P|, N_w) = \pi a/2\theta(|P|, N_w) < N_w$. Solid line: $L_{\rm so}(|P|, N_w) = N_w$ corresponding to $|P| \simeq 0.97$.

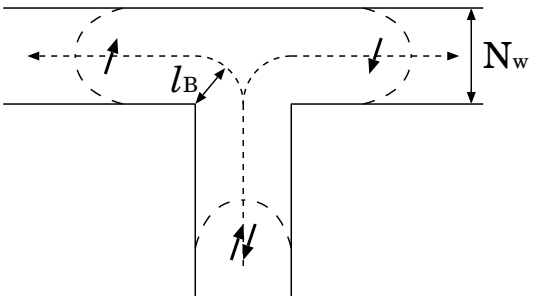

Figure 6.12: Schematic view of the electron trajectory. A pair of the electrons with anti-parallel spins are almost completely separated at the junction when the cyclotron diameter becomes shorter than the wire width ($2l_{\bar{B}}(\theta) < N_w$).

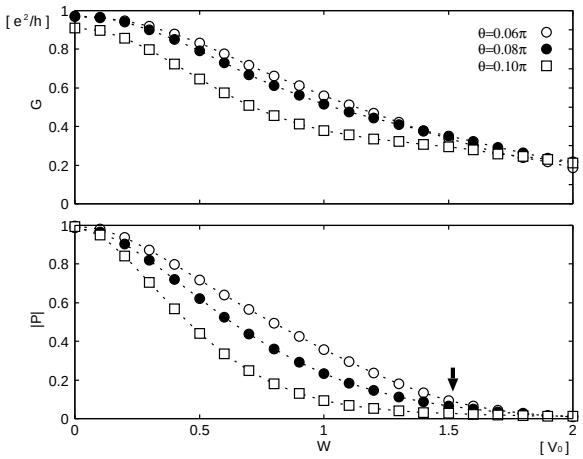

Figure 6.13: Conductance G and spin polarization $|P|$ as functions of the strength of disorder W for several spin-orbit couplings at $E = -3.8V_0$. Ensemble average has been taken over 10^4 samples. For stronger spin-orbit coupling, the polarization becomes more sensitive to disorder. Arrow: crossover between ballistic and diffusive regimes [cf.Eq.(6.12)].

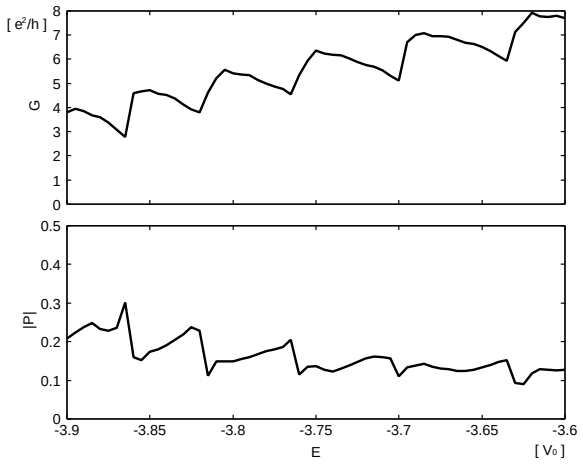

Figure 6.14: Conductance G and spin polarization $|P|$ as functions of the Fermi energy E in the region of multi-channel transport. The system size is set to be $N_w = 50a$ and $N_l = 50a$, and the strength of spin-orbit coupling $\theta = 0.01\pi$.

Chapter 7

Cavity attached to three probes

In the experiment, it is still hard to fabricate a narrow T-shape structure such that the transport is formed only by the lowest subband. In order to realize the single-channel transport, it is more realistic to fabricate a structure by a quantum dot attached to three probes via point contacts [32]. For this reason, we have investigated the transport through the cavity attached to three reservoirs via ideal probes as shown in Fig. 7.1 [33].

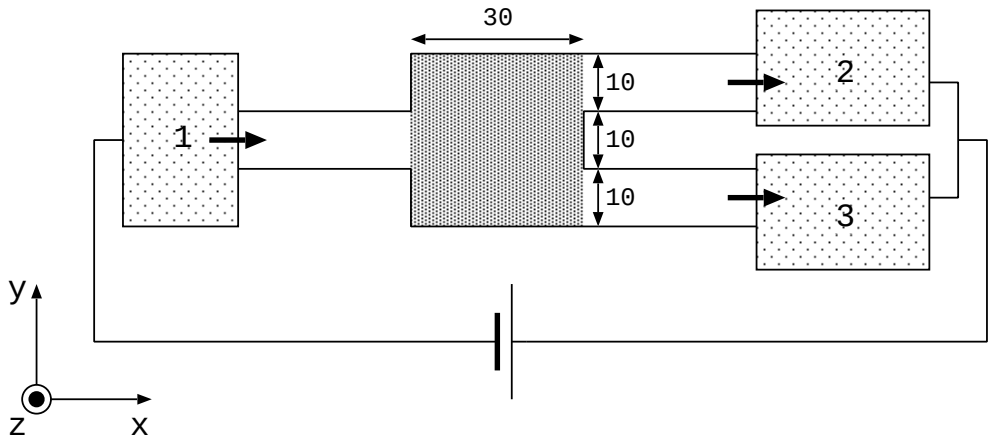

Figure 7.1: Schematic of the cavity attached to three probes. Shaded area represents the sample region with Rashba and Dresselhaus spin-orbit couplings.

The sample region contains RSO and DSO and the Hamiltonian is given by

Eq. (5.1). We have considered four different combinations of RSO and DSO as shown in Table 5.1.

7.1 Conductance and spin polarization

In this section, we show the energy dependence of the conductance and corresponding spin polarizations. The conductance and spin polarization are defined by Eqs. (6.1) and (6.2), respectively. In the following simulation, we focus on the ballistic transport ($W = 0$ in Eq. (5.1)) from the left reservoir ($J = 1$) to the upper right reservoir ($I = 2$) and the lower right reservoirs ($I = 3$).

7.1.1 Magnitude of spin polarization

Firstly, we focus on the magnitude of spin polarization (Eq. (6.3)). Figure 7.2 shows the energy dependence of the conductance and corresponding spin polarization in the presence of RSO and DSO. Similar to a T-shape conductor, high spin polarization can be obtained for the energy range of the single-channel transport in the presence of either RSO (A) or DSO (B). However, the spin polarization strongly depends on the energy in comparison with a T-shape conductor. Anisotropic properties is enhanced due to the scattering inside a cavity in the presence of RSO and DSO (C). In the case of the same strength of RSO and DSO (D), the spin polarization is smaller than above three results (A,B,C), but larger than the result obtained for a T-shape conductor. This can also attribute to the scattering inside a cavity.

7.1.2 Direction of spin polarization

Secondly, we focus on the spin polarizations in the x-, y-, and z-directions. Figure 7.3 shows the energy dependence of each components of the spin polarization at the upper and lower right probes in the presence of RSO and DSO. Obtained results are qualitatively the same as those for a T-shape conductor. Quantitatively, it shows strong energy dependence due to the cavity structure.

7.1.3 Energy levels of isolated system

In order to see the energy dependence of conductance and corresponding spin polarization in detail, we have compared these dependance with energy levels of isolated sample region. We focus on the energy dependence in the presence of RSO (Fig. 7.2 (A)) for $-3.9V_0 < E < -3.7V_0$ (Fig. 7.4). Vertical lines are corresponding to the energy levels of the 30×30 isolated sample region, which can be obtained

directly by diagonalizing the Hamiltonian (Eq. (5.1)). It is shown that the positions of large dips in conductance are well fitted with those of energy levels. Localization of electrons are enhanced at these energies althogh we have considered an open system, i.e., electrons are freely traveling from one probe to the other. Some dips and peaks of spin polarization are also observed at the energy levels of the isolated cavity. On the other hand, other dips and peaks seems independent from energy levels. If we reduce the strength of coupling between the sample region and ideal probes, such independence may disappear and transport properties can be dominated by the energy levels of the isolated cavity. In this case, however, one need to consider the electron-electron interaction inside the cavity.

7.2 Charge and spin distribution of current

In this section, we show the charge and spin distributions of a current. We focus on a ballistic transport ($W = 0$ in Eq. (5.1)). The Fermi energy is set to be $E = -3.8V_0$ where only one channel is opened. Obtained results are qualitatively the same as those of a T-shape conductor.

A: RSO

Figure 7.6 shows the charge and spin distribution of a current in the presence of RSO. The strength of RSO is set to be $\theta = 0.06\pi$. It is shown that the charge distribution is symmetric while the spin distribution is antisymmetric (A1). (A2) and (A3) show the charge and spin distribution of the current initially having the up- and down-spin components, respectively.

B: DSO

Figure 7.5 shows the charge and spin distribution of a current in the presence of DSO. The strength of DSO is set to be $\phi = 0.06\pi$. (B2) and (B3) show the charge and spin distribution of the current initially having the up- and down-spin components, respectively.

C: RSO + DSO

Figure 7.7 shows the charge and spin distribution of a current in the presence of both RSO and DSO. The strength of RSO and DSO are set to be $\theta = 0.04\pi$ and $\phi = 0.02\pi$, respectively. The charge distribution clearly shows an anisotropic transport (C1). (C2) and (C3) show the charge and spin distributions of the current initially having the up- and down-spin components, respectively.

D: RSO = DSO

Figure 7.8 shows the charge and spin distribution of a current for the same strength of RSO and DSO ($\theta = \phi = 0.03\pi$). (D2) and (D3) show the charge and spin distribution of the current initially having the up- and down-spin components, respectively.

7.3 Dynamics of wave packet

In this section, we show the dynamics of the wave packet. We have considered the isolated system which consists of the ideal probe regions and the sample region with RSO (Fig. 7.9). The size of the ideal probe and sample regions are set to be $(N_x^{\rm ideal} \times N_y^{\rm ideal}) = (50 \times 10)$ and $(N_x^{\rm sample} \times N_y^{\rm sample}) = (30 \times 30)$, respectively. The strength of RSO is set to be $\theta = 0.06\pi$. The initial condition of the wave packet is the same as that given in Sec. 5.3. One can see the more detailed dynamics of the wave packet as animation in the attached CD.

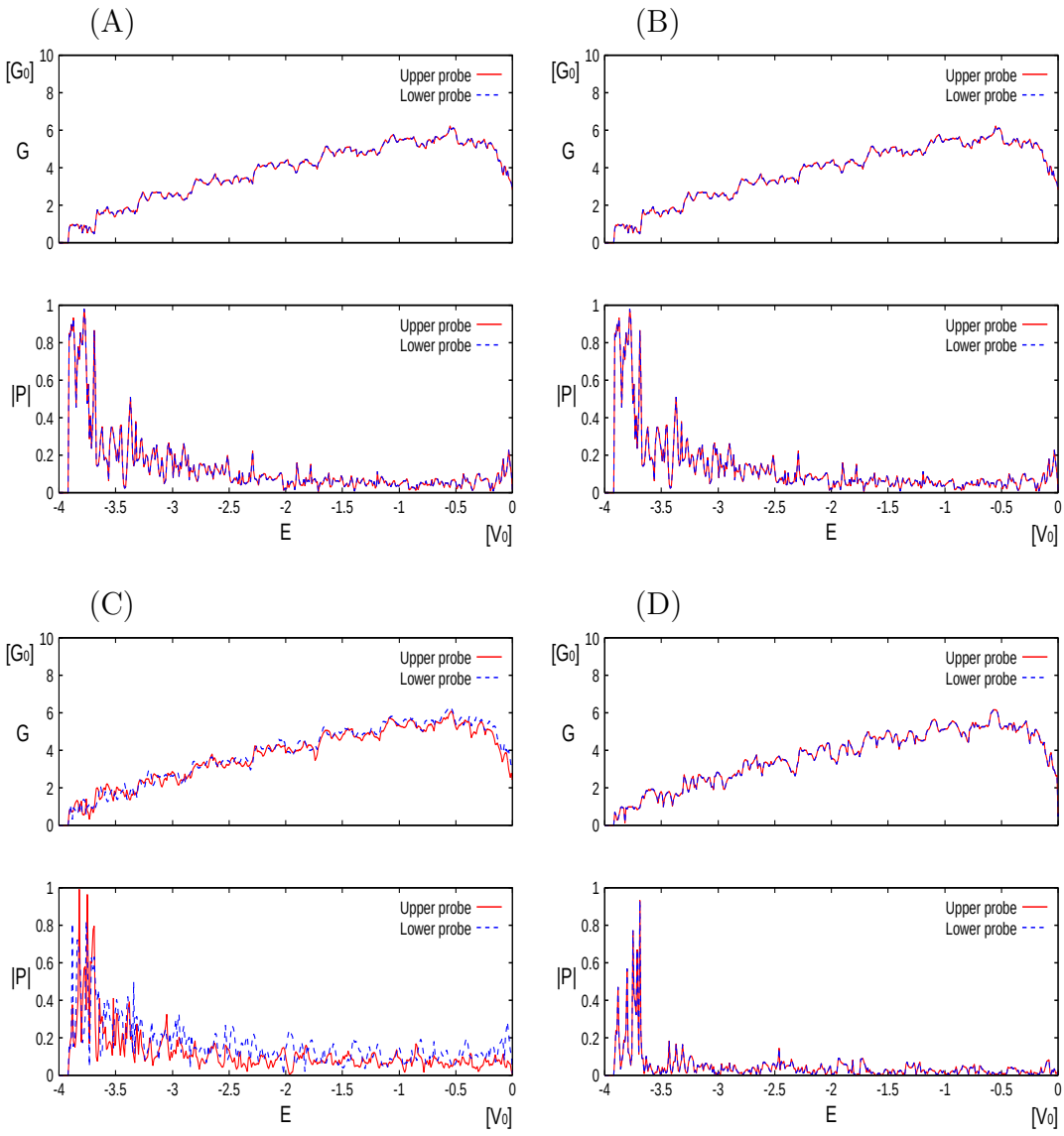

Figure 7.2: Energy dependence of the conductance (upper) and corresponding spin polarizations (lower). The strengths of RSO (θ) and DSO (ϕ) are set to be as follows. (A) $\theta = 0.06\pi$. (B) $\phi = 0.06\pi$. (C) $\theta = 0.04\pi$ and $\phi = 0.02\pi$. (D) $\theta = \phi = 0.03\pi$.

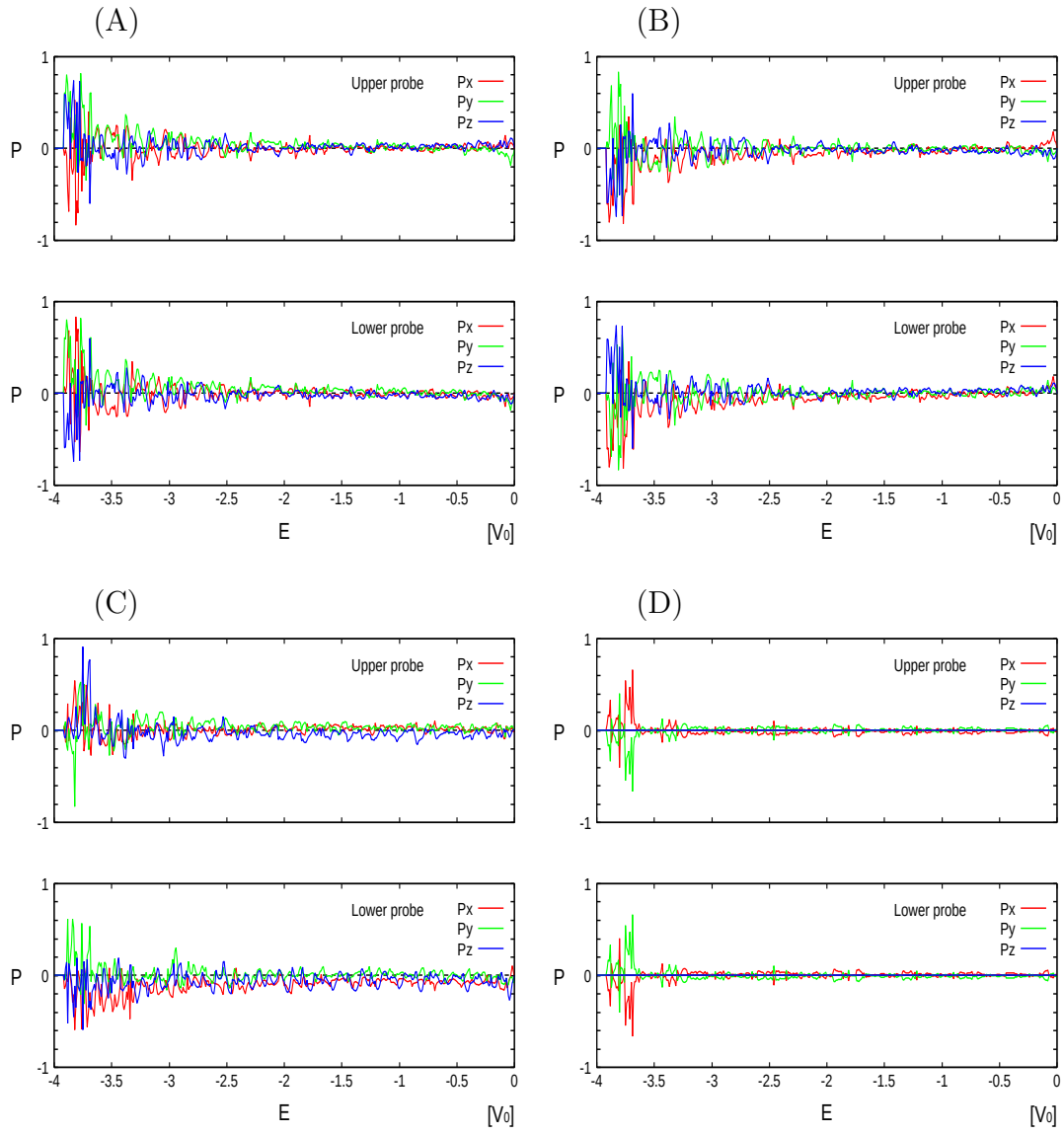

Figure 7.3: Components of spin polarization at the upper probe (upper) and the lower probe (lower). The strengths of RSO (θ) and DSO (ϕ) are set to be as follows. (A) $\theta = 0.06\pi$. (B) $\phi = 0.06\pi$. (C) $\theta = 0.04\pi$ and $\phi = 0.02\pi$. (D) $\theta = \phi = 0.03\pi$.

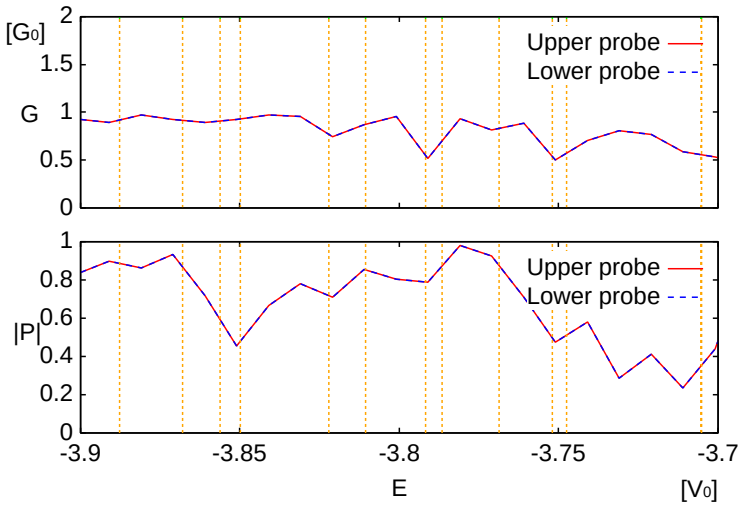

Figure 7.4: Energy dependence of conductance (upper) and corresponding spin polarization (lower) in the presence of RSO. Vertical lines are energy levels of isolated sample region.

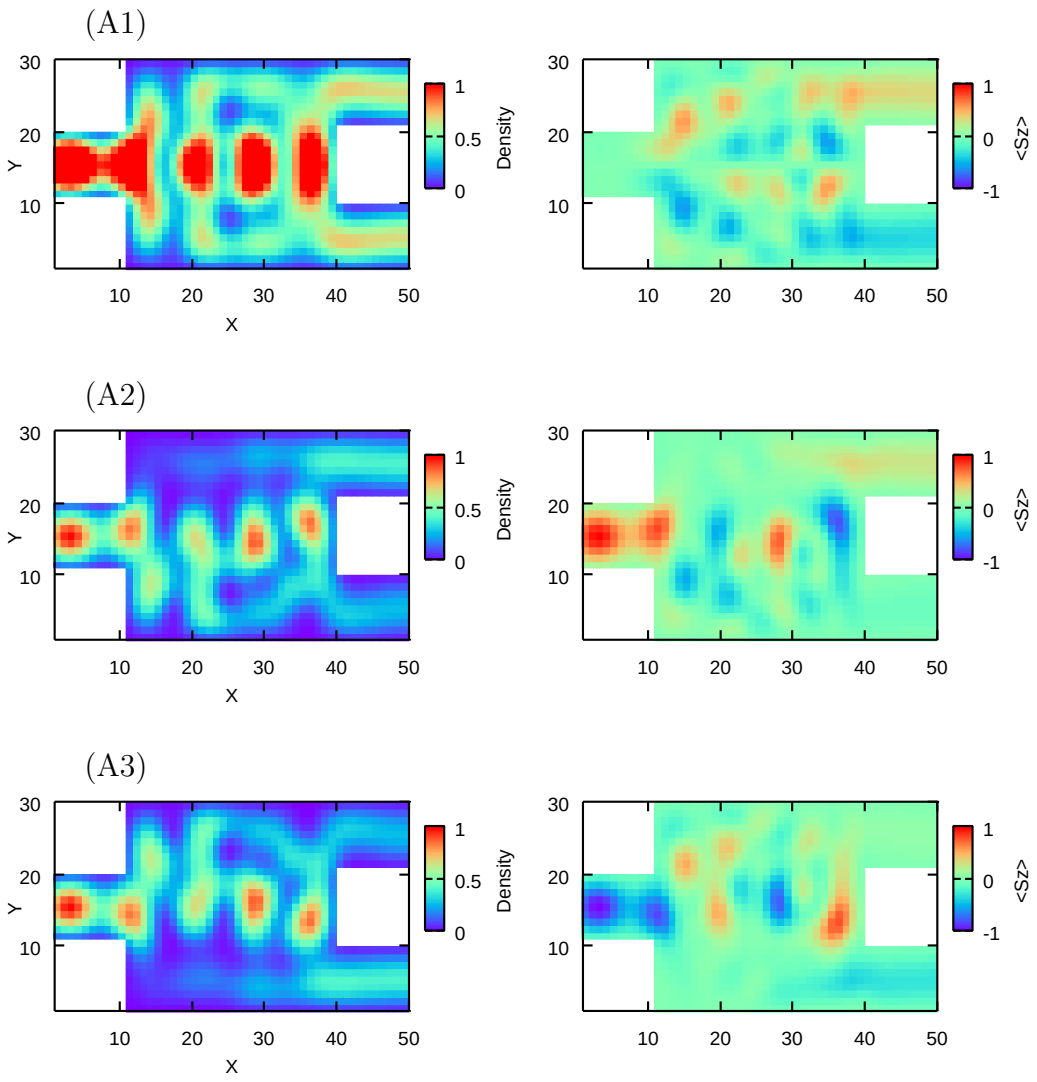

Figure 7.5: (A1) Charge and spin distribution of a current in the presence of RSO. The strength of RSO is set to be $\theta = 0.06\pi$. (A2) Up-spin component. (A3) Down-spin component.

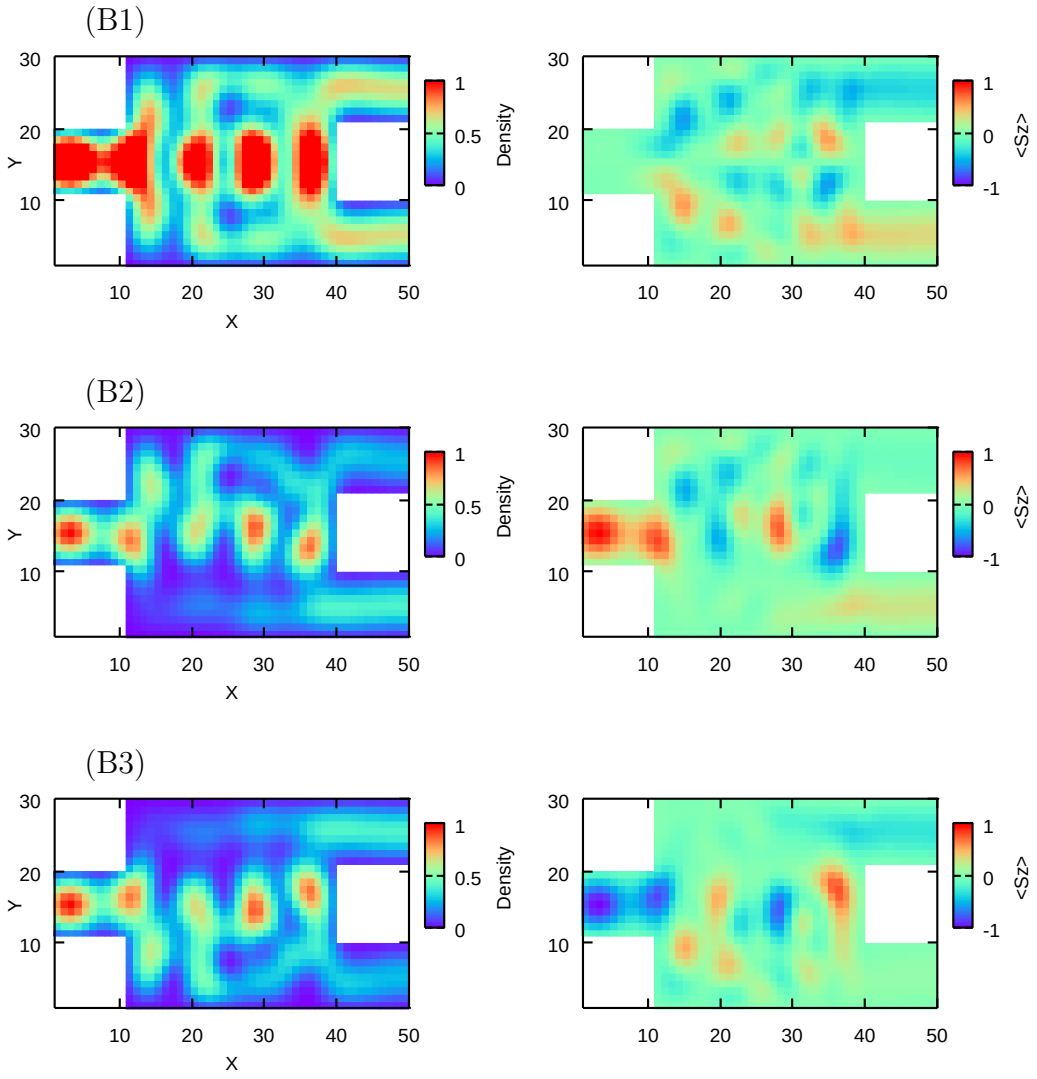

Figure 7.6: (B1) Charge and spin distribution of a current in the presence of DSO. The strength of DSO is set to be $\phi = 0.06\pi$. (B2) Up-spin component. (B3) Down-spin component.

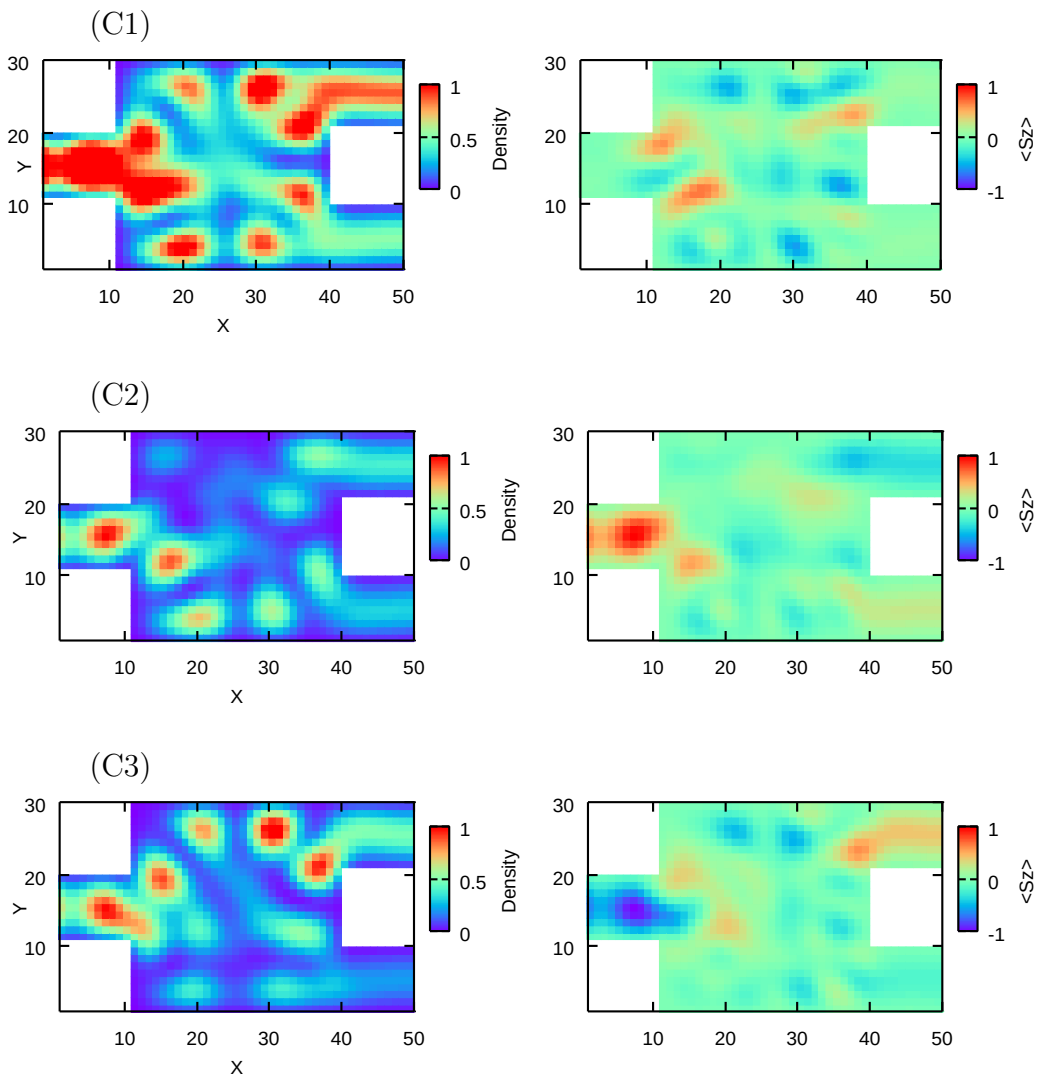

Figure 7.7: (C1) Charge and spin distribution of a current in the presence of RSO and DSO. The strengths of RSO and DSO are set to be $\theta = 0.04\pi$ and $\phi = 0.02\pi$, respectively. (C2) Up-spin component. (C3) Down-spin component.

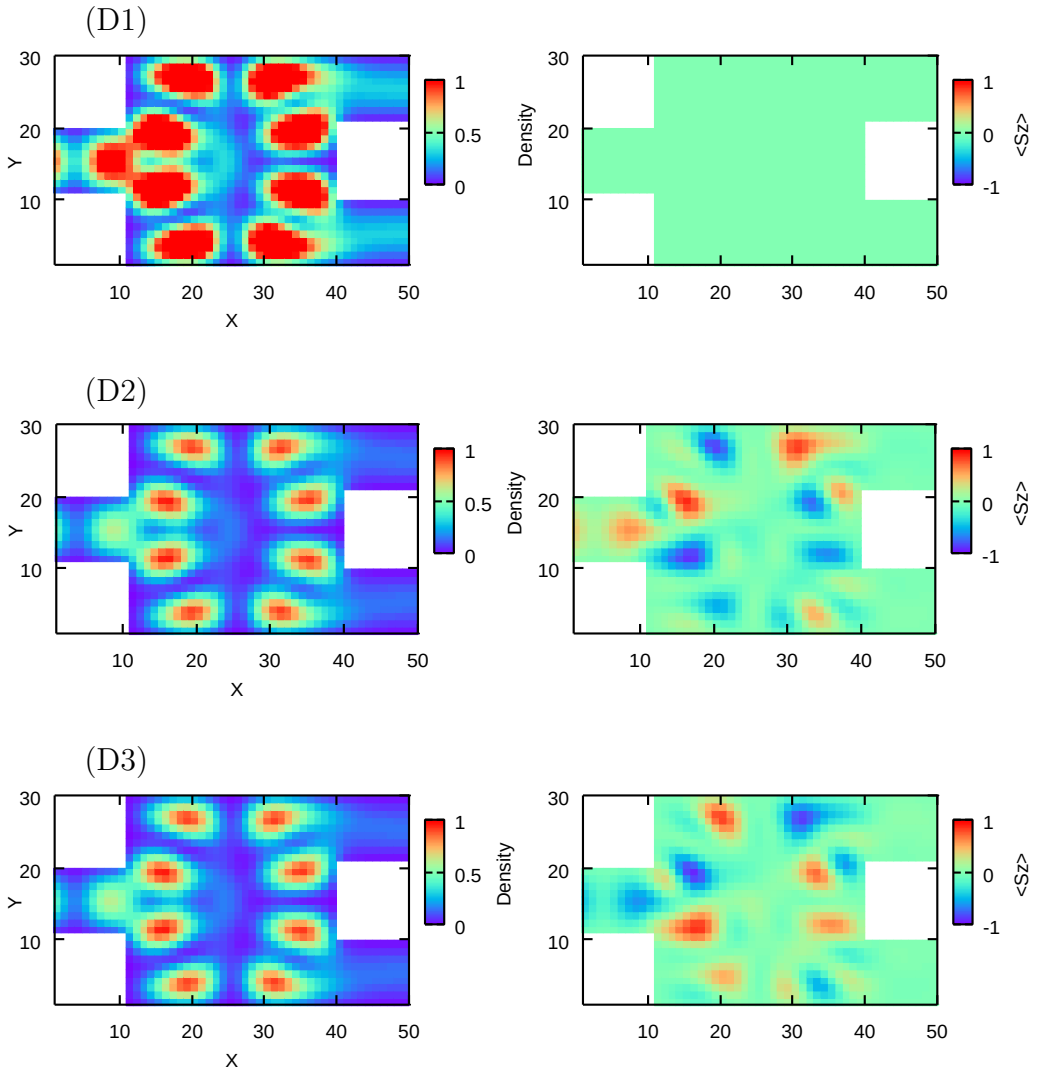

Figure 7.8: (D1) Charge and spin distribution of a current in the presence of RSO and DSO. The strengths of RSO and DSO are set to be $\theta = \phi = 0.03\pi$. (D2) Up-spin component. (D3) Down-spin component.

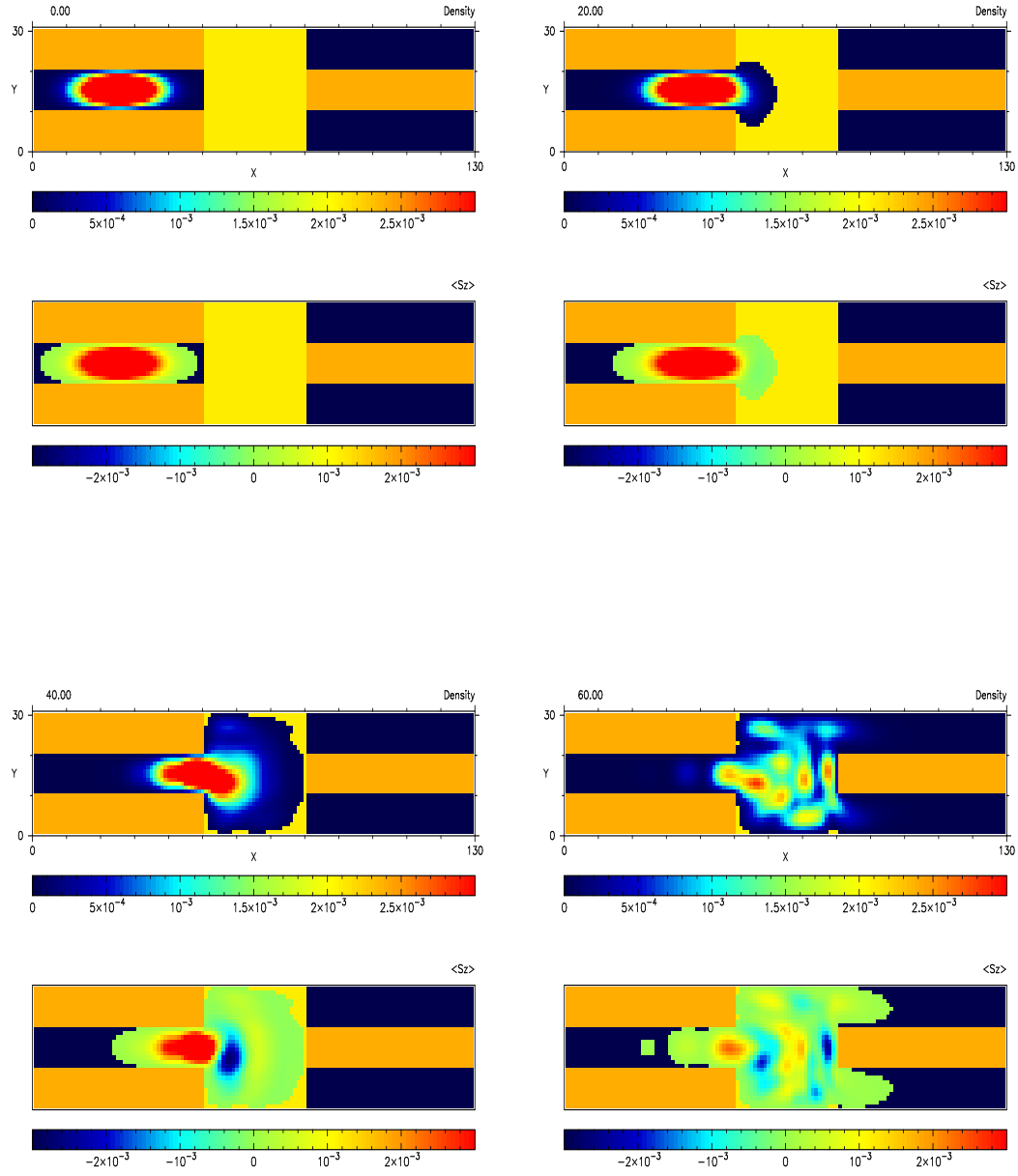

Figure 7.9: Time evolution of the wave packet. Yellow region represents the sample region with Rashba spin-orbit coupling. The time of each snapshot is $t = 0, 20, 40, \cdots$ in units of $\hbar V_0^{-1}$.

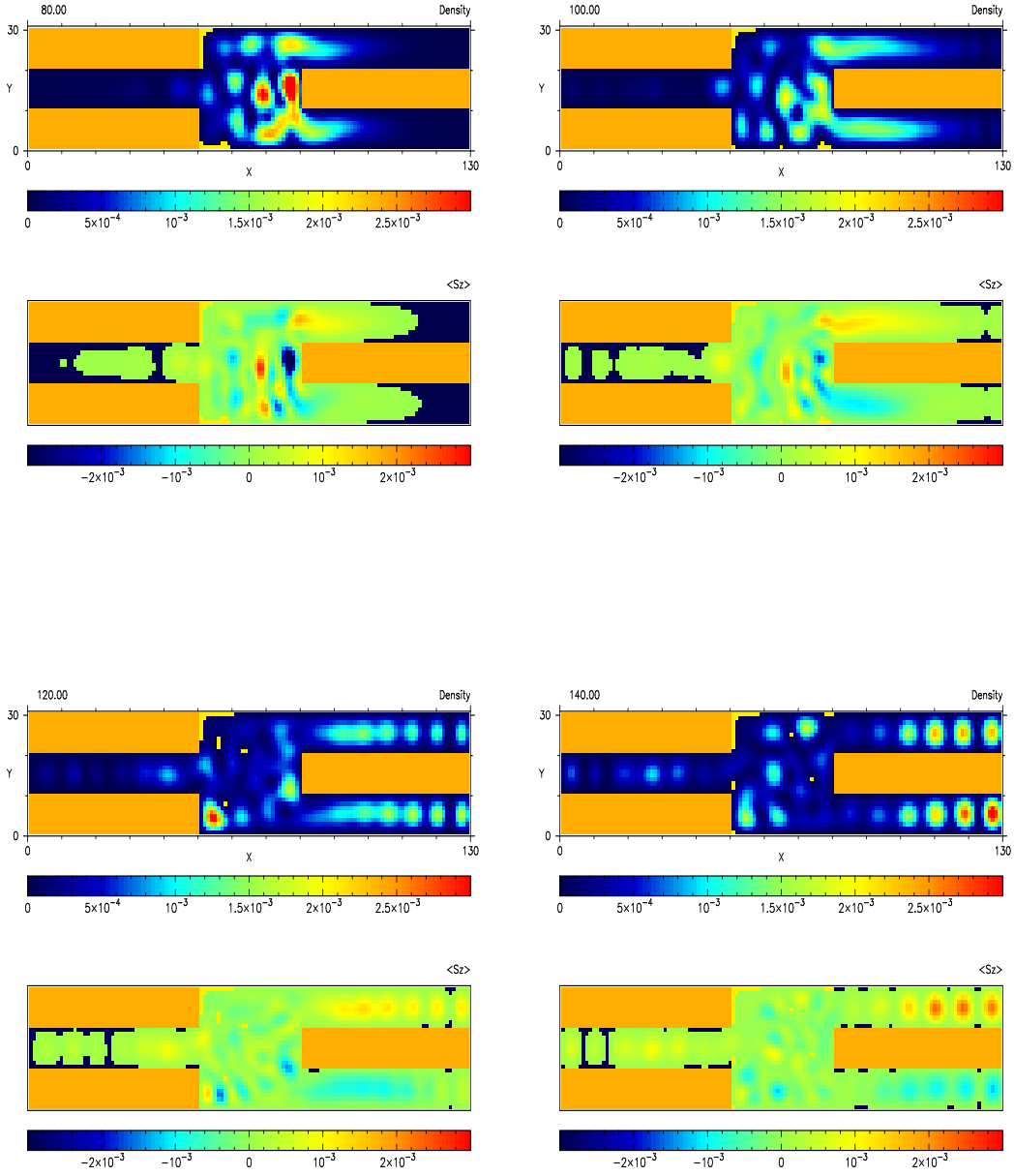
80.00
Density
30
Y
0
0
X
130
0
5x10^-4
10^-3
1.5x10^-3
2x10^-3
2.5x10^-3
<Sz>
-2x10^-3
-10^-3
0
10^-3
2x10^-3
100.00
Density
30
Y
0
0
X
130
0
5x10^-4
10^-3
1.5x10^-3
2x10^-3
2.5x10^-3
<Sz>
-2x10^-3
-10^-3
0
10^-3
2x10^-3
120.00
Density
30
Y
0
0
X
130
0
5x10^-4
10^-3
1.5x10^-3
2x10^-3
2.5x10^-3
<Sz>
-2x10^-3
-10^-3
0
10^-3
2x10^-3
140.00
Density
30
Y
0
0
X
130
0
5x10^-4
10^-3
1.5x10^-3
2x10^-3
2.5x10^-3
<Sz>
-2x10^-3
-10^-3
0
10^-3
2x10^-3

Appendix A

Calculation of Green function

A.1 Recursive calculation

In this appendix, we show how to calculate the $MN \times MN$ Green function recursively. For example, let us consider the $4M \times 4M$ Hamiltonian,

$$\begin{pmatrix} \boldsymbol{\mathcal{H}}_1 - E\boldsymbol{I} & -\boldsymbol{V} & \boldsymbol{0} & \boldsymbol{0} \\ -\boldsymbol{V}^\dagger & \boldsymbol{\mathcal{H}}_2 - E\boldsymbol{I} & -\boldsymbol{V} & \boldsymbol{0} \\ \boldsymbol{0} & -\boldsymbol{V}^\dagger & \boldsymbol{\mathcal{H}}_3 - E\boldsymbol{I} & -\boldsymbol{V} \\ \boldsymbol{0} & \boldsymbol{0} & -\boldsymbol{V}^\dagger & \boldsymbol{\mathcal{H}}_4 - E\boldsymbol{I} \end{pmatrix} \begin{pmatrix} \boldsymbol{G}_{11} & \boldsymbol{G}_{12} & \boldsymbol{G}_{13} & \boldsymbol{G}_{14} \\ \boldsymbol{G}_{21} & \boldsymbol{G}_{22} & \boldsymbol{G}_{23} & \boldsymbol{G}_{24} \\ \boldsymbol{G}_{31} & \boldsymbol{G}_{32} & \boldsymbol{G}_{33} & \boldsymbol{G}_{34} \\ \boldsymbol{G}_{41} & \boldsymbol{G}_{42} & \boldsymbol{G}_{43} & \boldsymbol{G}_{44} \end{pmatrix}$$
$$= \begin{pmatrix} \boldsymbol{I} & \boldsymbol{0} & \boldsymbol{0} & \boldsymbol{0} \\ \boldsymbol{0} & \boldsymbol{I} & \boldsymbol{0} & \boldsymbol{0} \\ \boldsymbol{0} & \boldsymbol{0} & \boldsymbol{I} & \boldsymbol{0} \\ \boldsymbol{0} & \boldsymbol{0} & \boldsymbol{0} & \boldsymbol{I} \end{pmatrix}, \tag{A.1}$$

where $\boldsymbol{\mathcal{H}}_i$ and $\boldsymbol{G}_{ij}$ denote the $M \times M$ sub-matrices of the Hamiltonian and the Green function, respectively. Here we have ignored the effect of ideal probes $\hat{\boldsymbol{\Sigma}}$ since it is not necessary to explain the mathematical procedure of the recursive method.

Firstly, we focus on the left side column of the Green function,

$$\begin{pmatrix} \boldsymbol{\mathcal{H}}_1 - E\boldsymbol{I} & -\boldsymbol{V} & \boldsymbol{0} & \boldsymbol{0} \\ -\boldsymbol{V}^\dagger & \boldsymbol{\mathcal{H}}_2 - E\boldsymbol{I} & -\boldsymbol{V} & \boldsymbol{0} \\ \boldsymbol{0} & -\boldsymbol{V}^\dagger & \boldsymbol{\mathcal{H}}_3 - E\boldsymbol{I} & -\boldsymbol{V} \\ \boldsymbol{0} & \boldsymbol{0} & -\boldsymbol{V}^\dagger & \boldsymbol{\mathcal{H}}_4 - E\boldsymbol{I} \end{pmatrix} \begin{pmatrix} \boldsymbol{G}_{11} \\ \boldsymbol{G}_{21} \\ \boldsymbol{G}_{31} \\ \boldsymbol{G}_{41} \end{pmatrix} = \begin{pmatrix} \boldsymbol{I} \\ \boldsymbol{0} \\ \boldsymbol{0} \\ \boldsymbol{0} \end{pmatrix}. \tag{A.2}$$

By calculating from the bottom row of the Hamiltonian, one can obtain the $\boldsymbol{G}_{11}$ as

$$\begin{aligned} -\boldsymbol{V}^\dagger \boldsymbol{G}_{31} + (\boldsymbol{\mathcal{H}}_4 - E\boldsymbol{I})\boldsymbol{G}_{41} &= \boldsymbol{0} \\ \boldsymbol{G}_{41} &= \boldsymbol{g}_4^{\uparrow} \boldsymbol{V}^\dagger \boldsymbol{G}_{31}\,, \end{aligned} \tag{A.3}$$

$$
\begin{aligned}
-\boldsymbol{V}^\dagger \boldsymbol{G}_{21} + (\boldsymbol{\mathcal{H}}_3 - E\boldsymbol{I})\boldsymbol{G}_{31} - \boldsymbol{V}\boldsymbol{G}_{41} &= \boldsymbol{0} \\
-\boldsymbol{V}^\dagger \boldsymbol{G}_{21} + ((\boldsymbol{\mathcal{H}}_3 - E\boldsymbol{I}) - \boldsymbol{V}\boldsymbol{g}_4^{\uparrow}\boldsymbol{V}^\dagger)\boldsymbol{G}_{31} &= \boldsymbol{0} \\
\boldsymbol{G}_{31} &= \boldsymbol{g}_3^{\uparrow}\boldsymbol{V}^\dagger \boldsymbol{G}_{21}\,, \qquad \text{(A.4)}
\end{aligned}
$$

$$
\begin{aligned}
-\boldsymbol{V}^\dagger \boldsymbol{G}_{11} + (\boldsymbol{\mathcal{H}}_2 - E\boldsymbol{I})\boldsymbol{G}_{21} - \boldsymbol{V}\boldsymbol{G}_{31} &= \boldsymbol{0} \\
-\boldsymbol{V}^\dagger \boldsymbol{G}_{11} + ((\boldsymbol{\mathcal{H}}_2 - E\boldsymbol{I}) - \boldsymbol{V}\boldsymbol{g}_3^{\uparrow}\boldsymbol{V}^\dagger)\boldsymbol{G}_{21} &= \boldsymbol{0} \\
\boldsymbol{G}_{21} &= \boldsymbol{g}_2^{\uparrow}\boldsymbol{V}^\dagger \boldsymbol{G}_{11}\,, \qquad \text{(A.5)}
\end{aligned}
$$

and

$$
\begin{aligned}
(\boldsymbol{\mathcal{H}}_1 - E\boldsymbol{I})\boldsymbol{G}_{11} - \boldsymbol{V}\boldsymbol{G}_{21} &= \boldsymbol{I} \\
((\boldsymbol{\mathcal{H}}_1 - E\boldsymbol{I}) - \boldsymbol{V}\boldsymbol{g}_2^{\uparrow}\boldsymbol{V}^\dagger)\boldsymbol{G}_{11} &= \boldsymbol{I} \\
\boldsymbol{G}_{11} &= \frac{1}{(\boldsymbol{\mathcal{H}}_1 - E\boldsymbol{I}) - \boldsymbol{V}\boldsymbol{g}_2^{\uparrow}\boldsymbol{V}^\dagger}\,. \qquad \text{(A.6)}
\end{aligned}
$$

Here $\boldsymbol{g}_i^{\uparrow}$ is defined by

$$
\boldsymbol{g}_i^{\uparrow} = \frac{1}{(\boldsymbol{\mathcal{H}}_i - E\boldsymbol{I}) - \boldsymbol{V}\boldsymbol{g}_{i+1}^{\uparrow}\boldsymbol{V}^\dagger} \qquad (\boldsymbol{g}_5^{\uparrow} = \boldsymbol{0})\,. \qquad \text{(A.7)}
$$

The $\boldsymbol{G}_{21}$ can be obtained by substituting $\boldsymbol{G}_{11}$ into Eq.(A.5). One can obtain $\boldsymbol{G}_{31}$ and $\boldsymbol{G}_{41}$ in sequence.

Secondly, we focus on the right side column of the Green function,

$$
\begin{pmatrix}
\boldsymbol{\mathcal{H}}_1 - E\boldsymbol{I} & -\boldsymbol{V} & \boldsymbol{0} & \boldsymbol{0} \\
-\boldsymbol{V}^\dagger & \boldsymbol{\mathcal{H}}_2 - E\boldsymbol{I} & -\boldsymbol{V} & \boldsymbol{0} \\
\boldsymbol{0} & -\boldsymbol{V}^\dagger & \boldsymbol{\mathcal{H}}_3 - E\boldsymbol{I} & -\boldsymbol{V} \\
\boldsymbol{0} & \boldsymbol{0} & -\boldsymbol{V}^\dagger & \boldsymbol{\mathcal{H}}_4 - E\boldsymbol{I}
\end{pmatrix}
\begin{pmatrix}
\boldsymbol{G}_{14} \\ \boldsymbol{G}_{24} \\ \boldsymbol{G}_{34} \\ \boldsymbol{G}_{44}
\end{pmatrix}
=
\begin{pmatrix}
\boldsymbol{0} \\ \boldsymbol{0} \\ \boldsymbol{0} \\ \boldsymbol{I}
\end{pmatrix}. \qquad \text{(A.8)}
$$

By calculating from the top row of the Hamiltonian, one can obtain $\boldsymbol{G}_{44}$ as

$$
\begin{aligned}
(\boldsymbol{\mathcal{H}}_1 - E\boldsymbol{I})\boldsymbol{G}_{14} - \boldsymbol{V}\boldsymbol{G}_{24} &= \boldsymbol{0} \\
\boldsymbol{G}_{14} &= \boldsymbol{g}_1^{\downarrow}\boldsymbol{V}\boldsymbol{G}_{24}\,, \qquad \text{(A.9)}
\end{aligned}
$$

$$
\begin{aligned}
-\boldsymbol{V}^\dagger \boldsymbol{G}_{14} + (\boldsymbol{\mathcal{H}}_2 - E\boldsymbol{I})\boldsymbol{G}_{24} - \boldsymbol{V}\boldsymbol{G}_{34} &= \boldsymbol{0} \\
((\boldsymbol{\mathcal{H}}_2 - E\boldsymbol{I}) - \boldsymbol{V}^\dagger \boldsymbol{g}_1^{\downarrow}\boldsymbol{V})\boldsymbol{G}_{24} - \boldsymbol{V}\boldsymbol{G}_{34} &= \boldsymbol{0} \\
\boldsymbol{G}_{24} &= \boldsymbol{g}_2^{\downarrow}\boldsymbol{V}\boldsymbol{G}_{34}\,, \qquad \text{(A.10)}
\end{aligned}
$$

$$
\begin{aligned}
-\boldsymbol{V}^\dagger \boldsymbol{G}_{24} + (\boldsymbol{\mathcal{H}}_3 - E\boldsymbol{I})\boldsymbol{G}_{34} - \boldsymbol{V}\boldsymbol{G}_{44} &= \boldsymbol{0} \\
((\boldsymbol{\mathcal{H}}_3 - E\boldsymbol{I}) - \boldsymbol{V}^\dagger \boldsymbol{g}_2^\downarrow \boldsymbol{V})\boldsymbol{G}_{34} - \boldsymbol{V}\boldsymbol{G}_{44} &= \boldsymbol{0} \\
\boldsymbol{G}_{34} &= \boldsymbol{g}_3^\downarrow \boldsymbol{V}\boldsymbol{G}_{44}\,, \qquad \text{(A.11)}
\end{aligned}
$$

and

$$
\begin{aligned}
-\boldsymbol{V}^\dagger \boldsymbol{G}_{34} + (\boldsymbol{\mathcal{H}}_4 - E\boldsymbol{I})\boldsymbol{G}_{44} &= \boldsymbol{I} \\
((\boldsymbol{\mathcal{H}}_4 - E\boldsymbol{I}) - \boldsymbol{V}^\dagger \boldsymbol{g}_3^\downarrow \boldsymbol{V})\boldsymbol{G}_{44} &= \boldsymbol{I} \\
\boldsymbol{G}_{44} &= \frac{1}{(\boldsymbol{\mathcal{H}}_4 - E\boldsymbol{I}) - \boldsymbol{V}^\dagger \boldsymbol{g}_3^\downarrow \boldsymbol{V}}\,. \qquad \text{(A.12)}
\end{aligned}
$$

Here $\boldsymbol{g}_i^\downarrow$ is defined by

$$
\boldsymbol{g}_i^\downarrow = \frac{1}{\boldsymbol{\mathcal{H}}_i - E\boldsymbol{I} - \boldsymbol{V}^\dagger \boldsymbol{g}_{i-1}^\downarrow \boldsymbol{V}} \qquad (\boldsymbol{g}_0^\downarrow = \boldsymbol{0})\,. \qquad \text{(A.13)}
$$

Lastly, we focus on the intermediate column of the Green function,

$$
\begin{pmatrix}
\boldsymbol{\mathcal{H}}_1 - E\boldsymbol{I} & -\boldsymbol{V} & \boldsymbol{0} & \boldsymbol{0} \\
-\boldsymbol{V}^\dagger & \boldsymbol{\mathcal{H}}_2 - E\boldsymbol{I} & -\boldsymbol{V} & \boldsymbol{0} \\
\boldsymbol{0} & -\boldsymbol{V}^\dagger & \boldsymbol{\mathcal{H}}_3 - E\boldsymbol{I} & -\boldsymbol{V} \\
\boldsymbol{0} & \boldsymbol{0} & -\boldsymbol{V}^\dagger & \boldsymbol{\mathcal{H}}_4 - E\boldsymbol{I}
\end{pmatrix}
\begin{pmatrix}
\boldsymbol{G}_{12} \\ \boldsymbol{G}_{22} \\ \boldsymbol{G}_{32} \\ \boldsymbol{G}_{42}
\end{pmatrix}
=
\begin{pmatrix}
\boldsymbol{0} \\ \boldsymbol{I} \\ \boldsymbol{0} \\ \boldsymbol{0}
\end{pmatrix}. \qquad \text{(A.14)}
$$

On the one hand, by calculating from the top row of the Hamiltonian, one can have

$$
\begin{aligned}
(\boldsymbol{\mathcal{H}}_1 - E\boldsymbol{I})\boldsymbol{G}_{12} - \boldsymbol{V}\boldsymbol{G}_{22} &= \boldsymbol{0} \\
\boldsymbol{G}_{12} &= \boldsymbol{g}_1^\downarrow \boldsymbol{V}\boldsymbol{G}_{22}\,. \qquad \text{(A.15)}
\end{aligned}
$$

On the other hand, by calculating from the bottom row of the Hamiltonian, one can have

$$
\begin{aligned}
-\boldsymbol{V}^\dagger \boldsymbol{G}_{32} + (\boldsymbol{\mathcal{H}}_4 - E\boldsymbol{I})\boldsymbol{G}_{42} &= \boldsymbol{0} \\
\boldsymbol{G}_{42} &= \boldsymbol{g}_4^\uparrow \boldsymbol{V}^\dagger \boldsymbol{G}_{32}\,, \qquad \text{(A.16)}
\end{aligned}
$$

and

$$
\begin{aligned}
-\boldsymbol{V}^\dagger \boldsymbol{G}_{22} + (\boldsymbol{\mathcal{H}}_3 - E\boldsymbol{I})\boldsymbol{G}_{32} - \boldsymbol{V}\boldsymbol{G}_{42} &= \boldsymbol{0} \\
-\boldsymbol{V}^\dagger \boldsymbol{G}_{22} + ((\boldsymbol{\mathcal{H}}_3 - E\boldsymbol{I}) - \boldsymbol{V}\boldsymbol{g}_4^\uparrow \boldsymbol{V}^\dagger)\boldsymbol{G}_{32} &= \boldsymbol{0} \\
\boldsymbol{G}_{32} &= \boldsymbol{g}_3^\uparrow \boldsymbol{V}^\dagger \boldsymbol{G}_{22}\,. \qquad \text{(A.17)}
\end{aligned}
$$

By substituting Eqs.(A.15) and (A.17) into the following equation, one can obtain $\boldsymbol{G}_{22}$ as

$$\begin{aligned} -\boldsymbol{V}^\dagger \boldsymbol{G}_{12} + (\boldsymbol{\mathcal{H}}_2 - E\boldsymbol{I})\boldsymbol{G}_{22} - \boldsymbol{V}\boldsymbol{G}_{32} &= \boldsymbol{I} \\ ((\boldsymbol{\mathcal{H}}_2 - E\boldsymbol{I}) - \boldsymbol{V}^\dagger \boldsymbol{g}_1^\downarrow \boldsymbol{V} - \boldsymbol{V}\boldsymbol{g}_3^\uparrow \boldsymbol{V}^\dagger)\boldsymbol{G}_{22} &= \boldsymbol{I} \\ \boldsymbol{G}_{22} &= \frac{1}{((\boldsymbol{\mathcal{H}}_2 - E\boldsymbol{I}) - \boldsymbol{V}^\dagger \boldsymbol{g}_1^\downarrow \boldsymbol{V} - \boldsymbol{V}\boldsymbol{g}_3^\uparrow \boldsymbol{V}^\dagger)} \,. \end{aligned} \tag{A.18}$$

Now we summarize the recursive calculation for the $MN \times MN$ Green function. Firstly, calculate $\boldsymbol{g}_i^\uparrow$ and $\boldsymbol{g}_i^\downarrow$ for $i = 1$ to N,

$$\boldsymbol{g}_i^\uparrow = \frac{1}{(\boldsymbol{\mathcal{H}}_i - E\boldsymbol{I}) - \boldsymbol{V}\boldsymbol{g}_{i+1}^\uparrow \boldsymbol{V}^\dagger} \qquad (\boldsymbol{g}_{N+1}^\uparrow = \boldsymbol{0}) \,, \tag{A.19}$$

$$\boldsymbol{g}_i^\downarrow = \frac{1}{(\boldsymbol{\mathcal{H}}_i - E\boldsymbol{I}) - \boldsymbol{V}^\dagger \boldsymbol{g}_{i-1}^\downarrow \boldsymbol{V}} \qquad (\boldsymbol{g}_0^\downarrow = \boldsymbol{0}) \,. \tag{A.20}$$

By using them, one can obtain the $M \times M$ diagonal sub-matrices of the Green function as

$$\boldsymbol{G}_{ii} = \frac{1}{(\boldsymbol{\mathcal{H}}_i - E\boldsymbol{I}) - \boldsymbol{V}\boldsymbol{g}_{i+1}^\uparrow \boldsymbol{V}^\dagger - \boldsymbol{V}^\dagger \boldsymbol{g}_{i-1}^\downarrow \boldsymbol{V}} \,. \tag{A.21}$$

Finally, the sub-matrices of the lower and upper triangle of the Green function can be obtained from the diagonal sub-matrices in order,

$$\boldsymbol{G}_{i+1,j} = \boldsymbol{g}_{i+1}^\uparrow \boldsymbol{V}^\dagger \boldsymbol{G}_{ij} \qquad (i \geq j) \,, \tag{A.22}$$

$$\boldsymbol{G}_{i-1,j} = \boldsymbol{g}_{i-1}^\downarrow \boldsymbol{V} \boldsymbol{G}_{ij} \qquad (i \leq j) \,. \tag{A.23}$$

A.2 Comparison with Transfer Matrix method

Let us consider the left side column of the Green function (Eq.(A.2)) again,

$$\begin{pmatrix} \boldsymbol{\mathcal{H}}_1 - E\boldsymbol{I} & -\boldsymbol{V} & \boldsymbol{0} & \boldsymbol{0} \\ -\boldsymbol{V}^\dagger & \boldsymbol{\mathcal{H}}_2 - E\boldsymbol{I} & -\boldsymbol{V} & \boldsymbol{0} \\ \boldsymbol{0} & -\boldsymbol{V}^\dagger & \boldsymbol{\mathcal{H}}_3 - E\boldsymbol{I} & -\boldsymbol{V} \\ \boldsymbol{0} & \boldsymbol{0} & -\boldsymbol{V}^\dagger & \boldsymbol{\mathcal{H}}_4 - E\boldsymbol{I} \end{pmatrix} \begin{pmatrix} \boldsymbol{G}_{11} \\ \boldsymbol{G}_{21} \\ \boldsymbol{G}_{31} \\ \boldsymbol{G}_{41} \end{pmatrix} = \begin{pmatrix} \boldsymbol{I} \\ \boldsymbol{0} \\ \boldsymbol{0} \\ \boldsymbol{0} \end{pmatrix} . \tag{A.24}$$

One can also calculate the $\boldsymbol{G}_{41}$ in the following way,

$$\begin{aligned} -\boldsymbol{V}^\dagger \boldsymbol{G}_{31} + (\boldsymbol{\mathcal{H}}_4 - E\boldsymbol{I})\boldsymbol{G}_{41} &= \boldsymbol{0} \\ \boldsymbol{G}_{31} &= \boldsymbol{V}(\boldsymbol{\mathcal{H}}_4 - E\boldsymbol{I})\boldsymbol{G}_{41} \qquad (\boldsymbol{V}^\dagger = \boldsymbol{V}^{-1}) \\ &= \boldsymbol{f}_3 \boldsymbol{G}_{41} \,, \end{aligned} \tag{A.25}$$

$$
\begin{aligned}
-\boldsymbol{V}^{\dagger}\boldsymbol{G}_{21} + (\boldsymbol{\mathcal{H}}_3 - E\boldsymbol{I})\boldsymbol{G}_{31} - \boldsymbol{V}\boldsymbol{G}_{41} &= \boldsymbol{0} \\
\boldsymbol{G}_{21} &= \boldsymbol{V}((\boldsymbol{\mathcal{H}}_3 - E\boldsymbol{I})\boldsymbol{G}_{31} - \boldsymbol{V}\boldsymbol{G}_{41}) \\
&= \boldsymbol{V}((\boldsymbol{\mathcal{H}}_3 - E\boldsymbol{I})\boldsymbol{f}_3 - \boldsymbol{V})\boldsymbol{G}_{41} \\
&= \boldsymbol{f}_2\boldsymbol{G}_{41}\,, \qquad \text{(A.26)}
\end{aligned}
$$

$$
\begin{aligned}
-\boldsymbol{V}^{\dagger}\boldsymbol{G}_{11} + (\boldsymbol{\mathcal{H}}_2 - E\boldsymbol{I})\boldsymbol{G}_{21} - \boldsymbol{V}\boldsymbol{G}_{31} &= \boldsymbol{0} \\
\boldsymbol{G}_{11} &= \boldsymbol{V}((\boldsymbol{\mathcal{H}}_2 - E\boldsymbol{I})\boldsymbol{G}_{21} - \boldsymbol{V}\boldsymbol{G}_{31}) \\
&= \boldsymbol{V}((\boldsymbol{\mathcal{H}}_2 - E\boldsymbol{I})\boldsymbol{f}_2 - \boldsymbol{V}\boldsymbol{f}_3)\boldsymbol{G}_{31} \\
&= \boldsymbol{f}_1\boldsymbol{G}_{41}\,, \qquad \text{(A.27)}
\end{aligned}
$$

and

$$
\begin{aligned}
(\boldsymbol{\mathcal{H}}_1 - E\boldsymbol{I})\boldsymbol{G}_{11} - \boldsymbol{V}\boldsymbol{G}_{21} &= \boldsymbol{I} \\
((\boldsymbol{\mathcal{H}}_1 - E\boldsymbol{I})\boldsymbol{f}_1 - \boldsymbol{V}\boldsymbol{f}_2)\boldsymbol{G}_{41} &= \boldsymbol{I} \\
\boldsymbol{G}_{41} &= \frac{1}{(\boldsymbol{\mathcal{H}}_1 - E\boldsymbol{I})\boldsymbol{f}_1 - \boldsymbol{V}\boldsymbol{f}_2}\,. \qquad \text{(A.28)}
\end{aligned}
$$

Here $\boldsymbol{f}_i$ is defined by

$$
\boldsymbol{f}_i = \boldsymbol{V}((\boldsymbol{\mathcal{H}}_{i+1} - E\boldsymbol{I})\boldsymbol{f}_{i+1} - \boldsymbol{V}\boldsymbol{f}_{i+2}) \qquad (\boldsymbol{f}_4 = \boldsymbol{I}, \boldsymbol{f}_5 = \boldsymbol{0})\,. \qquad \text{(A.29)}
$$

The procedure of this calculation is the same as that of the transfer matrix method [34]. In this approach, one need to invert the $M \times M$ sub-matrix only at the last step of the calculation in theory. In practice, however, the inversion of the sub-matrix is necessary at every five or six steps in order to avoid the divergence of the evanescent mode. Still, the operation time of the transfer matrix method is much shorter than that of the recursive Green function method.

Appendix B

Calculation of time evolution

In order to solve numerically the time-dependent Schrödinger equations, we have adopted the method based on the higher-order decomposition of exponential operators [35]. The basic formula we have used is the fourth-order decomposition

$$\exp[x(\mathcal{H}_1 + \mathcal{H}_2 + \cdots + \mathcal{H}_q)] = S(xp)S\left(x(1-2p)\right)S(xp) + O(x^5)\,, \tag{B.1}$$

where

$$S(x) \equiv e^{\frac{x}{2}\mathcal{H}_1}\, e^{\frac{x}{2}\mathcal{H}_2}\, \cdots\, e^{\frac{x}{2}\mathcal{H}_{q-1}}\, e^{x\mathcal{H}_q}\, e^{\frac{x}{2}\mathcal{H}_{q-1}}\, \cdots\, e^{\frac{x}{2}\mathcal{H}_1}\,, \tag{B.2}$$

and the parameter p is given by $p = (2 - \sqrt[3]{2})^{-1}$. Here $\mathcal{H}_1, \ldots, \mathcal{H}_q$ are arbitrary operators.

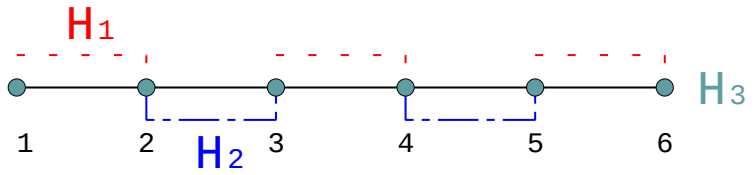

Figure B.1: Schematic of the one-dimensional wire. The Hamiltonian of this system can be decomposed into 3 parts.

In order to understand the basic idea of the method, let us consider the one-dimensional wire with 6 sites as shown in Fig.B.1. The Hamiltonian is given by

$$\mathcal{H} = \sum_{i=1}^{6} w_i c_i^\dagger c_i - \sum_{\langle ij \rangle} V_{ij} c_i^\dagger c_j\,, \tag{B.3}$$

where $c_i^\dagger(c_i)$ denotes the creation (annihilation) operator at the site i, w_i the on-site potential, V_{ij} the hopping term. The hopping is restricted in the nearest neighbors. In the matrix representation, it can be written as

$$\mathcal{H} = \begin{pmatrix} w_1 & -1 & 0 & 0 & 0 & 0 \\ -1 & w_2 & -1 & 0 & 0 & 0 \\ 0 & -1 & w_3 & -1 & 0 & 0 \\ 0 & 0 & -1 & w_4 & -1 & 0 \\ 0 & 0 & 0 & -1 & w_5 & -1 \\ 0 & 0 & 0 & 0 & -1 & w_6 \end{pmatrix}, \tag{B.4}$$

where we set $V_{ij} = 1$.

One can decompose the Hamiltonian of this system into 3 parts as

$$\mathcal{H} = \mathcal{H}_1 + \mathcal{H}_2 + \mathcal{H}_3 \,, \tag{B.5}$$

where

$$\mathcal{H}_1 = \begin{pmatrix} 0 & -1 & 0 & 0 & 0 & 0 \\ -1 & 0 & 0 & 0 & 0 & 0 \\ 0 & 0 & 0 & -1 & 0 & 0 \\ 0 & 0 & -1 & 0 & 0 & 0 \\ 0 & 0 & 0 & 0 & 0 & -1 \\ 0 & 0 & 0 & 0 & -1 & 0 \end{pmatrix}, \tag{B.6}$$

$$\mathcal{H}_2 = \begin{pmatrix} 0 & 0 & 0 & 0 & 0 & 0 \\ 0 & 0 & -1 & 0 & 0 & 0 \\ 0 & -1 & 0 & 0 & 0 & 0 \\ 0 & 0 & 0 & 0 & -1 & 0 \\ 0 & 0 & 0 & -1 & 0 & 0 \\ 0 & 0 & 0 & 0 & 0 & 0 \end{pmatrix}, \tag{B.7}$$

and

$$\mathcal{H}_3 = \begin{pmatrix} w_1 & 0 & 0 & 0 & 0 & 0 \\ 0 & w_2 & 0 & 0 & 0 & 0 \\ 0 & 0 & w_3 & 0 & 0 & 0 \\ 0 & 0 & 0 & w_4 & 0 & 0 \\ 0 & 0 & 0 & 0 & w_5 & 0 \\ 0 & 0 & 0 & 0 & 0 & w_6 \end{pmatrix}. \tag{B.8}$$

The state at the time $t + \Delta t$ is given by

$$|\psi(t + \Delta t)\rangle = \mathrm{e}^{-i\mathcal{H}\Delta t} \, |\psi(t)\rangle \,, \tag{B.9}$$

where

$$
\begin{aligned}
\mathrm{e}^{-i\mathcal{H}\Delta t} &= \mathrm{e}^{-i(\mathcal{H}_1+\mathcal{H}_2+\mathcal{H}_3)\Delta t} \\
&\simeq S(-ip\Delta t)S(-ip'\Delta t)S(-ip\Delta t) \\
&= \mathrm{e}^{-i\mathcal{H}_1\frac{p}{2}\Delta t}\,\mathrm{e}^{-i\mathcal{H}_2\frac{p}{2}\Delta t}\,\mathrm{e}^{-i\mathcal{H}_3 p\Delta t}\,\mathrm{e}^{-i\mathcal{H}_2\frac{p}{2}\Delta t}\,\mathrm{e}^{-i\mathcal{H}_1\frac{p}{2}\Delta t} \\
&\times \mathrm{e}^{-i\mathcal{H}_1\frac{p'}{2}\Delta t}\,\mathrm{e}^{-i\mathcal{H}_2\frac{p'}{2}\Delta t}\,\mathrm{e}^{-i\mathcal{H}_3 p'\Delta t}\,\mathrm{e}^{-i\mathcal{H}_2\frac{p'}{2}\Delta t}\,\mathrm{e}^{-i\mathcal{H}_1\frac{p'}{2}\Delta t} \\
&\times \mathrm{e}^{-i\mathcal{H}_1\frac{p}{2}\Delta t}\,\mathrm{e}^{-i\mathcal{H}_2\frac{p}{2}\Delta t}\,\mathrm{e}^{-i\mathcal{H}_3 p\Delta t}\,\mathrm{e}^{-i\mathcal{H}_2\frac{p}{2}\Delta t}\,\mathrm{e}^{-i\mathcal{H}_1\frac{p}{2}\Delta t}, \qquad \text{(B.10)}
\end{aligned}
$$

with $p' = 1 - 2p$.

Since $\mathcal{H}_i^2 = I\,(i = 1, 2)$, the exponentials of $\mathcal{H}_1$ and $\mathcal{H}_2$ are simply given by

$$
\begin{aligned}
\mathrm{e}^{-i\mathcal{H}_1\Delta t'} &= I + (-i\Delta t')\mathcal{H}_1 + \frac{(-i\Delta t')^2}{2!}\mathcal{H}_1^2 + \frac{(-i\Delta t')^3}{3!}\mathcal{H}_1^3 + \cdots \qquad \text{(B.11)} \\
&= I + (-i\Delta t')\mathcal{H}_1 + \frac{(-i\Delta t')^2}{2!}I + \frac{(-i\Delta t')^3}{3!}\mathcal{H}_1 + \cdots \qquad \text{(B.12)} \\
&= \cos\Delta t'\, I - i\sin\Delta t'\,\mathcal{H}_1 \qquad \text{(B.13)}
\end{aligned}
$$

$$
= \begin{pmatrix}
\cos\Delta t' & i\sin\Delta t' & 0 & 0 & 0 & 0 \\
i\sin\Delta t' & \cos\Delta t' & 0 & 0 & 0 & 0 \\
0 & 0 & \cos\Delta t' & i\sin\Delta t' & 0 & 0 \\
0 & 0 & i\sin\Delta t' & \cos\Delta t' & 0 & 0 \\
0 & 0 & 0 & 0 & \cos\Delta t' & i\sin\Delta t' \\
0 & 0 & 0 & 0 & i\sin\Delta t' & \cos\Delta t'
\end{pmatrix}, \qquad \text{(B.14)}
$$

and

$$
\mathrm{e}^{-i\mathcal{H}_2\Delta t'} = \begin{pmatrix}
0 & 0 & 0 & 0 & 0 & 0 \\
0 & \cos\Delta t' & i\sin\Delta t' & 0 & 0 & 0 \\
0 & i\sin\Delta t' & \cos\Delta t' & 0 & 0 & 0 \\
0 & 0 & 0 & \cos\Delta t' & i\sin\Delta t' & 0 \\
0 & 0 & 0 & i\sin\Delta t' & \cos\Delta t' & 0 \\
0 & 0 & 0 & 0 & 0 & 0
\end{pmatrix}, \qquad \text{(B.15)}
$$

respectively. The exponential of $\mathcal{H}_3$ is given by

$$
\mathrm{e}^{-i\mathcal{H}_3\Delta t'} = \begin{pmatrix}
\mathrm{e}^{-iw_1\Delta t'} & 0 & 0 & 0 & 0 & 0 \\
0 & \mathrm{e}^{-iw_2\Delta t'} & 0 & 0 & 0 & 0 \\
0 & 0 & \mathrm{e}^{-iw_3\Delta t'} & 0 & 0 & 0 \\
0 & 0 & 0 & \mathrm{e}^{-iw_4\Delta t'} & 0 & 0 \\
0 & 0 & 0 & 0 & \mathrm{e}^{-iw_5\Delta t'} & 0 \\
0 & 0 & 0 & 0 & 0 & \mathrm{e}^{-iw_6\Delta t'}
\end{pmatrix} \qquad \text{(B.16)}
$$

It is straightforward to apply the method to much longer wires as well as two-dimensional systems [36].

Bibliography

[1] Y.A. Bychkov and E.I. Rashba. *J. Phys. C*, 17:6039, 1984.

[2] J. Nitta, T. Akazaki, H. Takayanagi and T. Enoki. *Phys. Rev. Lett.*, 78:1335, 1997.

[3] G. Engels, J. Lange, Th. Schäpers and H. Lüth. *Phys. Rev. B*, 55:1958, 1997.

[4] S. Datta and B. Das. *Appl. Phys. Lett.*, 56:665, 1990.

[5] G. Schmidt, D. Ferrand, L.W. Molenkamp, A.T. Filip and B.J. van Wees. *Phys. Rev. B*, 62:4790, 2000.

[6] J. Nitta, F.E. Meijer and H. Takayanagi. *Appl. Phys. Lett.*, 75:695, 1999.

[7] T. Koga, J. Nitta and M. van Veenhuizen. *Phys. Rev. B*, 70:161302, 2004.

[8] S. Datta. *Quantum Transport: Atom to Transistor*. Cambridge University Press, 2005.

[9] R. Winkler. *Spin-orbit coupling effects in two-dimensional electron and hole systems*. Springer, 2003.

[10] H.P. Hjalmarson P. Vogl and J.D. Dow. *J. Phys. Chem. Solids*, 44:365, 1983.

[11] J.J. Sakurai. *Modern Quantum Mechanics*. Addison Wesley, 2nd edition, 1994.

[12] J.J. Sakurai. *Advanced Quantum Mechanics*. Addison Wesley, 1967.

[13] G. Dresselhaus. *Phys. Rev.*, 100:580, 1955.

[14] R. Lassnig. *Phys. Rev. B*, 31:8076, 1985.

[15] R. Winkler. *Phys. Rev. B*, 69:045317, 2004.

[16] V. Sih, R. C. Myers, Y. K. Kato, W. H. Lau, A. C. Gossard and D. D. Awschalom. *Nature Phys.*, 1:31, 2005.

[17] S. Bellucci and P. Onorato. *Phys. Rev. B*, 74:245314, 2006.

[18] K. Hattori and H. Okamoto. *Phys. Rev. B*, 74:155321, 2006.

[19] Y. Jiang and L. Hu. *Phys. Rev. B*, 74:075302, 2006.

[20] L. Tang Y. Xing, Q.-F. Sun and J.-P. Hu. *Phys. Rev. B*, 74:155313, 2006.

[21] S. Datta. *Electronic Transport in Mesoscopic Systems*. Cambridge University Press, 1995.

[22] J. Schliemann and D. Loss. *Phys. Rev. B*, 68:165311, 2003.

[23] M.I. D'yakonov and V.I. Perel'. *Zh. Eksp. Teor. Fiz.*, 60:1954, 1971.

[24] J.C. Egues J. Schliemann and D. Loss. *Phys. Rev. Lett.*, 90:146801, 2003.

[25] T. Ando. *Phys. Rev. B*, 44:8017, 1991.

[26] R. Landauer. *IBM J. Res. Dev.*, 1:223, 1957.

[27] C.W.J. Beenakker. *Rev. Mod. Phys.*, 69:731, 1997.

[28] A.A. Kiselev and K.W. Kim. *Appl. Phys. Lett.*, 78:775, 2001.

[29] M. Yamamoto, T. Ohtsuki and B. Kramer. *Phys. Rev. B*, 72:115321, 2005.

[30] C.W.J. Beenakker and H. van Houten. *Phys. Rev. Lett.*, 63:1857, 1989.

[31] C.-M. Hu, C. Zehnder, Ch. Heyn and D. Heitmann. *Phys. Rev. B*, 67:201302, 2003.

[32] M. Eto, T. Hayashi and Y. Kurotani. *J. Phys. Soc. Jpn.*, 74:1934, 2005.

[33] M. Yamamoto, K. Dittmer, B. Kramer, T. Ohtsuki. *Physica E*, 32:462, 2006.

[34] A. MacKinnon J. B. Pendry and P. J. Roberts. *Proc. R. Soc. London, Ser. A*, 437:67, 1992.

[35] M. Suzuki. *Phys. Lett. A*, 146:319, 1990.

[36] T. Kawarabayashi and T. Ohtsuki. *Phys. Rev. B*, 51:10897, 1995.